UNCLASSIFIED
SECURITY CLASSIFICATION OF THIS PAGE

2

REPORT DOCUMENTATION PAGE

Form Approved
OMB No. 0704-0188

1a. REPORT SECURITY CLASSIFICATION UNCLASSIFIED	1b. RESTRICTIVE MARKINGS
2a. SECURITY CLASSIFICATION AUTHORITY	3. DISTRIBUTION/AVAILABILITY OF REPORT Approved for public release; distribution is unlimited.
2b. DECLASSIFICATION/DOWNGRADING SCHEDULE	
4. PERFORMING ORGANIZATION REPORT NUMBER(S) AD-A264 647	5. MONITORING ORGANIZATION REPORT NUMBER(S) AFOSR-TR- 93 0533
6a. NAME OF PERFORMING ORGANIZATION International Business Machines Corp	6b. OFFICE SYMBOL (If applicable)
6c. ADDRESS (City, State, and ZIP Code) San Jose, CA 95120	7a. NAME OF MONITORING ORGANIZATION AFOSR/NC
	7b. ADDRESS (City, State, and ZIP Code) Building 410, Bolling AFB DC 20332-6448
8a. NAME OF FUNDING/SPONSORING ORGANIZATION AFOSR	8b. OFFICE SYMBOL (If applicable) NC
8c. ADDRESS (City, State, and ZIP Code) Building 410, Bolling AFB DC 20332-6448	9. PROCUREMENT INSTRUMENT IDENTIFICATION NUMBER F49620-89-C-0068
	10. SOURCE OF FUNDING NUMBERS

PROGRAM ELEMENT NO.	PROJECT NO.	TASK NO.	WORK UNIT ACCESSION NO.
61102F	2303	A2	

11. (U) TITLE (Include Security Classification) Fundamental Studies of Friction, Lubrication, and Wear by Atomic Force Microscopy

12. PERSONAL AUTHOR(S) Gary M. McClelland

13a. TYPE OF REPORT	13b. TIME COVERED	14. DATE OF REPORT (Year, Month, Day)	15. PAGE COUNT
/Final	FROM 7/1/89 TO 9/30/92	1993, April, 14	5

16. SUPPLEMENTARY NOTATION

93-11295

17. COSATI CODES			18. SU
FIELD	GROUP	SUB-GROUP	

identify by block number)

19. ABSTRACT To probe friction, lubrication, and wear on an atomic scale, a capacitance-based ultrahigh vacuum force microscope was developed. It measures both parallel and perpendicular forces between a tip and a surface. Friction between a diamond tip and chemical-vapor-deposited (CVD) diamond films at loads below one micronewton showed a sublinear dependence of friction on load, with the effective friction coefficient varying between 0.2 and 0.8 depending on load and location. Stick-slip behavior resulting from both surface heterogeneity and static/dynamic friction was observed. A CVD process was developed for growing single crystal diamond tips with radii as small as 30 nm. The normal force between these tips and diamond (100) and (111) surfaces agrees with calculated dispersion forces. The frictional force variation on the (100) surface are tentatively associated with a reconstructed geometry convoluted over an asymmetric tip shape, while the (111) surface exhibits features which cannot be simply associated with the surface structure. Friction is approximately 3 nanonewtons independent of loads up to 100 nanonewtons. A field emission technique was developed for continuously observing the motion of individual adsorbed atoms and molecules. The hopping of individual Cs atoms between sites on a tungsten tip was observed with 2 ps and 5 Å resolution.

20. DISTRIBUTION/AVAILABILITY OF ABSTRACT	21. ABSTRACT SECURITY CLASSIFICATION
☐ UNCLASSIFIED/UNLIMITED ☐ SAME AS RPT. ☐ DTIC USERS	UNCLASSIFIED

22a. NAME OF RESPONSIBLE INDIVIDUAL	22b. TELEPHONE (Include Area Code)	22c. OFFICE SYMBOL
Captain Thomas E. Erstfeld	(202) 767-4963	AFOSR/NC

DTIC ELECTE MAY 21 1993 S E D

OD Form 1473, JUN 86 Previous editions are obsolete. SECURITY CLASSIFICATION OF THIS PAGE

93 5 004

UNCLASSIFIED

or
&I
ed
By
Distribution /
Availability Codes
Dist | Avail and / or Special
A-1

Final Report: Fundamental Studies of Friction, Lubrication, and Wear by Atomic Force Microscopy

Gary M. McClelland
IBM Research Division
Almaden Research Center
San Jose, CA 95120

DISTRIBUTION UNLIMITED 5

Objectives

The objective of this work is to obtain an atomic-level understanding of the friction between well-characterized surfaces by using atomic force microscopy (AFM), scanning tunneling microscopy, and other surface analysis techniques.

Status of the Research Effort

(A comprehensive description of this work is given in the attached reprints and preprints.)

An Ultrahigh Vacuum Bidirectional Capacitance AFM

To measure the tribological properties of surfaces under well defined conditions, a new type of atomic force microscope was designed and constructed. This was the first vacuum force microscope, the first microscope to use capacitance detection, and the first microscope to measure forces on the tip both parallel and perpendicular to the sample surface. A comprehensive mathematical analysis of the performace of the capacitance detection system shows that the sensitivity is ultimately limited by the need to avoid snapping of the lever into the sensor electrode by the attractive electrostatic force. A very stable and sensitive capacitance-sensing electronic circuit was designed. Using curved wire cantilevers and flat plate capacitance sensors, a noise level from 0.01 to 1000 Hz of 0.03 Å RMS is achievable with the capacitance circuit, but the best performance observed was a factor of 3 higher, due to roughness of the cantilever.

Friction Between a Diamond Tip and Polycrystalline Diamond Films

The capacitance AFM was used to study the friction of a diamond tip on a polycrstalline diamond film at loads below 10^{-6} N. The tip was formed by fracturing a diamond in air. The film was grown by hot filament vapor deposition from a mixture of 1 % methane in hydrogen at a pressure of 6 kPa, resulting in crystallites $\simeq 2$ μm across. Experiments were performed without cleaning the sample and tip at a pressure below 10^{-9} Torr.

Friction was measured on a a single crystallite where topographic measurements showed a roughness of several Å over regions of several 100 Å. The dependence of friction on load was sub-linear, as expected for elastic single-asperity contact. Stick-slip behavior was observed, which in some cases could be correlated with features on the surface, but in other cases appeared to arise from a difference between static and dynamic friction. The local static and dynamic friction coefficients could be deduced from the shape of the stick-slip behavior. Depending on the point of contact, static friction coefficients could vary from 0.2 to 0.8, perhaps due to local crystal orientation.

Approved for public release;
distribution unlimited.

Fabricating Diamond Force Microscope Tips by Chemical Vapor Deposition

Previous force microscope studies have used tips of uncertain geometry and surface chemistry. We have developed a chemical vapor deposition method to manufacture single crystal diamond tips of known orientation and surface chemistry. The diamonds are grown onto the end of etch-sharpened tungsten wires on which a seed crystal is deposited onto an etched-sharpened tungsten wire by carefully controlled contact with a diamond abrasive block. Diamond crystals $\simeq 1\mu m$ in diameter are grown in a H_2/CH_4 mixture near a hot Ta wire. Of ten tips grown simultneously in a single holder, the best is chosen using scanning electron microscopy. Extremely low electron dosage is used to avoid damage to the hydrogen-terminated surface. This surface is very inert, and can be cleaned of physisorbed contaminants by flash desorption. After the friction experiment, the tip is examined by high magnification SEM to determine its orientation and apex radius (typically 30 nm).

Atomic Scale Friction of a Diamond Tip on Diamond (100) and (111) Surfaces

The vacuum AFM was modified to incorporate a dual fiber force sensor using a novel tilted configuration to avoid interference between the fiber and sample. Friction and normal forces were measured between single crystal diamond AFM tips and single crystal diamonds samples, both cleaned in UHV. This is the first AFM study involving a well-characterized tip of known orientation. The attractive normal force between the tip and surface agreed well with calculated dispersion interactions. The frictional force exhibits periodic features, which on the (100) surface are tentatively associated with a 2×1 reconstructed surface convoluted over an asymmetric tip shape. The (111) surface shows features which cannot be simply related to the surface structure. As the tip is scanned back and forth along a line, the same features are observed in each direction, but offset, suggesting the presence of a conservative force independent of the direction of motion as well as a non-conservative force. The friction is approximately $\simeq 3 \times 10^{-9}$ N, independent of loads up to 1×10^{-7} N. The differential friction coefficient for this system is less than 0.01 at the largest loads, and similarly small values have been measured for oxidized tungsten tips sliding on diamond surfaces. These values are unprecedentedly small for unlubricated sliding in vacuum, suggesting that we are close to attaining the zero friction limit predicted for incommensurate rigid sliding surfaces.

Observing the Motion of a Single Adsorbed Atom with Picosecond and Subnanometer Resolution

To characterize metal tips for AFM experiments, we became interested in applying field ion and field emission microscopy. We soon realized that field emission provides a unique opportunity to continuously observe single adsorbed atoms and molecules on the spatial and temporal scales of molecular vibration. We developed a new instrument, the femtosecond field emission camera, to record the time dependence of field emission from a sharp tip. In this instrument, the field-emitted electrons are tightly focussed into a beam, which is electrostatically swept across a detection screen as in a streak camera.

In our first experiments, hopping of single Cs atoms between sites on a W<111> tip was observed. Atomic resolution field ion microscopy was used to form sharp tips ending in a plane of three atoms. Individual Cs atoms are deposited onto a 80 K tip, and a field emission image is recorded. The tip is pulsed negatively for 2 ns while the

focussed emission beam is swept across the screen. The increased field emission excites the Cs, which hops to a nearby site. This event is recorded with 2 ps resolution by the changing field emission intensity. After the sweep, the new position of the Cs atom is reflected in the field emission image. By defocussing the e^- beam perpendicular to the sweep direction, simultaneous temporal and one dimensional spatial resolution of the dynamics is achievable. Because the accelerating field at the tip is so high, the time-of-flight spread of the field-emitted electrons, which determines our instrument's time resolution, can be shorter than 100 fs. Work underway is aimed at observing the vibrational motion of individual adsorbed molecules.

Publications

"Tribology at the Atomic Scale," G. M. McClelland and S. R. Cohen, in *Chemistry and Physics of Solid Surfaces VIII*, eds. R. Vanselow and R. Rowe (Springer, Berlin, 1990), p. 419.

"Force Microscopy with a Bidirectional Capacitance Sensor," G. Neubauer, S. R. Cohen, G. M. McClelland, D. Horne, and C. M. Mate, *Rev. Sci. Instrum.* **61** 2296 (1990).

"Nanotribology of Diamond Films Studied by Atomic Force Microscopy," G. Neubauer, S. R. Cohen, G. M. McClelland, and H. Seki, in *Thin Films: Stresses and Mechanical Properties II* eds. M. F. Doerner, W. C. Oliver, G. Pharr and F. R. Brotzen. *MRS Symposium Proceedings* **188**, 219-224 (1990).

"Friction at the Atomic Scale," G. M. McClelland and J. N. Glosli, in *Fundamentals of Friction: Macroscopic and Microscopic Processes* , eds. I. L. Singer and H. M. Pollock, (Kluwer, Dordrecht, 1992), p. 405.

"Diamond Force Microscope Tips Fabricated by Chemical Vapor Deposition," G. J. Germann, G. M. McClelland, Y. Mitsuda, M. Buck, and H. Seki, *Rev. Sci. Instrum.* **63**, 4053 (1992).

"Atomic Scale Friction of a Diamond Tip on Diamond (100) and (111) Surfaces," G. J. Germann, S. R. Cohen, G. Neubauer, G. M. McClelland, H. Seki, and D. Coulman, J. Appl. Phys. **73**, 163 (1993).

"Observing the Motion of a Single Surface Atom with Picosecond and Sub-Nanometer Resolution," H. Heinzelmann, F. Watanabe, and G. M. McClelland, Phys. Rev. Lett., in press.

Technical Personnel

Principal investigator: Gary M. McClelland.

Technician: Bruce A. Hoenig.

Visiting Scientists (postdocs): Gabi Neubauer, Yoshitaka Mitsuda, Harry Heinzelmann, Geoffrey Germann.

Papers Presented

"Tribology at the Atomic Scale," Eighth International Summer Institute on Surface Science, Milwaukee, August 22, 1989.

"Nanotribology Using a 2D AFM with Capacitative Detection," AVS Meeting, Boston, October 26, 1989.

"Tribology at the Atomic Scale," AFOSR Chemical Dynamics Contractors Meeting, Captiva Island, Florida, November 1, 1989.

"Friction at the Atomic Scale," U. of Akron Physics Seminar, November 29, 1989.

"Atomic Scale Tribology of Graphite and Diamond," AFOSR Tribology Contractors Meeting, Dayton, Ohio, December 1, 1989.

"Tribology at the Atomic Scale," Sandia National Labs, February 9, 1990.

"Nanotribology of Diamond Films Studied by Atomic Force Microscopy," MRS Meeting, San Francisco, April, 1990.

"The Atomic Dynamics of Friction," Gordon Conference on Energetic Materials, June 1990.

"The Atomic Dynamics of Friction," International Symposium on Industrial Tribology, Chicago, August, 1990.

"Friction at the Atomic Scale," West Coast Spectroscopy Conference, Asilomar, February, 1991.

"Tribology at the Atomic Scale," March APS meeting, Cincinnati, 1991.

"Friction at the Atomic Scale," McIlvain Lecture at University of Wisconsin Chemistry Department, April 24, 1991.

"Friction at the Atomic Scale," NATO ASI on Fundamentals of Friction, Braunlage, Germany, July, 1991.

"Bidirectional AFM Study of Diamond-Diamond Friction in UHV," International STM Conference, Interlaken, August, 1991.

"Bidirectional AFM Study of Diamond-Diamond Friction in UHV," AFOSR contractors meeting, Irvine, October 22, 1991.

"Friction and Picosecond Dynamics at the Atomic Scale," 12th International Vac. Cong./8th Intl. Conf. on Solid Surfaces, The Hague, Netherlands, October 12-16, 1992.

"Bidirectional Force Microscope Study of Diamond-Diamond Friction in UHV," ACS meeting, San Franciso, April 5-9, 1992.

"Bidirectional Force Microscope Study of Diamond-Diamond Friction in UHV," International Conference on Metalurgical Coatings and Thin Films, April 5-9, 1992.

"Direct Observation of Picosecond Dynamics of Individual Surface Atoms," International Field Emission Symposium, Halifax, August 11-15, 1992.

Patent

"Subpicosecond Atomic and Molecular Motion Detection and Signal Transmission by Field Emission," G. M. McClelland, U. S. patent 5151594, issued Sept. 29, 1992.

18. Tribology at the Atomic Scale

*Gary M. McClelland and Sidney R. Cohen**

IBM Research Division, Almaden Research Center
San Jose, CA 95120-6099, USA

Tribology is the study of contacting surfaces rubbing against each other. It encompasses the topics of friction, lubrication, and wear, and historically has received the most attention from mechanical engineers. The study of tribology has generally been motivated by the need to optimize the efficiency, endurance, and precision of mechanical devices. There has been a gradually increasing appreciation that tribology presents interesting fundamental problems to materials scientists, physicists, chemists and particularly surface scientists, and that solving these fundamental problems could have striking ramifications for applied problems.

This paper reviews recent experimental and theoretical developments involving tribology at the atomic scale. After a brief summary of key concepts in classical tribology, experimental results will be reviewed from instruments whose resolution approaches the atomic scale, including the field ion microscope, the atomic force microscope, and the surface force apparatus. Finally, theoretical models are discussed in which the motion of individual atoms are followed. This chapter includes little discussion of the extensive previous work which has shown *indirectly* the role of atomic scale phenomena, such as the effect of monolayers on friction and adhesion.

For a compilation of many research articles dealing with atomic scale and near atomic scale tribology, the reader is referred to a recent proceedings volume [18.1]. An excellent monograph concerning surface forces (but not frictional forces) has appeared [18.2], and two recent monographs highlight the role of surface physics in tribology [18.3, 4]. A collection of articles outlines new directions in tribology [18.5].

18.1 Concepts in Classical Tribology

Since many readers of this chapter may be unfamiliar with classical tribology, a summary of key concepts follows; many books on the subject are available [18.6]. The major goal of tribology is to reduce wear of rubbing mechanical parts, but wear may also be the desired outcome during machining and polishing. For a given system, wear may occur through one or more of several mechanisms, including abrasion, adhesion, chemical processes, and fatigue. Even for a given

* Chaim Weizmann Postdoctoral Fellow

load and contact area, wear rates can vary tremendously, over 10 orders of magnitude. Another goal in most tribological applications is to reduce friction, although in devices such as brakes, high friction is desirable. In contrast to wear rates, for different materials, friction coefficients are found to vary over a range of 0.01 to 3, with the vast majority of systems falling between 0.1 and 1.

Because of the complexity of sliding interfaces, there are few universal laws in tribology. One important empirical relationship, Amontons' Law, holds that for a given sliding system, the ratio of the frictional force to load is, to a good approximation, constant over several orders of magnitude variation in load. This ratio, the friction coefficient, is independent of the apparent contact area and depends only weakly on the surface roughness. Qualitatively, Amontons' Law arises from the fact that for real surfaces the true contact area is generally much less than 1% of the apparent contact area. Most surfaces can be described as a collection of mildly sloped asperities (bumps) with various heights and curvatures arranged across the surface (Fig. 18.1a,b). When the load increases from zero, at first, only the tips of a very few asperities come into contact. As the load increases further, the true contact area increases because existing contacts broaden and more asperities come into contact. Qualitatively, it is this increasing contact area which leads to the increase in friction with load described by Amontons' Law.

For the particular case of plastic asperity contact, Amontons' Law arises in a straightforward fashion. The frictional force is the product of the material shear strength and the contact area, which is in turn proportional to the load divided by the yield strength. Comparing different materials, the shear and yield strengths tend to vary together, leading to the relatively small range of friction coefficients observed. For many systems, individual asperities interact not by plastic, but rather by elastic contact, for which the contact area is proportional to the 2/3 power of the load [18.7]. However, it has been shown that for almost any type of asperity contact, the total contact area summed over all asperities is

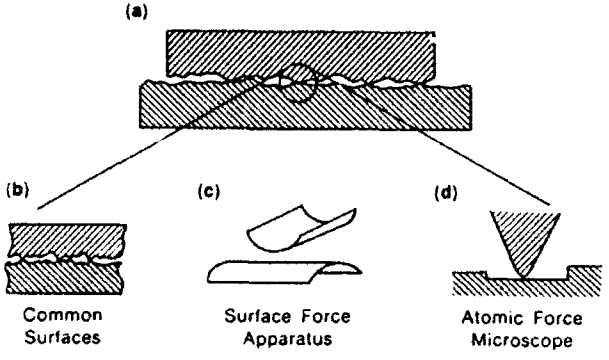

Fig. 18.1. Two macroscopic rubbing surfaces in contact (*a*), and in enlargement (*b,c,d*). For common surfaces, the contact is heterogeneous even on an atomic scale (*b*). In model experiments, contact may be simplified by using a surface force apparatus (*c*) or by using a single asperity technique, such as the atomic force microscope (*d*)

proportional to the load, if a distribution in heights of the asperities is taken into account [18.8].

Lubricants decrease friction and wear by separating sliding surfaces by a layer of low shear strength. Hydrodynamic lubrication occurs when the two moving surfaces are separated by a liquid film. The Reynolds Equation predicts that a liquid film is maintained quite naturally in very simple systems, such as that of a cylinder rotating with respect to another concentric cylinder which contains a liquid lubricant. As long as rotation is maintained, the load will not squeeze out the film. Hydrodynamic lubrication is an ideal subject for engineering analysis, because the performance of bearings can be predicted very accurately by a numerical analysis of fluid flow. Under some conditions, the viscosity of very thin films can be increased by the high pressure at the contact, resulting in elastohydrodynamic lubrication.

In boundary lubrication, the friction and wear of two surfaces is reduced by an adsorbed film as thin as a monolayer on one or both surfaces. If the layer does not bind strongly to the opposing surface, the interfacial shear strength is small, resulting in low friction and wear. Through this scheme, low friction can be achieved by using a hard bearing material for low contact area together with a soft overlayer of low shear strength.

Stick-slip friction is a commonly observed phenomenon, in which an increasing lateral force on an object produces no motion (stick) until the object suddenly leaps forward (slip) before coming to rest again. This behavior can occur when the force required to initiate sliding from zero velocity (the static friction) is greater than the force required to maintain sliding at a non-zero velocity (the kinetic friction). The static friction can be higher because slow processes such as chemical reactions have more time to occur at a static interface than at a moving one.

18.2 Experimental Approaches

18.2.1 Surface Force Apparatus

The intricate role in tribology of multiasperity contact, outlined above, highlights the importance of making measurements under conditions where asperities are well-defined or absent, even at the atomic level. An atomically flat surface is an ideal sample, but generally such surfaces can be prepared only in vacuum and with a size only up to tens of nanometers. A virtually unique exception is mica, which can be cleaved step-free over areas of several square centimeters (Fig. 18.2). It is the sample employed in the surface force apparatus (SFA) [18.9, 10] which has been successfully used to measure the forces between microscopic surfaces at distances ranging from several angstroms to hundreds of nanometers. In this instrument, cleaved mica sheets are are fashioned into a cylindrical shape and oriented with the axes perpendicular to create a "contact" zone of several tens of square microns. A delicate spring attached to one of the cylinders allows detection of forces as low as 10^{-8} N, while the distance between

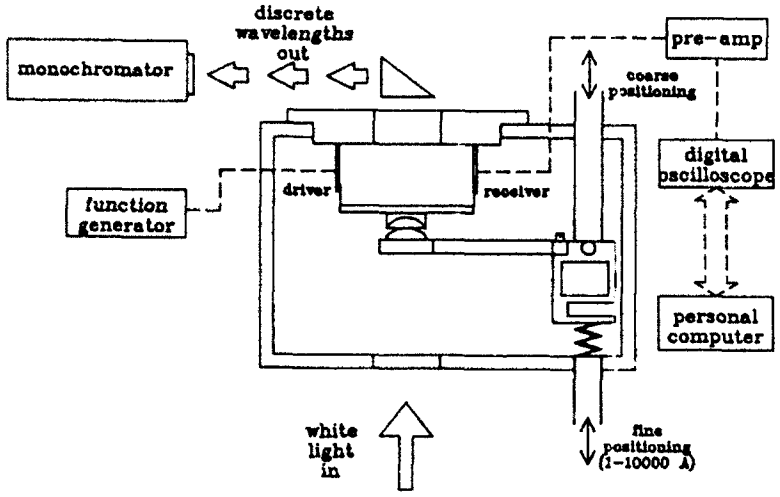

Fig. 18.2. Schematic representation of the surface force apparatus. From [18.33]

the interfaces is monitored using an optical technique; by silvering the back of the mica and shining a white light into the interface, multiple beam interferometry and fringes of equal chromatic order are used to observe separations to an accuracy of 1 Å.

If the surfaces of the SFA are immersed in a liquid and their separation decreased to near molecular dimensions, the liquid layer separating them will, at some point, cease to exhibit bulk properties. In particular the density in a liquid oscillates at short radial distances from a molecule or surface, as may also be deduced from X-ray studies [18.11, 12, 13]. A number of theoretical studies of liquids near surfaces have been able to model the oscillatory behavior [18.14, 15, 16], the envelope of which decays with distance from the surface [18.17, 18]. This change in liquid density gives rise to oscillatory solvation or structural forces, which have been observed experimentally using the SFA [18.2, 19, 20]. The effect is due to the disruption of ordered molecular layers upon the approach of a second surface. The oscillations, which vary alternately between attraction and repulsion, have a periodicity of the mean molecular diameter.

a) Dependence of Adhesive Energy on Lattice Orientation. Besides its use in monitoring forces for non-contacting surfaces during approach or retraction, the SFA can measure the adhesive force required to separate two surfaces. When two identically oriented crystals of the same material are brought into contact, a single perfect crystal can be formed, and the adhesion energy is twice the surface energy of a single crystal. However, if the crystals are misoriented, a

grain boundary, such as exists in a polycrystalline sample, is produced when the surfaces are brought together. Perfect bonding is not achieved, and the adhesion is reduced.

McGuiggan and *Israelachvili* have recently determined how the adhesion force between two mica cylinders in water depends on their angular misorientation [18.21, 22]. Narrow angular minima in the adhesive force are found by SFA measurements (Fig. 18.3). The adhesion enhancement at perfect alignment is large ($\simeq$ 50%), with a full width at half maximum of only about 0.5°. The very narrow peak widths observed in the mica adhesion experiments arise from the relative strength of the *intersolid* bonds formed across the interface with respect to the *intrasolid* bonds near the surface within each solid. The weak intersolid bonds between the mica cylinders are able to laterally distort the lattices only slightly, so that only a slight angular mismatch can be accomodated.

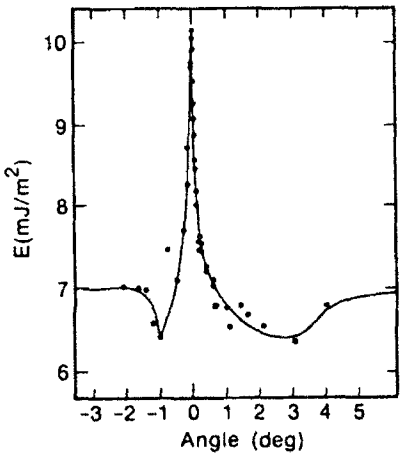

Fig. 18.3. Adhesion energy versus misorientation angle θ for two mica surfaces in water. From [18.21]

b) Thin Fluid Flow. In a lubricated system, an abrupt increase in friction and wear is expected when the lubricant layer decreases to a thickness of a few molecules. It is essential to understand to what extent continuum fluid dynamics based on the bulk viscosity can be extended into this regime. *Chan* and *Horn* [18.23] and *Israelachvili* [18.24] have explored this problem with the SFA, which in one experiment can probe fluid dynamics from the continuum micrometer level down to the single monolayer level. Figure 18.4 presents a "drainage" experiment with OMCTS (octamethylcyclotetrasiloxane, $[CH_3)_2\ SiO]_4$), described by *Chan* and *Horn* [18.23]. In this experiment a well-defined force pushes the mica plates of the SFA together, expelling the liquid between them. As the plates move closer, the approach rate decreases as the drainage path becomes more constrained; in the figure, this effect is manifested in the plot of cylinder separation vs. time. Since the experimental geometry is very well defined, the approach rate

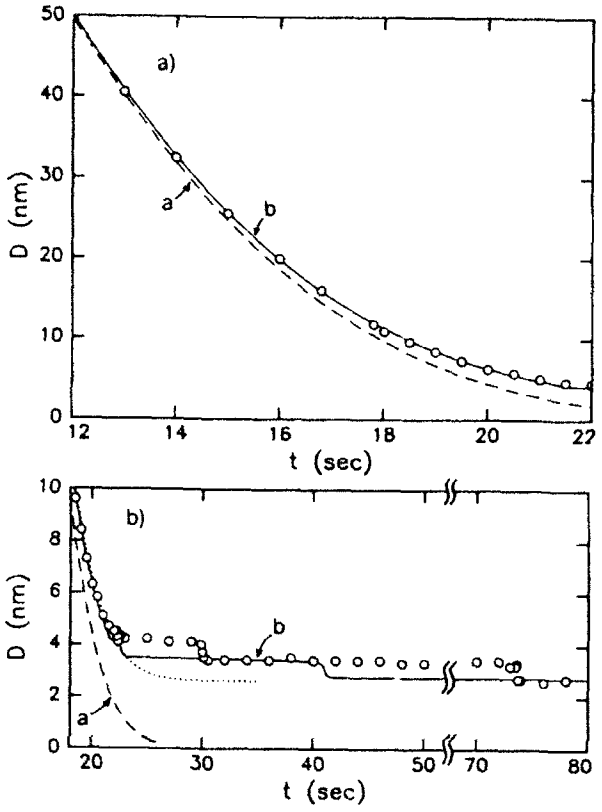

Fig. 18.4a,b. Drainage of OMCTS from between two crossed mica cylinders pushed together by a force. Distance D between the cylinders versus time. See text. From [18.23]

expected for a structureless liquid continuum with the viscosity of bulk OMCTS can be calculated, and is displayed in Fig. 18.4 with the experimental results. The continuum model, labelled "a" in Fig. 18.4 agrees quite well with the data until the liquid thickness decreases to below about 20 nm, at which point the experimental drainage rate is slower than predicted by the model.

The authors suggest that the deviation of their results from the continuum theory is due to a layer of liquid adjacent to each surface being immobilized by its interaction with the surface. They find that, down to a surface separation of about 4 nm, the experiment can be fit (curve "b") by assuming that the thickness of each immobile layer is about 1.3 nm, just less than twice the molecular diameter of OMCTS. The authors emphasize that, while this is a physically appealing interpretation, it is obviously an oversimplified picture.

At separations below about 4 nm, the discreteness of the flowing layers themselves becomes manifest in the abrupt changes of plate separation in steps of one molecular diameter. The change occurs at later times than can be accounted for from the measured static force alone, indicating that the effect is a dynamic one. Chan and Horn speculate that the retarded drainage of the discrete layers may be due to the effect of layering on molecular mobility or to the inability of the constricted molecules to move around each other.

Georges and his co-workers [18.25] have studied the dynamic and static forces between curved macroscopic surfaces other than mica. They forego the absolute distance calibration afforded by interferometry, instead using capacitance measurements to monitor the relative displacement of the surfaces. In a study of the flow of dodecane between two alumina cylinders with roughness of 2 nm, they found deviations from bulk behavior at separations less than 5 nm, where the observed irreversibility in the normal force was attributed to molecular packing [18.25]. They have also investigated a lubricant solution containing colloidal calcium carbonate particles and the effect of the adsorption of these particles on the mechanical interactions of surfaces < 100 nm apart [18.26].

Matthewson and *Mamin* have recently emphasized that the role of liquid films in determining meniscus and viscous forces involved in adhesion and friction depends qualitatively on the thickness of the films and on surface flatness [18.27].

c) Shear Motion. The use of curved mica plates to study surfaces in shear motion has a long history, starting in 1955 with a study by *Bailey* and *Courtney-Pratt* [18.28], who demonstrated that coating the mica surfaces with a monolayer of calcium stearate reduces the friction by a factor of forty. Later, *Briscoe* and *Evans* studied the tribological behavior of dry Langmuir-Blodgett films [18.29].

Several recent studies have employed the SFA to probe the shear behavior of thin liquid films constrained between mica plates. Because of the oscillating force behavior described above, even a multilayer of liquid can support a load. For the shear studies, the mica plates are attached to their supports by a flexible adhesive, which allows the plates to deform locally at the contact so as to become parallel. *Israelachvili* et al. described a study in which mica surfaces separated by cyclohexane and OMCTS were sheared hundreds of μm over each other while monitoring the shear force, load, and separation between the plates [18.30]. The observed response can be characterized by a critical shear stress; at shear stresses below this critical value, no sliding occurs, while at this shear stress, sliding commences. The frictional force during sliding is roughly independent of velocity. The novel feature of this experiment is the observation of "quantized friction". The measured shear stress varies over a set of discrete values, which are directly related to the number of liquid layers trapped between the plates. For cyclohexane, the shear stress is 2×10^7 N/m^2 for one layer, and decreases by about a factor of two for each additional layer up to four layers. The friction measured for OMCTS multilayers is considerably less, an effect which the authors attribute to the fact that the more gradually curved OMCTS molecules feel smoother than cyclohexane to the mica surfaces.

Israelachvili et al. have also reported stick-slip behavior for these systems [18.31], indicating that the static friction is greater than the kinetic friction under conditions where plastic deformation or chemical reactions with the surface are unlikely. The fact that the friction for static plates is greater than that for moving plates suggests a liquid ordering process occurs when the plates are not sliding. Water is found to act as a good lubricant under conditions when the K^+ ions are not removed from the mica surface, so that they exert a repulsion between the plates [18.32].

Van Alsten and *Granick* have reported a series of experiments [18.33, 34, 35] using an apparatus similar to that of Israelachvili et al. A major difference was that the amplitude of the oscillating shear applied was only on the order of hundreds of angstroms. For hexadecane, OMCTS, and other liquids, these workers found that at moderate pressures, there is no critical shear stress, but rather a viscous response is observed. In other words, shear motion occurs even in response to a very small shear force, and the shear rate is proportional to the force. The authors deduce an effective viscosity from their measured data, but caution that this number cannot be regarded as a true viscosity, because of the very thin anisotropic geometry involved. The fact that the effective viscosities measured are up to four orders of magnitude larger than those of the corresponding bulk liquids is probably attributable to the constrained quasi-two-dimensional geometry available for fluid flow between the mica plates. An increasing effective viscosity was found with decreasing film thickness. Also, the pressure could be varied over a factor of two without decreasing the film thickness, while the effective viscosity increased by about a factor of four. From such observations an effective activation volume of $3\,nm^3$ can be calculated. This is much larger than the volume of a single molecule, suggesting that the fundamental process for flow involves many molecules.

As the pressure is increased, Van Alsten and Granick find a sudden apparent "freezing" of the liquid film. At this point the viscous response disappears, and the sample appears to take on a critical shear stress. Sliding only occurs when this shear stress is exceeded. After the pressure is increased, the critical shear stress increases slowly with time, requiring about 15 minutes to attain its equilibrium value. Above the threshold for its onset, the shear stress increases very rapidly with pressure, exhibiting a very large pressure corresponding to an activation pressure of $10^7\,nm^3$ per molecule, implying a unit process for flow which is enormously larger than a single molecule.

It is important to understand what conditions determine whether a system exhibits a critical shear stress or viscous friction response to a shear. To do this, the full range of experimental conditions between those investigated by these two groups must be explored. The critical difference may be the amplitude of the shear motion [18.35] which in one study is much larger than the contact diameter, while in the other study is much smaller than this diameter. Also, very low level laboratory vibrations have been found to affect the frictional behavior [18.34]. Another topic which has not been addressed is the relationship of drainage experiments [18.23 24] to shear experimetns carried out on the SFA.

Although the external forces applied in the shear and drainage experiments are obviously very different, the motion of the entrapped molecules in both cases is constrained to be parallel to the interface. Perhaps the effective viscosities deduced from the two sorts of experiments can be related.

18.2.2 Single Asperity Techniques

Unfortunately, there are few materials which can be made smooth enough over a large enough surface area to be used in the SFA technique. Another approach to precisely defining a contact is to mimic the contact of a single asperity with a surface (Fig. 18.1d). The results can then be interpreted without the averaging implied in Amontons' Law. If the tip is small enough, contact with the surface can be limited to a region over which there are no defects on the surface.

There is a rather extensive literature concerning the contact of sharp tips with surfaces in vacuum, with and without sliding. In addition to normal and lateral force measurement, the contact resistance can be measured. Some measurements have been combined with a scanning electron microscope and transmission electron microscope to examine indentations and wear tracks, others with field ion and field emission spectroscopy to examine changes in the tip during contact. Among the interesting effects observed in these experiments are the development of strong metal-metal adhesion at zero loads, and friction at "negative loads".

When the contact area is reduced to that of several contacting atoms, and indentation depths are a few nanometers or less, inhomogeneities in the tip and surface may influence the contact mechanics. On this scale, a monolayer of contaminant will profoundly affect the attractive and adhesive forces. The behavior will also be influenced by the local crystal structure. Indeed, as the contact area between surfaces approaches atomic dimensions, the interface and its associated stress zone may be free of dislocations, leading to mechanical behavior approaching that of an ideal lattice. This idea has existed for some time [18.36, 37] although its careful examination has only been possible in recent years. *Maugis* et al. have related observed dislocation density to adhesion, friction, and microhardness of Al foils in contact with a fine tip [18.38]. The experiments indicate two different regimes exist, depending on the applied load. Below a critical load, the behavior is elastic so that the measured adhesion force is low and friction is near zero. As the load is increased, however, the range at which the load can act on a dislocation source increases, so that plastic deformation occurs, accompanied by increases in both the adhesive force and friction. When sliding, the threshold comes at a lower applied load, because the size of the shear stresses involved augments the effective applied load. This work and others [18.39, 40, 41] however, have shown that the elastic energy stored in dislocations represents 1% or less of the total frictional energy expended, and heat must be dissipated by other means.

The key role of dislocation density has been substantiated recently by *Pharr* and *Oliver*, who have reinvestigated the dependence of hardness on indentation

depth into Ag {111} surfaces [18.42]. A rapid increase in hardness of about a factor of two is observed as the indentation depth is decreased from 50 to 20 nm. In this range of indentation depths, dislocations are not observed to nucleate around the indentation, as they do at larger indentation depths. Thus, the increased hardness for small indentations may be the result of the confinement of dislocation activity to sub-surface regions.

Skinner and *Gane* have also investigated the friction and microhardness for sharp tips on a flat surface under small, and even 'negative' loads. Some controversy exists in these works concerning the effect of surface cleanliness. In their indentation experiments, Gane and co-workers [18.43, 44, 45] found that under certain conditions, the surface would not yield until it "punched" through, leaving a large indentation as the load was increased. This behavior was correlated with the presence of a carbon-containing polymeric film at the surface. The action of this film was believed to be one of preventing the spread of dislocations to the surface. *Maugis* et al. [18.38] cite the role of the contaminant film as one of reducing the attraction which would exist between two clean metals. This attraction, for fine metal tips, is strong enough to initiate plastic deformation even at zero applied load. The presence of such a strong attraction, which exists due to the natural strong short-range attraction between clean metals, is widely recognized, and has been observed by others [18.46, 47]. Intentional contamination of a clean nickel surface by oxidation has no effect on adhesion of a tungsten stylus until the oxide layer is several nm thick [18.47]. This topic has recently been reviewed [18.48] although it is worthwhile noting that determination of the hardness of a clean surface relative to a contaminated one is not yet fully understood.

a) The Nanoindenter. Many of the measurements cited above have utilized some kind of nanoindentor. Nanoindentation is a well-developed method for studying the elastic and plastic properties of surface materials to normal loads resulting in indentation depths between 10^{-8}–10^{-3} m [18.49]. Here, a standard indenter, usually a diamond pyramid, is loaded and unloaded from a surface while measuring the forces involved. For accurate measurements, the point of the indenter must be sharper than the diameter of the indent. Through these experiments, both the adhesive force and the microhardness of the materials can be investigated. Simultaneous measurement of contact resistance is useful for the estimate it provides of the contact area, and as a measure of the onset of contact during approach between conducting indenters and surfaces. *Chen* and *Hendrickson* [18.50] have demonstrated that nanoindentation can be accompanied by etch pitting and electron microscopy to image individual dislocations generated by the indentation where they intersect the surface.

Pethica, Oliver and co-workers have extended the technique to apply a desired load by magnetic coils, and monitor the tip displacement [18.51, 52, 53]. They have thus been able to observe the surprising robustness of thin oxide films and their effect on the contact mechanics. By applying a small, ac modulation to the tip, it is possible to measure the surface stiffness, $S = \partial P/\partial x$, with P the load and x the displacement. The attractiveness of this measurement is that the stiffness is related to the radius of the contact area a by a simple power law relationship $S = k \cdot aE^*$, where k is $\simeq 2$, and E^* the reduced elastic modulus, independent of the tip shape [18.54]. The resolution of this instrument allows the evaluation of stiffness, and thus contact radius, for contact areas on the atomic scale. Using this technique, near theoretical lattice strength was observed for a diamond tip on Cu and sapphire when the tip radius was 500 Å.

b) Field Ion Microscopy. Because of its power to both clean and image sharp tips with atomic resolution, special mention is given to the field ion microscope [18.55] which was invented by *Müller* in 1951 [18.56]. The potential of the FIM for studying tip-surface contacts was first exploited by *Nishikawa* and *Müller* who characterized the damage done to tungsten tips during contact with several types of metals [18.55]. *Buckley* reports that when a tungsten tip contacts a gold surface, only enough gold is transferred to the surface to create a dense covering of gold trimers [18.3]. From a platinum surface, epitaxial transfer to an iridium tip is found except when the interface is subject to vibration, in which case platinum clusters are found on the tip. In a FIM study of contact of tungsten and platinum tips touched to platinum surfaces with $\simeq 10^{-6}$ N loads, *Walko* finds that tip damage extends only 5–15Å deep [18.57]. By determining as a function of load the area over which tip damage occurred, it was determined that the contact followed Hertz's equations for elastic contact.

c) Other UHV Work. The concern, mentioned above, of deviation from clean surface behavior due to a contaminant film, is particularly strong when high energy surfaces such as active metals are under investigation. In these cases, the experiment should be performed in UHV. Standard surface science instrumentation which is typically available in UHV chambers can be used to monitor the phenomena occurring. *Buckley* [18.3 58] and *Pepper* [18.59] have proven the effectiveness of such tools as LEED, Auger spectroscopy, field ion microscopy, and the atom probe in studies of adhesion, wear, and the associated transfer of material. *Pollock* has made a careful analysis of surface forces and the effect of nanometer-scale topography aided by a single asperity UHV experiment [18.46].

Pepper has correlated the friction of Cu on diamond in vacuum with the presence or absence of unoccupied surface states in the bandgap [18.60]. The friction coefficient for a polished surface, annealed at 750°C was $\simeq 0.1$. Annealing above 850°C or bombarding with 500 eV electrons, which presumably dehydrogenates the surface, results in an increased friction coefficient of 0.5. Exposure of this state to excited hydrogen reduces the friction coefficient. Energy loss spectra showed the presence of a feature at 284 eV (in the bandgap) could be correlated with the conditions in which high friction was observed. Formation of an interfacial bond involving the gap state is postulated. The combination of UHV surface techniques with tribological measurements is being actively pursued by several groups [18.61, 62, 63].

d) Scanning Tunneling and Atomic Force Microscopy. The demonstration of single atom resolution by scanning tunneling microscopy (STM) in 1983 greatly expanded the horizons for the single-asperity technique [18.64]. The reader is referred to Chap. 16 (Avouris) and Chap. 14 for reviews of STM experiments and theory [18.66] and to scanning probe techniques in general (Chap. 15). Obviously, the STM shows great potential for determining the topography of surfaces of tribological interest [18.65]. Early on, it was recognized that tip-surface forces could play a role in the imaging process [18.66], an effect thought to be responsible for the anomalously large atomic corrugations observed on graphite [18.67, 68, 69]. Tip-surface forces are among the many effects demonstrated to achieve surface modification in the STM, which has been promoted as a technique for very high density recording of information. The scanning tip can be used both to modify the surface and to image the modification and any spontaneous changes at the surface. This approach was used on a gold {111} surface by *Jaklevic* and *Elie* [18.70]. They created craters $\simeq 10$ Å deep and $\simeq 100$ Å wide by tip contact, and, over a period of about an hour, observed the healing of the craters by surface diffusion. Other examples of such surface modifications, which are prototypes for both ultrahigh resolution lithography and wear at the atomic scale, are discussed in Chap. 15.

As its inventors, *Binnig*, *Quate* and *Gerber*, have emphasized, the atomic force microscope (AFM) is simply a stylus profilometer updated with technology developed for the STM [18.71]. In the atomic force microscope, the forces normal to the surface exerted by the surface on the tip are measured by the deflection of a cantilever on which the tip is mounted. As the surface is scanned past the tip, the variation in tip-surface forces reveals the topography of the surface. The most critical aspect of the AFM is reliably and accurately sensing the sub-angstrom deflection of the cantilever. Although this tunneling method offers unsurpassed sensitivity, the tunneling junction exerts an extraneous force on the cantilever, and is unreliable. Soon after the first AFM was demonstrated, simple [18.72] and heterodyne [18.73] optical interferometry were introduced in place of tunneling to detect the cantilever deflection. Fiber interferometry [18.74], laser deflection [18.75], and capacitance [18.76, 77, 78] methods have also been developed.

The force-sensing sensitivity of an AFM is ultimately limited by the noise level of the deflection sensing technique and by the unavoidable thermal excitation of the lever. However, .01 Å noise levels are achievable over a 100 Hz bandwidth. Although low lever force constants k_l give high sensitivity, they also allow the tip to "snap-in" to the surface under the influence of the attractive force of the tip. A good compromise value is $k_l = 20$ N/m, for which 0.01 Å gives a noise level of 2×10^{-11} N (1 N $\simeq$ 100 gram weight). For comparison, the force required to break a single chemical bond is about 10^{-8} N, while a single van der Waals bond breaks at about 10^{-10} N. Thus the AFM is sensitive enough to image individual atoms without breaking chemical bonds and to accurately measure forces (including frictional forces) exerted on a single atom of the tip.

Many AFM images showing atomic features have now been reported, but only on layered compounds such as graphite or boron nitride. Since almost all

of the AFM work to date has been in air, such compounds are used because they can be cleaved to give unreactive surfaces. There have been near-atomic resolution images recorded on surfaces of polymers, organic crystals, and biopolymers [18.79]. To obtain a high resolution image, the instrument must be operated in the "respulsive mode", with a force of 10^{-9} to 10^{-7} N between the tip and the surface. The simple fact that two-dimensional atomic resolution images can be repeatedly scanned on the same region of a surface is very significant from a tribological perspective because the tip must be sliding across the surface with no wear. These AFM images represent the most direct evidence to date that wearless sliding is possible. Since a force of 10^{-7} N is much larger than required to break a single chemical bond, it seems surprising that such a large load can lead to atomic resolution images. This question has been the subject of some modeling calculations of the tip-surface interaction [18.80] which we will discuss in more detail below. These calculations have emphasized that, because of the layered structure of graphite, a deep and laterally extended deformation of the surface occurs at modest loads, so that tip-surface contact occurs over more than just one atom. It may be that, while imaging in air, most of this contact is lubricated by a mobile adsorbed layer with only a single tip atom "poking through" it to do the imaging [18.68]. While imaging a layered compound, it is also possible for a flake to break off of the surface and adhere to the tip. If the flake remains oriented with respect to the surface, the normal force of the surface on the tip will vary with the periodicity of the surface [18.81].

Many AFM images show anomalous features which are apparently the result of forces parallel to the surface. A featureless region appearing immediately after the surface changes direction is likely due to sticking of the tip to the surface [18.82]. "Grooving" is sometimes observed, in which two successive x line scans taken at slightly differing y values are very different [18.82]. It has been suggested that this occurs when the tip which has been stuck in a row of the surface lattice suddenly slips to an adjacent row. Frictional forces have also been invoked to explain lattice distortion observed at the beginning of line scans in repulsive mode imaging [18.83]. The effect of frictional forces would be more clearly elucidated by comparing line scans obtained in opposite scanning direction while the sample is oscillated under the tip.

The first AFM study of frictional forces at atomic-level resolution was reported by *Mate* et al. and *Erlandsson* et al. for the 2000 Å radius tip of a tungsten wire sliding on graphite [18.84] and mica [18.85] surfaces in air. This work used an AFM based on optical interferometry in which the sample and tip were rotated by 90° from the usual orientation used for mapping topography (Fig. 18.5a), so that lever deflections detected parallel to the surface measure the frictional force. The frictional force on both the graphite and mica surfaces shows a clear pattern with the period of the sample surface (Fig. 18.5b), an effect most easily seen in two-dimensional scans [18.84, 85].

The force varies in a stick-slip pattern, which appears to be very much like that discussed above for the surface force apparatus experiments. Here, the origin of this effect is not the velocity dependence of the frictional force, but rather,

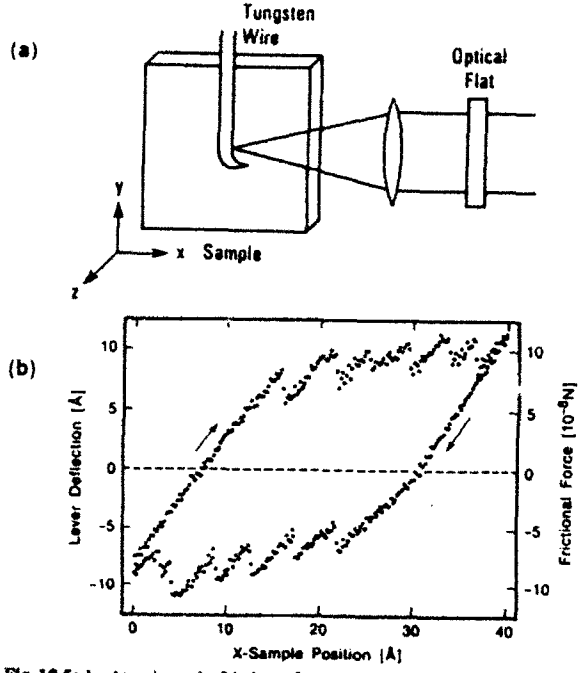

Fig. 18.5a,b. Atomic scale friction of a tungsten tip on a mica surface in air (a) Schematic representation of tip, sample, and interferometer geometry. (b) The lever deflection and corresponding frictional force in the x direction as a function of sample position as the sample is scanned back and forth under the tip. From [18.85]

its dependence on position. To understand this effect and other aspects of AFM experiments, the tip and cantilever cannot be considered simply as a probe of tip-surface forces. Rather, the dynamics of the tip moving in response to forces exerted by the surface and the cantilever must be considered. Because surface features are encountered at a frequency smaller than the lever's resonant frequency, the tip always comes to an instantaneous mechanical equilibrium (total force zero) in response to the combined force of the lever and sample. Considering only displacements of the sample and tip along the scanning direction x, and noting that the tip-sample force F_s depends only on the instantaneous relative position of the tip and sample, the total force F on the tip can be written as a function of the tip position x_t and the sample position x_s

$$F = -k_l x_t + F_s(x_t - x_s) .$$

The first term represents the force exerted by the cantilever on the tip, and has a negative slope with respect to x_t, pushing more towards negative x_t as x_t increases. If F_s is not constant, it will have regions of both positive and

negative F_s'. For any region where $dF/dx_t > 0$, the tip will not be at a stable equilibrium. If the tip encounters such regions, it will slip until it finds a region where $dF/dx_t < 0$. The effect can be likened to pulling a stick across successive boards of a picket fence. This equation predicts that, for a given lever, if the frictional force is made low enough so that dF/dx_t is always less than k_l, no slipping will occur, and the tip position will vary smoothly with the sample position, while still reflecting the periodic character of the lattice. This change between discontinuous to continuous behavior has been observed on graphite [18.84].

An elastic analysis of the graphite and mica friction experiments indicates that the tip-surface contact covers many unit cells of the surface, and for the larger loads used for graphite, is as much as 1000 Å across [18.84]. In view of this fact, it seems surprising that the surface periodicity is directly manifested in the frictional force, because the large tip contact area would average any variations across the unit cell. However, the contact is not uniform and undoubtedly consists of the contact of many nm-scale asperities, which are probably responsible for the linearity of the frictional force with load. These contacts will not be spaced uniformly, and so will not completely average out the lateral dependence of the frictional force.

Another possibility which could explain the large force modulation is that flakes of the flat surface break off and remain on the tip, remaining in orientational registry with the surface. Such flakes have been postulated to be present during STM imaging of graphite [18.81]. In some recent low-resolution AFM experiments, care was taken to measure the frictional force before extensive sliding had occurred which might transfer a flake to the tip [18.76]. In this case the measured friction coefficient (0.28) was much larger than the value of 0.01 that had been observed after extensive contact.

Using the AFM in the nonscanning, nanoindenter mode, *Burnham* and *Colton* [18.86] and *Neubauer* et al. [18.76] have studied the elastic indentation of a graphite surface with hard metal tips of several thousand angstrom radii. The apparent surface stiffness is much lower than is to be expected from the known graphite elastic constants, but for indentation depths greater than 100 Å, the stiffness approaches its expected value [18.76]. This effect may be due to the partial delamination of graphite flakes, which are pushed back into the surface by the applied load. This sensitive technique was recently extended to surfaces consisting of Langmuir-Blodgett (LB) films, where it was shown that substituting the exposed methyl group of stearic acid with the trifluoromethyl group led to a noticeable variation in the tip-surface forces [18.87].

Blackman et al. [18.88] have recently used the AFM to study the tribology in air of a tungsten tip ($\simeq$ 1000 Å radius) on LB films of cadmium arachidate deposited on the oxidized Si{111} surface. From friction loops of the type displayed in Fig. 18.5b, they found that for a monolayer film, friction was not proportional to load, but that the derivative of friction vs. load began at 0.1 for small loads, increased to 0.6 at intermediate loads, and fell back to about 0.3 for the maximum load of 6×10^{-8} N. Using the AFM tip to image by attractive

VDW forces, the monolayer was found to be undamaged by the friction although it was swept free of "molecular debris" adhering to the surface. In contrast, when a thicker film of five layers was used as a lubricant, the first four layers were easily worn away. Using the AFM tip as an indenter, the Meyer's hardness of a 7 layer film was determined to be 0.6 MPa.

Albrecht has studied self-assembled films which, in contrast to LB films, are attached to the surface through a covalent bond [18.82]. Using a microfabricated SiO_2 tip, and forces up to 10^{-6} N, it was possible to wear away a monolayer of octadecyl phosphate, but not a monolayer of octadecyltrichlorosilane. The latter undergoes chain polymerization (cross-linking) at the base, in addition to the chain-substrate bond. The AFM results may be compared with macroscopic studies, performed on both LB [18.89,90,91] and self-assembled [92,93] films, which show that one layer provides all of the lubricating action. Interestingly, the strength of the monolayer-substrate bond plays no obvious role in the microscopic studies, whereas the intramolecular cohesion, altered by varying the chain substituents, does. More work needs to be done at the atomic level to elucidate the importance of substrate bonding and intramolecular forces in these lubricants.

For tribological studies of well-characterized surfaces, *Neubauer* et al. have recently incorporated an AFM into a UHV system equipped with sample and tip transfer airlocks and standard surface analysis equipment [18.78]. This AFM is the first to sense the lever deflection simultaneously both parallel and perpendicular to the surface. This enables direct measurement of the load during a friction experiment, and allows tip-surface dynamics to be followed in great detail. Furthermore, the surface can be imaged by repulsive tip-surface forces after measuring friction loops. To sense the lever deflection both parallel and perpendicular to the surface, a dual capacitance sensor is employed (Fig. 18.6a). In this capacitance method, a radio frequency oscillating voltage is applied to the sensor plates, which are positioned about 1000 Å from the lever. Angstrom-scale deflections of the lever cause $\simeq 10^{-17}$ F variations of the capacitance between the lever and plates, which are sensed by a detector locked onto the radio frequency.

This new AFM was used to characterize the indentation and friction of an iridium tip on a Au{111} surface in UHV [18.97]. To obtain these data, the sample is oscillated back and forth parallel to the sample direction while being advanced toward and retracted from the sample. As the sample is advanced toward the tip, the tip snaps into the surface when the derivative of the attractive force exceeds the lever force constant (Fig. 18.6b). The sample is advanced until the load is about 10^{-7} N, and then is retracted. The curve of lever deflection vs. sample position is reversible and the slope is near one, indicating that the tip-surface contact undergoes very little elastic or plastic deformation. The snap-out of the lever establishes that the adhesive force is about 3×10^{-7} N. The frictional force computed from the height of friction loops of the sort shown in Fig. 18.5b is also displayed. Interestingly, the friction shows a very strong hysteresis, changing much more gradually when the load is decreased than when it is increased. While the dependence of friction on load is not strictly linear, the approximate friction coefficient upon increasing the load is 1.0, while upon decreasing the load it is 0.4. Considering that very little hysteresis is observed in the motion of the lever perpendicular to the sample, the changing frictional behavior is evidently associated with very subtle changes in the tip-surface interface. For these experiments, the surface was clean as verified by LEED and Auger analyses. The tip was cleaned by heating and ion bombardment before these experiments, but measurements of the tip-surface contact resistance indicate that some contaminant prevented full tip-surface contact.

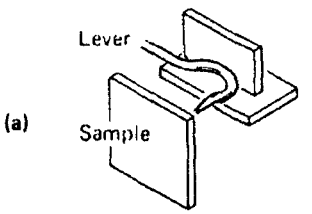

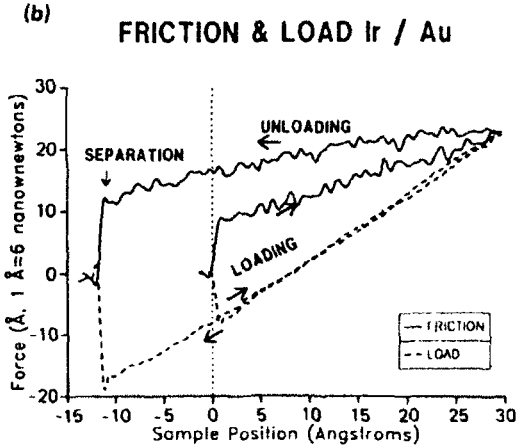

Fig. 18.6a,b. Friction of an iridum tip on a Au {111} surface in vacuum. (a) Schematic representation of geometry used to simultaneously measure friction and load by capacitance measurement. (b) Variation in frictional (lateral) and loading (normal) forces as the sample is pushed into the tip with simultaneous oscillation in the sample plane. From [18.18]

In order to better understand the head-disk interaction in magnetic disk recording devices, the AFM has been used to characterize the friction and adhesion properties of magnetic disks [18.95]. In addition to its usefulness in probing the dynamics of tribological interactions, the AFM is a very useful surface analytical tool for characterization of tribologically interesting surfaces. For example, the AFM has been used to correlate the topography of hard carbon films with their tribological properties [18.83]. *Mate* et al. have used the AFM as a "dipstick" to profile the thickness of lubricant coatings [18.96,97] and have profiled the liquid-air interface by sensing van der Waals forces [18.96].

Contact electrification refers to the exchange of charge which occurs between two surfaces. When electrification is caused by the repeated contact of asperities during rubbing, it is referred to as tribocharging. The role of rubbing is to repeatedly make and remake asperity contacts. Between metals, electrification

results from the electron flow which must occur to equilibrate the fermi level of two contacting metals of different work functions. Tribocharging of insulators is not at all understood, and has recently been investigated on a small scale by force microscopy [18.98]. *Terris* et al. have developed a method for detecting force gradients from charges as small as 6, with a lateral resolution of 0.2 μm [18.99]. This resolution, which is 3–4 orders of magnitude better than previous tribocharging studies, enables the observation of a bipolar charge distribution: when a Ni tip of 0.1 μm radius is touched to a polymethyl methacrylate surface, a charged region of 10 μm diameter is formed. Within this region are both positive and negative charges which are stable on the surface for days before decaying away [18.98].

18.3 Theoretical Descriptions of Tribology

Because of the complexity of tribological interfaces and the difficulty of obtaining reliable data from a "buried" sliding interface, interpretation of experimental data is bound to be ambiguous. Theoretical molecular dynamics models, even if simplified, provide the advantage of being able to study a well-defined system, and to follow directly any desired variable of the system. The relation of directly measurable properties to the atomic dynamics can be determined directly. Using empirical or *ab initio* interatomic potentials, molecular dynamics calculations integrate the classical equations for motion of atomic nuclei. Although, ultimately a quantitative prediction of experiment requires realistic interatomic potentials, a great deal of phenomena can be elucidated with less accurate potentials.

18.3.1 Simplified Model of Wearless Friction

As discussed above in the general overview of tribology, in most cases, friction is associated with wear. For example, according to the adhesive theory of friction, shear occurs within the contacting asperities, and the energy is dissipated during the movement of dislocations involved in the plastic deformation of asperities. The AFM and SFA results obtained recently seem to show clearly that friction can occur without wear, and *McClelland* has recently presented a discussion of friction in this regime, using a highly simplified model [18.100]. The motivation of such models is not to provide a realistic comparison to experiment, but rather to clarify important mechanisms of interfacial energy dissipation which can be obscured in complex calculations. Figure 18.7a presents a schematic representation of two atomically smooth surfaces sliding over each other in such a way as to generate no wear. We assume that each solid is bound together by strong (chemical, metallic, or ionic) *intrasolid bonds*, but that, because the valency of each atom at the interface is satisfied, the *intersolid* interaction across the interface is weak, consisting only of van der Waals interactions. Then, when the lower solid A is slid across the upper solid B, the interfacial interaction is not

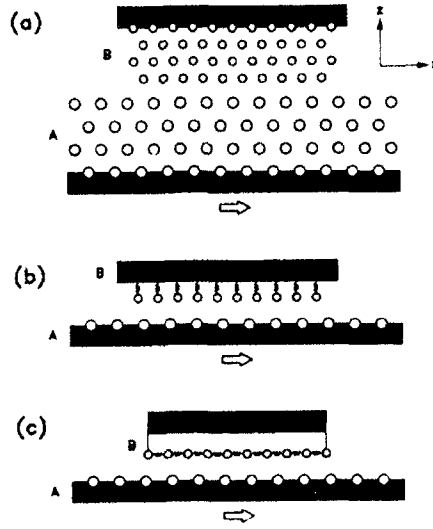

Fig. 18.7a–c. Models of wearless friction. (a) Solid A sliding across solid B in two dimensions. (b) Independent oscillator model. (c) Frenkel-Kontorova model. The black areas represent rigid supports of the atoms. From [18.100]

strong enough to break any of the bonds within either solid. However, it can, in principle, move the atoms within the solid, thus generating phonons and dissipating energy. For purposes of discussion, for each solid, a row of atoms far from the interface is attached to a rigid "handle". The top handle is held fixed while the bottom handle is translated slowly across the other solid.

To understand qualitatively how energy can be dissipated for this type of interface, a simplified "independent oscillator model" is analyzed, which is similar in spirit to a model described long ago by *Tomlinson* [18.101]. In this simplified model, solid A has been replaced by a single row of atoms anchored to a rigid handle while solid B has been replaced by non-interacting atoms, bound as damped harmonic oscillators to the B handle.

Suppose that the handle of the solids are held at absolute zero temperature during sliding. Noting that for reasonable sliding speeds, the time scale for sliding over a single atom is many orders of magnitude less than a vibrational period, we see that a particular B-atom, B_0, will at all times move toward achieving a position of lowest energy in the potential energy governing its motion. As illustrated in Fig. 18.8a, this potential V_S is the sum of two components: V_{BB}, a simple harmonic potential attaching it to its handle, and V_{AB} the periodic interfacial potential arising from the interaction with the A-atoms [18.103]. In the left column of the Fig. 18.8, V_{AB} is a rather strong hard-sphere interaction.

Following the left column of Fig. 18.8, as A is slid, B_0 at first moves gradually, following the minimum of V_s, until, at the point diagrammed in frame e, the atom is suddenly released because the minimum has disappeared. This disappearance occurs when the repulsive (concave downward) part of V_{AB} is overcome by the increasingly sloped concave upward part of V_{BB}. When the

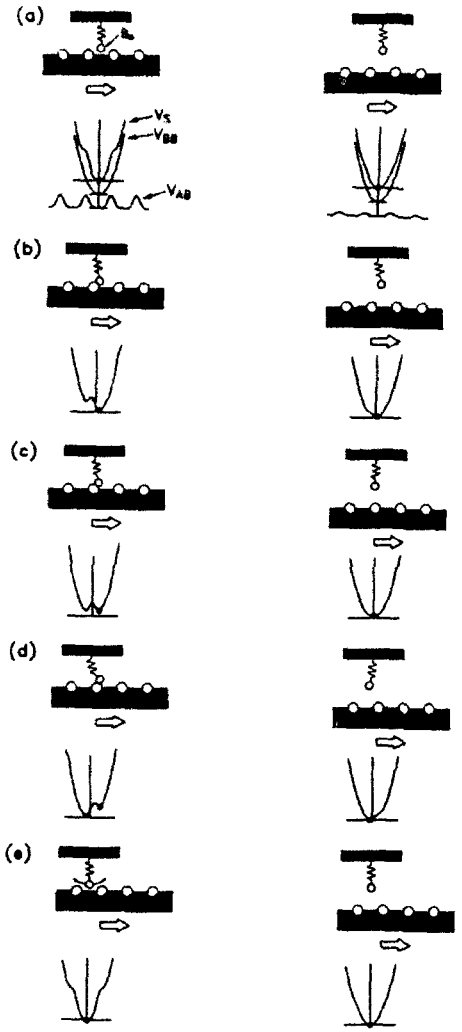

Fig. 18.8a–e. Motion of an atom B_0 of B in the independent oscillator model of friction. Left and right columns diagram strong and weak interfacial interactions, respectively. The top panel diagrams the relevant potentials, while subsequent panels illustrate the response of B_0 represented by a black dot on V_S to progressive sliding of A, as determined by the potential sum V_S plotted below each diagram. From [18.100]

B-atom is released, it falls suddenly down into the nearby minimum, becoming vibrationally excited in the process. This vibrational excitation is dissipated into the surrounding solid. The dissipation of energy results in friction.

A key feature of friction is that the frictional force opposes the direction of motion, so that it must reverse when the sliding direction is changed. How this reversal occurs in the independent oscillator model can be discovered in the left panel of Fig. 18.8c. Because solid A has been moving from left to right, the

B-atom sits in the right minimum of a symmetric V_S, and, therefore, exerts a force to the right on solid B.

One might expect that the frictional force would be roughly proportional to the interfacial interaction, but in fact the dynamics changes *qualitatively* as V_{AB} is reduced. The right column of Fig. 18.8 traces out the dynamics for a V_{AB} one fifth the size of that diagrammed in the left column. Following the sequence of frames, it is seen that there is no "plucking" step to release energy as there was for higher V_{AB}. Plucking can only occur when there is a disappearing local maximum in V_S, which happens only when a portion of V_{AB} has a downward curvature greater than the upward curvature of V_{BB} (the force constant of the B bond).

The situation where two solids interact by physical interactions while they are each held together by stronger bonds actually corresponds to the right column of Fig. 18.8. We conclude that in this case the friction vanishes. It should be emphasized that the origin of this frictionless behavior is the reversible adiabatic response of the system to the slow external perturbation. The conclusion of frictionless motion is not limited to the highly simple independent oscillator mode. As emphasized by *Sokoloff* [18.102], the same result arises in the Frenkel-Kontorova model, where the interaction between atoms is included, but all other forces on the interfacial atoms are neglected (Fig. 18.7c). In the Frenkel-Kontorova model, however, the effect of the relative lattice spacing can be seen. When the two interacting solids are commensurate (i.e., when their lattice spacings are related by a simple ratio of whole numbers) the force acts in phase on many atoms to produce a concerted motion of the interfacial atoms of each solid. The effective restoring force for such a concerted motion is very small, so that in this case energy dissipation occurs.

These concepts have been confirmed by molecular dynamics calculations [18.100]. In the simple model presented here, thermal excitation would reduce friction if the temperature were high enough to activate the B_0-atoms over the V_s barrier at a rate competitive to sliding. A similar model has been applied to discuss the effect of adsorbed molecules at a sliding interface [18.100].

18.3.2 Molecular Dynamics Studies of Shearing Solids

Recently, the Georgia Tech group has reported several large scale molecular dynamics simulations of interfacial shear using reasonable representations of the interatomic potentials. In one such simulation, two solids, each of which had 9 layers containing 70 atoms interacting by Leonard-Jones potentials, were placed in contact and sheared across each other [18.103–105]. One solid (the soft solid) was less weakly bound than the other, and three-dimensional periodic boundary conditions were employed. As an increasing shear stress was applied across the two solids, an elastic response was first observed, followed by stacking fault formation and eventuall yield.

When the lattice constant parallel to the shear direction was set the same for the two solids, shear occurred not at the interface, but in the softer solid, an

observation in general agreement with experimental experience. But when the lattice constant for the softer solid was set to be 50% larger than that of the hard solid, the yield stress was lowered because "pinning" no longer occurred at the interface. Yield occurred not within the soft solid but at the interface. In the context of the above discussion of frictionless sliding, we expect a non-zero friction in this case both because the intersolid bonds are not much weaker than the intrasolid bonds, and because the lattices are commensurate with a spacing ratio of 3 to 2.

Modeling of sharp tips sliding across surfaces is relevant both to asperity contact during sliding of two surfaces and to imaging in force microscopy. *Landman* et al. [18.104–107] have discussed the sliding of a Si {111} surface across a 16 atom {111} facet of a dynamical Si tip. This is clearly a "reactive" system, in which the surface can form strong bonds with the tip. Accordingly, when the tip is brought into contact with the surface and then withdrawn, a plastic "neck" is formed between the two, consisting mostly of tip atoms. On the other hand, if the tip is not withdrawn, but is simply slid over the surface, no damage occurs to surface or the tip. A striking feature of these results is the clear manifestation of abrupt behavior in the frictional force (Fig. 18.9d) of the sort discussed in the independent oscillator model above. The slips are not absolutely abrupt because the sliding velocity is so large, making the time interval in the figure quite short.

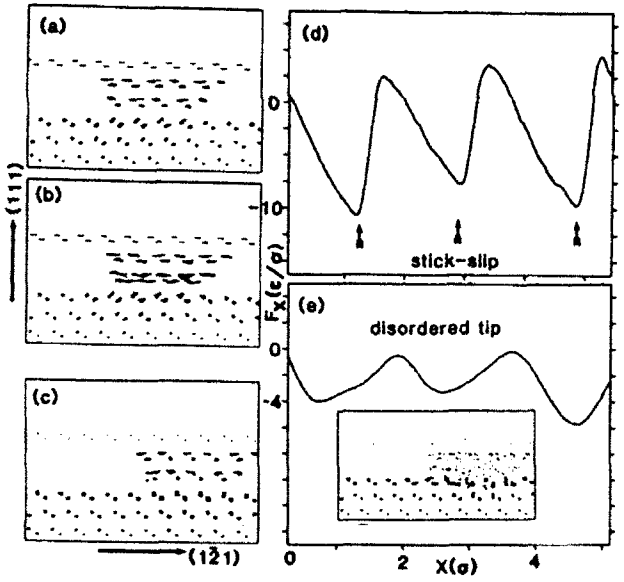

Fig. 18.9a–e. Sliding of a silicon tip across a silicon surface. (a–c) Particle trajectories viewed along the (10$\bar{1}$) direction just before (a) and after (b) an atomic scale stick-slip event, and (c) towards the end of the scan. (d) The frictional force. (e) The frictional force for an amorphous tip. From [18.106]

From the figure, it is clear that the interfacial atoms have become greatly excited during the slip process. Interestingly, a disordered tip shows a frictional force which also varies with the period of the lattice, but no distinct slips are visible (Fig. 18.9e) probably because the friction is composed of minor unsynchronized individual slips across the interface.

The relation of the STM and AFM imaging processes to tribology has been emphasized above. Normal forces between the tip and surface have been the subject of several theoretical calculations involving varying degrees of sophistication in their treatment of electronic structure and tip and surface deformation. Topics addressed include tip geometry [18.108, 109], elastic deformation of the substrate [18.80, 109, 110], detection of intercalation atoms [18.110], the effect of tip-surface forces on STM topographs [18.67, 111] and tip-induced modifications of the surface electronic structure [18.111, 112]. The possibility of jumping of a tip to a surface due to the flexibility not of a cantilever but of the tip itself has been discussed [18.113, 114], as have the universal aspects of interaction forces between metal tips and surfaces [18.115].

18.3.3 Molecular Dynamics Studies of Thin Fluid Flow

The importance of thin liquid films in lubrication and in recent SFA experiments has motivated theoretical studies of liquid flow in small channels. A recent molecular dynamics study addressed the shearing of a one to five atom thick Lennard-Jones fluid between two flat, rigid, ordered surfaces of atoms of the same type [18.116]. When the surfaces are held fixed, they induce freezing of the intervening fluid into a commensurate structure. Sliding of one surface over the other can occur only when a critical shear stress is exceeded, at which point the intervening solid becomes less dense and liquifies.

In the SFA experiments, it is the load, not the spacing, which is held fixed, and such a constraint was applied in the simulation of *Landmann* et al. of a three layer liquid [18.105]. For static surfaces, this liquid also orders. At the onset of shear, the thickness of the confined liquid is reduced by one layer, but residual liquid ordering is still manifested by oscillation of the frictional force during sliding.

The flow of a very narrow atomic liquid through a smooth pore of square cross-section about 6 molecular diameters wide was reported by *Bitsanis* et al. [18.117]. The viscosity was found to be less than that of the bulk liquid, but could be accounted for accurately by assigning a local viscosity equal to that of a bulk fluid with a density equal to that of the density found in the pore simulation.

18.4 Summary and Future Directions

During the last few years, tremendous advances have been made in the development of experimental and theoretical tools necessary for attaining a scientific

understanding of tribology. Atomically resolved images of surfaces in real space can be generated by scanning tunneling and atomic force microscopy. Furthermore, the mechanical properties of the surfaces themselves can be determined with atomic resolution. Using the surface force apparatus, the angular dependence of adhesive forces has been revealed. The static and dynamic forces both normal and parallel to the surfaces have been determined as a function of the numbers of layers on the surface. Using the atomic force microscope, the periodic structure of a surface has been detected in the frictional force. Due to the increasingly widespread capability of doing large scale numerical computation, the experimental advances have been matched by realistic molecular dynamics simulations of sliding interfaces.

The possibilities are so new that they have barely been explored. For example, using an STM/AFM tip, it is now possible to image a surface (including its defects) with atomic resolution, measure the frictional force and load as a single apex atom of the tip slides across the surface, and then use the same tip to monitor atomic-scale defects in the surface. This experiment could be made perfectly well-defined if the tip were imaged at atomic resolution by field ion microscopy. Already reproducible manufacture of single atom tips has been demonstrated, and FIM-characterized tips have been used for STM [18.118]. Another approach for better characterized tribology experiments is to study surfaces of low specific surface free energy, such as LB and self-assembled monolayers, which do not require UHV to remain clean.

An important direction for the surface force apparatus experiments will be the extension of this technique to surfaces other than mica. The mica surfaces can be chemically modified, and recent results on sapphire [18.119] and glass [18.120] are promising.

There have been no direct experimental studies of the fate of energy dissipated at a sliding interface. Eventually, this issue may be addressed by spectroscopically detecting phonons created at the sliding interface.

At present, a major advantage of molecular dynamics approaches is that, in contrast to the experiments, the systems that are being studied are well-defined. In the future it will be important to use more accurate representations of inter-atomic potentials. A particular challenge will be to model slow phenomena which have a molecular basis, for example, stick-slip motion in the surface force apparatus.

Even with an accurate atomic scale picture of a tribological interface, a complete understanding requires a proper account of the very heterogeneous rough interface. Fractal treatments offer a possible approach to this problem [18.121].

The practical movitation for a fundamental understanding of tribology remains strong, with developing applications in micromechanics, space craft, medical implants, and information storage devices. We can look forward to a fruitful interplay of applied and fundamental studies during the next few years.

Acknowledgements. We are grateful to A. Homola, A. Gellman, S. Granick, R.G. Horn, J.N. Israelachvili, U. Landmann, and C.M. Mate for providing preprints of their work. Partial support of the ONR under contract N00014-88-C-0419 and the AFOSR under contract F49620-89-C-0068 is gratefully acknowledged. S.R.C. acknowledges the support of the Myron A. Bantrell Trust through a Chaim Weizmann postdoctoral fellowship.

References

18.1 L.E. Pope, L.L. Fehrenbacher, W.O. Winer (Eds): *New Materials Approaches to Tribology Theory and Applications* (Materials Research Society Symposium Proceedings **140**, Pittsburgh 1989)
18.2 J.N. Israelachvili: *Intermolecular and Surface Forces* (Academic, New York 1985)
18.3 D.H. Buckley: *Surface Effects in Adhesion, Friction, Wear, and Lubrication* (Elsevier, Amsterdam 1981)
18.4 G. Heinicke: *Tribochemistry* (Hanser, Munich 1984)
18.5 W.R. Loomis (Ed.): *New Directions in Lubrication, Materials, Wear, and Surface Interactions* (Noyes, Park Ridge 1985)
18.6 A.D. Sarkar: *Friction and Wear* (Academic, London 1980); J. Halling: *Introduction to Tribology* (Wykeham, London 1976); N.P. Suh: *Tribophysics* (Prentice Hall, New York 1986)
18.7 I.N. Sneddon: Int. J. Eng. Sci. **3**, 47 (1965)
18.8 J.A. Greenwood, J.H. Tripp: J. Appl. Mech. March 1979, p. 153; J.A. Greenwood: J. Lubrication Tech. Jan. 1967, p. 81; J.A. Greenwood, J.B.P. Williamson: Proc. Roy. Soc. Lond. 295, 300 (1966)
18.9 J.N. Israelachvili, D. Tabor: Proc. Roy. Soc. Lond. A **331**, 19 (1972)
18.10 D. Tabor, R.H.S. Winterton: Proc. Roy. Soc. Lond. A **312**, 435 (1969)
18.11 J.A. Pryde: *The Liquid State* (Hutchinson Univ. Library, London 1966)
18.12 F. Kohler: *The Liquid State* (Verlag Chemie, Weinheim 1972)
18.13 P. Kruus: *Solids and Solutions: Structure and Dynamics* (Dekker, New York 1977)
18.14 W. van Mege, I.K. Snook: J. Chem. Phys. **74**, 1409 (1981)
18.15 N.I. Christou, J.S. Whitehouse, D. Nicholson, N.G. Parsonage: Symp. Faraday Soc. **16**, 139 (1981)
18.16 G. Rickayzen, P. Raymond: in *Thin Liquid Films*, ed. by I.B. Ivanov (Dekker, New York 1985) Chap. IV
18.17 F.F. Abraham: J. Chem. Phys. **68**, 3713 (1978)
18.18 I.K. Snook, W. van Megen: J. Chem. Phys. **70**, 3099 (1979)
18.19 R.G. Horn, J.N. Israelachvili: J. Chem. Phys. **75**, 1400 (1981)
18.20 H.K. Christenson, R.G. Horn: Chem. Phys. Lett. **98**, 45 (1983)
18.21 P.M. McGuiggan, J.N. Israelachvili: in *Characterization of Structure and Chemistry of Defects in Matter*, Mat. Res. Soc. Symp. p. 349 (1989)
18.22 P.M. McGuiggan, J.N. Israelachvili: Chem. Phys. Lett. **146**, 469 (1988)
18.23 D.Y.C. Chan, R.G. Horn: J. Chem. Phys. **83**, 5311 (1985)
18.24 J.N. Israelachvili: J. Colloid Interface Sci. **110**, 263 (1986)
18.25 A. Tonck, J.M. Goerges, J.L. Loubet: J. Colloid Interface Sci. **126**, 150 (1988)
18.26 J.M. Georges, J.L. Loubet, A. Tonck: Mat. Res. Soc. Symp. Proc. **140**, 67 (1989)
18.27 M.J. Mathewson, H.J. Mamin: Mat. Res. Soc. Symp. Proc. **119**, 87 (1988)
18.28 A.I. Bailey, J.S. Courtney-Pratt: Proc. R. Soc. London A**227**, 500 (1955)
18.29 B.J. Briscoe, B. Scruton, F.R. Willis: Proc. R. Soc. London A**333**, 99 (1973); B.J. Briscoe, D.C.B. Evans: Proc. R. Soc. London A**380**, 389 (1982)
18.30 J.N. Israelachvili, P.M. McGuiggan, A.M. Homola: Science **240**, 189 (1988)
18.31 P.M. McGuiggan, J.N. Israelachvili, M.L. Gee, A.M. Homola: in *New Materials Approaches to Tribology: Theory and Applications*, ed. by L.E. Pope, L.L. Fehrenbacher, W.O. Winer: Mat. Res. Soc. Symp. Proc. **140**, 51 (1989)
18.32 A.M. Homola, J.N. Israelachvili, M.L. Gee, P.M. McGuiggan: J. Tribology, to be published
18.33 J. Van Alsten, S. Granick: Phys. Rev. Lett. **61**, 2570 (1988)
18.34 J. Van Alsten, S. Granick: Tribology Trans, in press
18.35 J. Van Alsten, S. Granick: Langmuir, in press
18.36 H. Bückle: "Progress in Micro-Indentation Hardness Testing", Metallurgical Reviews (London, Institute of Metals), **4**, 49 (1959)
18.37 B.W. Mott: *Microindentation Hardness Testing* (Butterworths, London 1957)
18.38 D. Maugis, G. Desalos-Andarelli, A. Heurtel, R. Courtel: ASLE Trans. **21**, 1 (1976)
18.39 R. Feder, P. Chaudhari: Wear **19**, 109 (1972)
18.40 G. Andarelli, D. Maugis, R. Courtel: Wear **23**, 21 (1973)
18.41 N. Gane, J. Skinner: Wear **25**, 381 (1973)
18.42 G.M. Pharr, W.C. Oliver: J. Mater. Res. **4**, 94 (1989)
18.43 N. Gane, F.P. Bowden: J. Appl. Phys. **39**, 1432 (1968)

18.44 N. Gane: Proc. R. Soc. Lond. A 317, 367 (1970)
18.45 N. Gane, J.M. Cox: Philos. Mag. 22, 881 (1970)
18.46 Q. Guo, J.D.J. Ross, H.M. Pollock: Mat. Res. Soc. Symp. Proc. 140, 51 (1989)
18.47 M.D. Pashley, J.B. Pethica, D. Tabor: Wear 100, 7 (1984)
18.48 D. Maugis, H.M. Pollock: Acta Metall. 32, 1323 (1984)
18.49 P.J. Blau, B.R. Lawn (Eds.): *Microindentation Techniques in Materials Science and Engineering* (ASTM, Ann Arbor 1986)
18.50 C.C. Chen, A.A. Hendrickson: J. Appl. Phys. 42, 2208 (1971)
18.51 J.B. Pethica, R. Hutchings, W.C. Oliver: Philos. Mag. A48, 593 (1983)
18.52 J.B. Pethica: *Ion Implantation into Metals*, ed. by V. Ashworth et al. (Pergamon Press, Oxford 1982) p. 147
18.53 J.B. Pethica, W.C. Oliver: Physica Scripta T19, 61 (1987)
18.54 K. Kendall, D. Tabor: Proc. R. Soc. A323, 321 (1971)
18.55 E.W. Müller, T.T. Tsong: *Field Ion Microscopy* (Elsevier, New York 1969)
18.56 E.W. Müller: Z. Physik 131, 136 (1951)
18.57 R.J. Walko: Surface Sci. 70, 302 (1978)
18.58 D.H. Buckley: J. Vac. Sci. Technol. 13, 88 (1976); Wear 46, 19 (1978)
18.59 S.V. Pepper: J. Appl. Phys. 50, 8062 (1979); ibid. 47, 801 (1976); ibid. 45, 2947 (1974)
18.60 S.V. Pepper: J. Vac. Sci. Technol. 20, 643 (1982)
18.61 B.M. DeKoven, P.L. Hagans: Mat. Res. Soc. Symp. Proc. 140, 357 (1989)
18.62 K.P. Walley, A.J. Gellman: preprint
18.63 K. Miyoshi: Mat. Res. Soc. Symp. Proc. 153, 321 (1989)
18.64 G. Binnig, H. Rohrer, Ch. Gerber, E. Weibel: Phys. Rev. Lett. 50, 120 (1983)
18.65 M.T. Dugger, Y.W. Chung, B. Bhushan, W. Rothschild: J. Tribology, to be published
18.66 J.H. Coombs, J.B. Pethica: IBM J. Res. Develop. 30, 455 (1986)
18.67 J.M. Soler, A.M. Baro, N. Garcia, H. Rohrer: Phys. Rev. Lett. 57, 444 (1986)
18.68 H.J. Mamin, E. Ganz, D.W. Abraham, R.E. Thomson, J. Clarke: Phys. Rev. B 34, 9015 (1986)
18.69 C.M. Mate, R. Erlandsson, G.M. McClelland, S. Chiang: Surface Sci. 208, 473 (1989)
18.70 R.C. Jaklevic, L. Elie: Phys. Rev. Lett. 60, 120 (1988)
18.71 G. Binnig, C.F. Quate, Ch. Gerber: Phys. Rev. Lett. 56, 930 (1986)
18.72 G.M. McClelland, R. Erlandsson, S. Chiang: in *Review of Progress in Quantitative Non-Destructive Evaluation*, ed. by D.O. Thompson, D.E. Chimenti (Plenum, New York 1987) p. 1307; R. Erlandsson, G.M. McClelland, C.M. Mate, S. Chiang: J. Vac. Sci. Technol. A 6, 266 (1988)
18.73 Y. Martin, C.C. Williams, H.K. Wickramasinghe: J. Appl. Phys. 61, 4723 (1987)
18.74 D. Rugar, H.J. Mamin, R. Erlandsson, J.E. Stern, B.D. Terris: Rev. Sci. Instrum. 59, 2337 (1988); D. Rugar, H.J. Mamin, P. Günther: Appl. Phys. Lett. 55, 2588 (1989)
18.75 G. Meyer, N.M. Amer: Appl. Phys. Lett. 53, 1045 (1988); S. Alexander, L. Hellemans, O. Marti, J. Schneir, V. Elings, P.K. Hansma, M. Longmie, J. Gurley: J. Appl. Phys. 65, 164 (1989)
18.76 G. Neubauer, S.R. Cohen, G.M. McClelland: In *Interfaces Between Polymers, Metals, and Ceramics*, ed. by B.M. DeKoven, A.J. Gellman, R. Rosenberg: Mat. Res. Soc. Symp. Proc. 153, 307 (1989)
18.77 T. Göddenhenrich, H. Lemke, U. Hartmann, C. Heiden: to appear in J. Microscopy
18.78 G. Neubauer, S.R. Cohen, G.M. McClelland, D. Horne, C.M. Mate: Rev. Sci. Instrum. (1990), in press
18.79 S. Gould, O. Marti, B. Drake, L. Hellemans, C.E. Bracker, P.K. Hansma, N.L. Keder, M.M. Eddy, G.D. Stucky: Nature 332, 332 (1988); P.K. Hansma, V.B. Elings, O. Marti, C.E. Bracker: Science 242, 209 (1988)
18.80 F.F. Abraham, I.P. Batra: Surface Sci. 209, L125 (1989)
18.81 J.P. Pethica: Phys. Rev. Lett. 57, 3235 (1986)
18.82 T.R. Albrecht: Ph.D. Dissertation, Stanford University (1989)
18.83 E. Meyer, H. Heinzelmann, P. Grütter, Th. Jung, H.-R. Hidber, H. Rudin, H.-J. Güntherodt: Thin Solid Films, 180 (1989), to be published
18.84 C.M. Mate, G.M. McClelland, R. Erlandsson, S. Chiang: Phys. Rev. Lett. 59, 1942 (1987)
18.85 R. Erlandsson, G. Hadziioannou, C.M. Mate, G.M. McClelland, S. Chiang: J. Chem. Phys. 89, 5190 (1988)
18.86 N.A. Burnham, R.J. Colton: J. Vac. Sci. Technol. A 7, 2906 (1989)
18.87 N.A. Burnham, D.D. Dominguez, R.L. Mowery, R.J. Colton: Phys. Rev. Lett. 64, 931 (1990)

18.88 G.S. Blackman, C.M. Mate, M.R. Philpott, to be published
18.89 I. Langmuir: Trans Faraday Soc. XV, pt. 3, 62 (1920)
18.90 I. Langmuir: J. Franklin Inst. 218, 143 (1934)
18.91 V. Novotny, J.D. Swalen, J.P. Rabe: Langmuir 5, 485 (1989)
18.92 V. DePalma, N. Tillman: Langmuir 5, 868 (1989)
18.93 O. Levine, W.A. Zisman: J. Chem. Phys. 61, 1068 (1957)
18.94 S.R. Cohen, G. Neubauer, G.M. McClelland: to appear in J. Vac. Sci. Technol. A (July/August, 1990)
18.95 R. Kaneko, K. Nonaka, K. Yasuda: J. Vac. Sci. Technol. A 6, 291 (1988); R. Kaneko: J. Microscopy 152, 363 (1988)
18.96 C.M. Mate, M.R. Lorenz, V.J. Novotny: J. Chem. Phys. 90, 7550 (1989)
18.97 C.M. Mate, M.R. Lorenz, V.J. Novotny: IEEE Trans. on Magnetics 1990 (in press)
18.98 B.D. Terris, J.E. Stern, D. Rugar, H.J. Mamin: Phys. Rev. Lett. 63, 2669 (1989); J. Vac. Sci. Techn. A, in press
18.99 J.E. Stern, B.D. Terris, H.J. Mamin, D. Rugar: Appl. Phys. Lett. 53, 2717 (1988)
18.100 G.M. McClelland: In *Adhesion and Friction*, ed. by M. Grunze, H.J. Kreuzer, Springer Series in Surface Science, Vol. 17 (Springer, Berlin, Heidelberg 1989), p. 1
18.101 G.A. Tomlinson: Philos. Mag. Series 7 7, 905 (1929)
18.102 J.B. Sokoloff: Surf. Sci. 144, 267 (1984)
18.103 M.W. Ribarsky, U. Landman: Phys. Rev. B 38, 9522 (1988)
18.104 U. Landman, W.D. Luedtke, M.W. Ribarsky: J. Vac. Sci. Technol. A 7, 2829 (1989)
18.105 U. Landman, W.D. Luedtke, M.W. Ribarsky: Mat. Res. Soc. Symp. Proc. 140, 101 (1989)
18.106 U. Landman, W.D. Luedtke, A. Nitzan: Surface Sci. 210, L177 (1989)
18.107 U. Landman, W.D. Luedtke, R.N. Barnett: In *Many-Atom Interactions in Solids*, ed. by R. Nieminien (Springer, Berlin, Heidelberg 1989)
18.108 F.F. Abraham, I.P. Batra, S. Ciraci: Phys. Rev. Lett. 60, 1314 (1988)
18.109 S.A.C. Gould, K. Burke, P.K. Hansma: Phys. Rev. B 40, 5363 (1989)
18.110 D Tománek, G. Overney, H. Miyazaki, S.D. Mahanti, H.J. Güntherodt: Phys. Rev. Lett. 63, 876 (1989)
18.111 S. Ciraci, A. Baratoff, I.P. Batra: to be published
18.112 I.P. Batra, S. Ciraci: J. Vac. Sci. Technol. A 6, 313 (1988)
18.113 J.B. Pethica, A.P. Sutton: J. Vac. Sci. Technol. 6, 2494 (1988)
18.114 J.R. Smith, G. Bozzolo, A. Bannerjea, J. Ferrante: Phys. Rev. Lett. 63, 1269 (1989)
18.115 A. Bannerjea, J.R. Smith, J. Ferrante: Mat. Res. Soc. Symp. Proc. 140, 89 (1989)
18.116 M. Schoen, C.L. Rhykerd, Jr., D.J. Diestler, J.H. Cushman: Science 245, 1223 (1989)
18.117 I. Bitsanis, J.J. Magda, M. Tirrell, H.T. Davis: J. Chem. Phys. 87, 1733 (1987)
18.118 H.-W. Fink: IBM J. Res. Develop. 30, 460 (1986); Y. Kuk, P.J. Silverman: Appl. Phys. Lett. 48, 1597 (1986); Y. Kuk, P.J. Silverman: Rev. Sci. Instrum. 60, 165 (1989)
18.119 R.G. Horn, D.R. Clarke, M.T. Clarkson: J. Mater. Res. 3, 413 (1988)
18.120 R.G. Horn, D.T. Smith, W. Haller: Chem. Phys. Lett. 162, 404 (1989)
18.121 A. Majumdar, B. Bhushan: J. Trib., Trans. ASME (in press)

Reprinted from

REVIEW OF SCIENTIFIC INSTRUMENTS

a publication of the American Institute of Physics

Vol. 61, No. 9, September 1990

Force microscopy with a bidirectional capacitance sensor

Gabi Neubauer, Sidney R. Cohen, Gary M. McClelland, Don Horne, and C. Mathew Mate

IBM Research Division, Almaden Research Center, 650 Harry Rd., San Jose, California 95120-6099

pp. 2296-2308

Force microscopy with a bidirectional capacitance sensor

Gabi Neubauer,[a] Sidney R. Cohen,[b] Gary M. McClelland,[c] Don Horne, and C. Mathew Mate[d]
IBM Research Division, Almaden Research Center, 650 Harry Rd., San Jose, California 95120-6099

(Received 5 March 1990; accepted for publication 10 April 1990)

A new method for sensing cantilever deflection in the atomic force microscope (AFM), based on capacitance measurement, is described. Parameters governing the design of such an instrument are considered in detail. Two different geometries are compared, wire on plate and an integrated flat plate sensor. The electronic circuitry, providing 6×10^{-19} F noise in a 0.01–1000 Hz bandwidth, is also described. Implementation of the design ideas into a working AFM in ultrahigh vacuum is demonstrated. This AFM allows simultaneous measurement of cantilever deflection in two orthogonal directions, necessary for our nanotribology studies. The theoretical sensitivity of 5×10^{-7} F/m is not achieved due to roughness. The bidirectional sensing and imaging capabilities are demonstrated for an Ir tip on cleaved graphite, and a diamond tip on diamond films. The capacitance detection technique is compared and contrasted with other AFM sensors.

I. INTRODUCTION

Since its introduction in 1986,[1] the atomic force microscope (AFM) has proven to be an invaluable tool in obtaining atomic scale, and near-atomic scale topographical images of nonconducting surfaces. In addition, it has been used to measure forces as weak as the van der Waals attraction between a sharp tip and a nearby surface. In the AFM, forces between a tip and a surface are detected by measuring the deflection of a flexible cantilever upon which the tip is mounted. In the first AFM, the cantilever deflection was monitored by tunneling from a second tip; subsequent designs have used optical detection. In this paper, we report the implementation of a new scheme: using capacitance to detect cantilever deflection in an AFM. Our new AFM, incorporating this sensor, was designed for ultrahigh vacuum (UHV) experiments in tribology (the study of friction, lubrication, and wear), at the subnanometer level. In such studies, the imaging capabilities of the AFM are combined with force measurements in the nanonewton range, perpendicular and lateral to the surface. This is the first AFM capable of sensing the two directions of force simultaneously. First results obtained with this instrument have been published elsewhere.[2,3] Göddenhenrich *et al.* have also recently described a capacitance-based AFM.[4]

Whereas our AFM was designed specifically for atomic scale tribology, it has promise for broad applications as a probe for interfacial forces. To be useful for this range of applications, three requirements are of particular importance. First, the AFM should be operated inside an ultrahigh vacuum system, where well-characterized surfaces can be prepared and maintained. Next, it must be capable of measuring frictional force and load simultaneously. And finally, it should be operable at frequencies near zero (i.e., dc mode), while recording the instantaneous cantilever deflections. Many AFMs surmount problems of low-frequency noise by rapidly oscillating the sample or cantilever (i.e., operating the AFM in the ac mode) and using phase-sensitive detection. For force measurements that are made during hard contact between tip and surface, such oscillations are not allowed as they may perturb the mechanics of the system under study.

Keeping these requirements in mind, we will, in Sec. II, examine the applicability of different existing AFM cantilever sensor techniques, and summarize the role of capacitance in scanning microscopies. Section III presents in detail our new detection method and considers various possible detector designs. The electronic circuitry will then be introduced, paying particular attention to the low frequency noise behavior. Section IV briefly describes the incorporation of the instrument into a UHV chamber with other surface probes. In Sec. V the instrumental performance will be evaluated using data obtained for iridium tips and diamond tips sliding on highly oriented pyrolytic graphite and diamond films, respectively. Section VI proposes refinements and extensions to the capacitance technique.

II. AFM CANTILEVER SENSOR TECHNIQUES

The first AFM employed tunneling from an additional tip to the back side of the lever for detecting the cantilever deflection.[1] The high sensitivity resulting from the exponential distance dependence of the tunneling current led to a wide application of this technique, mostly in imaging studies.[1,5,6] However, because of its low dynamic range, the tunneling technique requires the use of feedback circuits to follow large cantilever deflections and thermal drifts, thereby limiting the available bandwidth. As the major disadvantage, the tunneling detection method suffers from contamination-induced instabilities of the tunneling junction, which can make its performance very unreliable, even under vacuum conditions. Finally, the tunneling tip exerts extraneous

[a] Current address: Lawrence Berkeley Laboratory, Center for Advanced Materials, Mailstop 66/200, 1 Cyclotron Rd., Berkeley, CA 94720.
[b] Chaim Weizmann Postdoctoral Fellow.
[c] Author to whom correspondence should be addressed.
[d] Also affiliated with the IBM Magnetic Recording Institute.

 0034-6748/90/092296-13$02.00 © 1990 American Institute of Physics

forces on the cantilever, both van der Waals and electrostatic in nature, which can significantly distort the actual force measurements. A bidirectional sensor based on the tunneling technique has been operated in our laboratory[7] by monitoring the tunneling current from the cutting edges of two orthogonal razor blades to the back side of a lever.[8] However, the low reliability of the tunneling technique, now compounded by the simultaneous operation of two independent tunneling junctions, was unsatisfactory.

The need for a more reliable detection method led to the introduction of a variety of optical techniques, which have a much greater dynamic range and exert no extraneous force on the cantilever. In homodyne optical interferometry, initially demonstrated in our laboratory, a HeNe laser beam is reflected off a cantilever and interferes with a part of the beam reflected from a reference flat.[9-11] Despite its simplicity and higher reliability as compared to the tunneling method, this homodyne interferometer suffers from its high noise level at frequencies below 100 Hz. For example, in a 0.5 Hz to 3 kHz bandwidth a cantilever displacement noise level of 0.2-Å RMS was found.

By introducing optical fibers into the homodyne setup, the air path length of the interferometer was lowered to that of the fiber-level spacing, $\simeq 10\ \mu$m, thus reducing the low frequency noise.[12-14] A major improvement of the homodyne techniques was recently achieved through an all-fiber configuration containing a multimode GaAlAs diode laser with a direct single-mode fiber output and a single-mode directional coupler.[13] In addition to the advantages of very compact, UHV adaptable instrumentation and reduced heat dissipation, optical path length fluctuations due to air turbulences are almost completely avoided, the only remaining spacing being the one between fiber and cantilever. Because of the short coherence length of the diode laser, the low-frequency stability is further improved, since interference effects due to stray reflections are eliminated. Thus, in a dc to 1-kHz bandwidth, the peak-to-peak noise is less than 0.1 Å. Above 1 kHz a noise spectral density of 5.5×10^{-4} Å/$\sqrt{\text{Hz}}$ is reported, close to the shot noise limit. A fiber design using a HeNe laser and a single mode directional coupler has also been reported.[15]

In the heterodyne technique[16] a frequency-shifted part of a HeNe laser, formed by a radio frequency (rf) Bragg-cell modulator, interferes with the phase-shifted part reflected off the cantilever. This technique requires extensive rf electronics as compared to the homodyne setup, but it is inherently insensitive to laser intensity fluctuations. This method has only been implemented in the ac mode, where the interferometer noise at the lever resonant frequency was much less than the thermal noise of the lever, which amounted to 0.01 Å/$\sqrt{\text{Hz}}$.

Another interferometric scheme, very well suited for both ac and dc measurements, was reported recently.[17] From a HeNe laser two orthogonally polarized light beams—a reference and a sensing beam—are formed, which are reflected off the base and end of the cantilever, respectively. The relative phase of the two beams is a measure of the cantilever deflection. This method greatly reduces sensitivity to optical path length or laser intensity fluctuations. The total RMS noise was measured to be 0.01 Å in a bandwidth of 1 Hz to 20 kHz.

In a recently reported GaAlAs diode laser feedback system,[18] the amplitude of cantilever vibrations is detected by an integrated photodiode, which measures intracavity intensity changes due to interaction of the reflected part of the laser light with the gain medium. At the lever resonance frequency, a sensitivity of 0.03 Å/$\sqrt{\text{Hz}}$ was reported.[19]

Finally, an optical method using deflection rather than interferometry is being used in several laboratories.[20,21] Here, the deflection of a laser beam off a small mirror mounted on the cantilever is detected with a dual-photodiode position-sensitive detector. This approach was also demonstrated in vacuum,[20] with the HeNe laser and the detector located outside the UHV chamber, and a smallest detectable cantilever displacement of 4×10^{-4} Å/$\sqrt{\text{Hz}}$ due to shot noise was calculated by the authors. Deflections of the laser beam due to air path fluctuations were clearly recognized as the major source of noise in the setup in air.[21] This problem can very likely be avoided by placing diode and detector in vacuum, or by running fibers to these elements, placed outside the vacuum.

Although the use of capacitance variation to measure lever deflection in a force microscope is new, the idea of using capacitance to measure displacement is well known,[22] and general purpose sensors are commercially available. Microscopes which *directly* sense the capacitance variation between a sharp tip and a surface have been described,[23-26] and this principal is the basis of a video disk player.[27]

Scanning microscopy has also been demonstrated where the electrostatic force that exists between the two electrodes of a capacitor, here a sharp tip and a conducting surface, is the output of the feedback loop. This technique is independent of the means of detecting lever deflection. This principal has been used to profile conducting surfaces with and without dielectric overlayers,[11,28] and to detect minute static charges.[29]

The new cantilever-sensing technique, which will be described in the next section, uses a compact, vacuum-compatible sensor, which measures forces in both directions through changes in capacitance and, in addition, enables changing of cantilevers *in situ*. This is the first AFM capable of measuring two directions of force simultaneously. Bidirectional optical sensors are possible, but have not yet been demonstrated. This method provides high sensitivity and a high dynamic range while maintaining low noise levels in the dc mode; e.g. 0.03-Å RMS in a 0.1 Hz-to-1 kHz bandwidth.

Recent publications by ourselves[2,3] and another group[4] have demonstrated the use of a capacitance AFM but have not elaborated on the many important factors involved in the construction and operation of such an instrument, which we present below.

III. THE NEW DETECTION METHOD

A. Experimental design considerations

The specific geometry chosen for the capacitance sensor proves to be an issue of some complexity. The obvious concern of high sensitivity is opposed by the more subtle subject

of snapping. The rate of change in capacitance with distance (sensitivity) increases as the distance between two bodies decreases. However, the attractive electrostatic force between the bodies also becomes large at small distances. The geometry must be chosen to achieve maximum sensitivity without causing snapping together, which occurs when the gradient of the attractive force exceeds the spring constant. This will be discussed below. During typical operation, tips are changed on a frequent basis. The design must be able to accommodate different sizes and shapes of tips and cantilevers, and provide for ease in exchanging them.

Two design geometries were evaluated, and are depicted in Fig. 1. The integrated sensor [Fig. 1(a)] detects capacitance between two flat plates. The bottom plate consists of two electrodes. For example, we tried preliminary studies where the top plate consisted of a doped silicon strip that had been micromachined[30] to a thickness of several microns, and attached to the glass plate using field-assisted bonding.[31] The area of overlap of the two plates and the distance between them determines the capacitance. The sensor is coupled to the force-sensing cantilever. The bidirectional detection capability of this design would operate as follows: an increase in load brings the upper plate closer to both of the bottom electrodes and thus increases the capacitance. Friction results in a twisting of the upper plate, which would bring it closer to one of the bottom electrodes and further from the other. An increase would be seen in the *difference* signal from the two bottom electrodes. The parallelism and flatness of the two plates is crucial to this technique. This is to prevent shorting out for the small separations used.

The capacitance between the plates is

$$C = \epsilon A/d. \tag{1}$$

Here A is the plate area, d the distance between plates, and ϵ the permittivity in vacuum, 8.85×10^{-12} F/m. Ultimately, the sensitivity is governed by the capacitance derivative

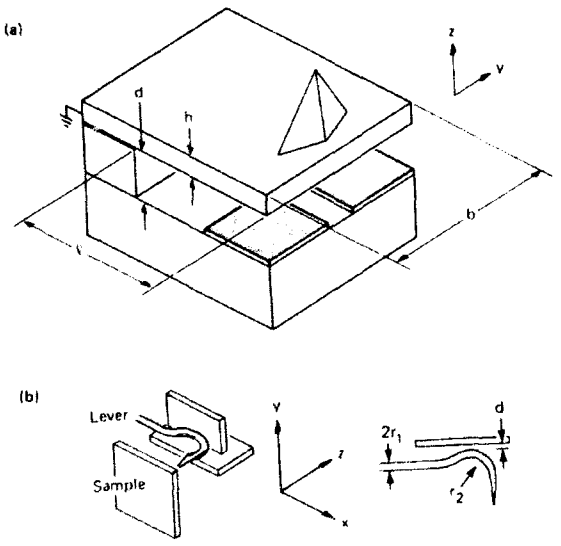

FIG. 1. Schematic views of the two sensor configurations: (a) integrated sensor with tip; (b) wire on plate with sharpened end pointing toward the sample. Parameters indicated are those referred to in the text.

$$\frac{dC}{dd} = -\frac{\epsilon A}{d^2}. \tag{2}$$

The spring constant k and resonance frequency f_R of a rectangular bar fixed at one end (i.e., the top plate) are[32]

$$k = (Ebh^3/4l^3), \tag{3a}$$

$$f_R = (1.02/\pi)(k/blh\rho)^{1/2}, \tag{3b}$$

where E is the Young's modulus of the material, b, h, and l are the width, thickness, and length of the bar, respectively, and ρ is the material density. The electrostatic force attracting the plates is the partial derivative with respect to d of the electrostatic energy $W_{el} = (Q^2/2C)$ in a capacitor holding charge $Q = VC$:

$$F_{el} = -\left.\frac{\partial W_{el}}{\partial d}\right|_Q = -\left(\frac{Q^2}{2}\right)\frac{\partial(1/C)}{\partial d}$$

$$= C^2\frac{V^2}{2}\frac{A}{\epsilon} = -\frac{\epsilon}{2}\frac{AV^2}{d^2}. \tag{4}$$

From (4) we obtain the force derivative:

$$F'_{el} = A\epsilon V^2/d^3. \tag{5}$$

Here $A \simeq bl/3$ because the sensor is only free to bend on one end, and hence only part of the area contributes to changes in capacitance. In order to have similar sensitivities in the two dimensions, the width and length of the upper plate must be approximately equal so that $A = l^2/3 = b^2/3$. The exact dimensions of the device are dependent on the desired characteristics. Spring constant and resonance frequency must have values that satisfy the instrumental operating conditions. From Eqs. 3(a) and 3(b) it is derived that

$$l = \left(\frac{E^{1/8}}{1.17\pi^{3/4}\rho^{3/8}}\right)\frac{k^{1/4}}{f_R^{3/4}}, \tag{6a}$$

$$h = \left(\frac{1}{0.70\pi^{1/2}E^{1/4}\rho^{1/4}}\right)\left(\frac{k}{f_R}\right)^{1/2}. \tag{6b}$$

The maximum allowed voltage is then set by the snapping criterion, which requires k to be greater than the force derivative. In practice, this means that F'_{el} is some fraction α of the cantilever force constant. From (5) and (3a),

$$\frac{h^3d^3}{V^2A^2} = \frac{12\epsilon}{E\alpha}. \tag{7}$$

Substituting from (6b) gives

$$V^2A^2 = \frac{\alpha d^3E^{1/4}}{4.0\pi^{3/2}\epsilon\rho^{3/4}}\left(\frac{k}{f_R}\right)^{3/2}. \tag{8}$$

Since the detector noise is generally independent of the rf voltage applied, but the detectable current through the capacitor increases linearly with V, a corollary to (2) is that the signal-to-noise ratio varies as:

$$S/N \propto V\frac{dC}{dd} = \epsilon A\frac{V}{d^2}. \tag{2a}$$

S/N can be improved by increasing V, increasing A, or decreasing d. The limitations on this "tuning" process are defined by the equations above. A lower limit for d will most likely be defined by the precision of the micromachining process. This means that the only way to improve S/N is to increase V or A. Equation (7) shows that this can only be

done in conjunction with increasing h, which will adversely affect k and f_R. These tradeoffs can be incorporated into the sensitivity equation by substituting VA from Eq. (8) into (2a):

$$\left(\frac{S}{N}\right)_D \propto \left(\frac{\epsilon^{1/2}\alpha^{1/2}E^{1/8}}{4.78\rho^{3/8}}\right)\frac{k^{3/4}}{f_R^{3/4}d^{1/2}}. \tag{9}$$

This is the S/N for displacement measurement. For most purposes a more important figure is the S/N for force:

$$\left(\frac{S}{N}\right)_F = \frac{(S/N)_D}{k} \propto \left(\frac{\epsilon^{1/2}\alpha^{1/2}E^{1/8}}{4.78\rho^{3/8}}\right)\frac{1}{k^{1/4}f_R^{3/4}d^{1/2}}. \tag{10}$$

The significance of these two equations deserves emphasis. For a given material and length-to-width ratio, there are four adjustable parameters: l, h, d, and V. By requiring a certain cantilever force constant and resonant frequency and using a voltage limited by snapping, three of these variables have been eliminated. For example, choosing a desired k of 50 N/m and f_R of 5 kHz, we find that $l = b = 2.3$ mm, and $h = 19$ μm, using $E = 1.7\times10^{11}$ Pa and $\rho = 2300$ kg/m^3, values for Si. By setting the plate separation d to a realistic minimum of 2 μm, we obtain a capacitance derivative (sensitivity) of $\simeq 3.9\times10^{-6}$ F/m. From Eq. (8), the working voltage is then 6.4 V RMS.

The second configuration [Fig. 1(b)], which we have implemented, is that of a curved wire near two orthogonal plates. The capacitance is then measured between the wire and each of the two plates. This device is somewhat simpler than the first as the curved wire is itself the cantilever, so no mechanical connection need exist between the cantilever/tip and any part of the sensor providing greater ease in interchanging tips. In addition, no microfabrication is required. The disadvantages are that the cantilever must be conducting and have the geometry of a curved wire. The wire is curved in order to ease its alignment with respect to the plates.

Analogous to the flat plate geometry, a series of equations describes the choice of parameters. First we obtain the capacitance derivative by approximating the wire-plate geometry by that of an ellipsoid separated from the plate by a distance much smaller than either of its principle radii:

$$\frac{dC}{dd} = 5.56\times10^{-11}\frac{\sqrt{r_1 r_2}}{d}. \tag{11}$$

Here, r_1 is the wire radius and r_2 is the radius of curvature. The spring constant and resonance frequency of the cantilever are given by[32]

$$k = 3\pi r_1^4 E/4l^3, \tag{12a}$$

$$f_R = 0.284(r_1^2 E/\rho l^4)^{1/2}, \tag{12b}$$

and the force derivative is

$$F' = 2.78\times10^{-11}(V^2/d^2)\sqrt{r_1 r_2}. \tag{13}$$

As for the parallel plate geometry, the sensitivity increases with decreasing d, but in practice the operating distance d_{op} should be set so that F' is a fraction α of k, giving

$$d_{op} = \sqrt{2.78\times10^{-11}V^2(\sqrt{r_1 r_2}/k\alpha)}. \tag{14}$$

Combining Eqs. (11) and (14), we find that at this distance

$$\frac{dC}{dd} = \frac{1.05\times10^{-5}(r_1 r_2)^{1/4}(k\alpha)^{1/2}}{V}, \tag{15}$$

where $k\alpha = F'$. Remembering from above that the S/N is proportional to $V(dC/dd)$, we see that the S/N is independent of varying V and d, as long as these parameters are varied proportionately according to Eq. (13) to maintain a particular F'.

Specifying k and f_R, as was done for the first configuration, fixes two parameters, in this case the wire radius and length:

$$l = \left(\frac{E^{1/5}}{3.22\rho^{2/5}}\right)\frac{k^{1/5}}{f_R^{4/5}}, \tag{16}$$

$$r_1 = \left(\frac{1}{2.98\rho^{3/10}E^{1/10}}\right)\frac{k^{2/5}}{f_R^{1/5}}. \tag{17}$$

The snapping condition gives

$$\frac{d}{V} = \left(\frac{3.71\times10^{-11}}{\pi E\alpha}\right)^{1/2}\left(\frac{r_2^{1/4}l^{1/2}}{r_1^{7/4}}\right). \tag{18}$$

For the Ir wire we commonly use, $E = 5.2\times10^{11}$ Pa and $\rho = 2.25\times10^4$ kg/m^3. We find for a desired k of 50 N/m and f_R of 5 kHz that $r_1 = 33$ μm and $l = 3.0$ mm. Since the curvature r_2 is necessary only for alignment of the wire with the plates, it must be of the order of the plate dimension. We choose 2 mm, which for $V = 3.5$ V RMS and $\alpha = 0.5$ gives a working distance of 590 Å, corresponding to a sensitivity of 2.4×10^{-7} F/m. Clearly, there are a number of considerations that will determine the final choice of parameters. For instance, there is a minimum wire diameter that can be easily handled. A final consideration not discussed above is the dynamic range: in order to relieve the constraints of operation with feedback control on the sensor plates, d must be large enough to prevent snapping of the wire into the sensor plate as the cantilever is pushed back. If d is made too large, however, the sensitivity is unacceptably low.

Due to handling constraints in the current mode of operation, our typical wire is 125 μm in diameter and 6 mm long, giving $k = 90$ N/m and $f_R = 2.5$ kHz. With $r_2 = 2$ mm, $F' = 50$ N/m, and $V = 3.5$ V RMS, the operating distance is 490 Å [Eq. (14)], giving a sensitivity of 4.0×10^{-7} F/m.

B. Electronic circuitry

The above calculations for the model sensor geometries indicate that capacitance noise levels on the order of 10^{-18} F are required to achieve deflection sensitivities of 0.1 Å. These levels are small not only on an absolute scale, but also compared to the total input capacitance of several pF for typical circuits. The basis for the capacitance measurement, applying an oscillating voltage across the capacitor and measuring the reactive current, is well known. Very precise measurements are possible in principle, since a capacitor has no Johnson noise (associated with resistors) or shot noise (associated with semiconductor junctions). The sensitivity of the capacitance circuit is optimized by measuring the capacitance at a high frequency to maximize the sensor current and by using a balanced configuration to null out the effect of amplitude variations in the alternating voltage.

As illustrated in Fig. 2, the instrument uses a grounded cantilever, and the circuit measures at 6.4 MHz the capacitance C_s of the sensor plate with respect to ground. The transformer input configuration (using a Mini Circuits T1-1 transformer) has three advantages. It allows one terminal of the sensor capacitance to be at ground, keeps the sensitivity of the circuit independent of the total input capacitance, and affords a simple means for balancing the circuit through the trimmer capacitor or the varactor. Negative feedback keeps the base of the MPSH07 near rf ground, so that the sensor current flows through the feedback capacitor C_F, giving an rf signal at the collector of $(C_b - C_s)V_{rf}/C_F$, where V_{rf} is the rf supply voltage and C_b is the balancing capacitance. After the emitter follower 2N3904, the signal is demodulated at approximately unity gain by a mixer (Mini-Circuits TFM-3). It is then filtered before being amplified by 100, giving an overall circuit gain of $dV_{out}/dC_s = 100V_{rf}/C_F$. With a different output amplifier and filtering, this circuit could be operated at a bandwidth up to 1 MHz. Using an rf voltage V_{rf} of 3.5 V RMS, and a C_F of about 2 pF, we measure a gain of 1.2×10^{14} V/F, in good agreement with this equation.

The $\pm$ 10-V output swing gives a range of 0.16 pF. Precise balancing is therefore essential just to bring the output on scale, and is also important to minimize the effect of V_{rf} amplitude noise on the output. The balancing is provided by the varactor. Because the varactor performance conforms closely to published specifications, it also provides a simple means to calibrate and check the performance of the circuit, since the circuit responds in the same way to variations of the sensor capacitance as it does to variations of the varactor capacitance (after the two 20-pF series capacitors are taken into account). When larger series capacitors were used to provide a large balancing range, the varactors apparently made some contribution to the $1/f$ noise described below. As presently configured, when the varactor bias is varied between 8 and 27 V, the varactor capacitance changes from 6 to 2.5 pF, corresponding to a circuit offset range of 1.75 pF.

Figure 3 presents a schematic of the rf source used. This circuit generates a sine wave of very well-regulated frequency and amplitude, and we have no evidence that it contributed to the noise of our instrument.

The two principal sources of white noise in this circuit are the voltage and current noise of the MPSH07. With a dc base current $i_B =$ of 2.6 μA, the shot noise current is $\sqrt{2qi_B} = 0.9$ pA/$\sqrt{\text{Hz}}$, where q is the electronic charge. (In this paper all spectral densities are root mean square signal per unit bandwidth.) This noise current passes through C_f, and is demodulated around the rf frequency giving a noise voltage of 770 nV/$\sqrt{\text{Hz}}$ at the circuit output. The MPSH07 voltage noise is specified to be 1.7 nV/$\sqrt{\text{Hz}}$. With a total base capacitance C_B (including the sensor and stray capacitance of the lead in wires) of 5 pF, the resulting noise at the collector is $1.7\times(C_B + C_f)/C_F = 6$ nV/$\sqrt{\text{Hz}}$, giving 600 nV/$\sqrt{\text{Hz}}$ at the circuit output.

The net noise is thus calculated to be $\sqrt{0.6^2 + 0.77^2} = 1$ μV/$\sqrt{\text{Hz}}$. We measure 1.7 μV/$\sqrt{\text{Hz}}$, at frequencies $\gtrsim$500 Hz, in reasonable agreement. As expected the measured white noise spectral density is independent of V_{rf}.

Since the mixer demodulates in only a narrow bandwidth around 6.4 MHz, we would expect any current or voltage noise originating before the mixer to appear at the circuit output with a frequency-independent noise spectrum.

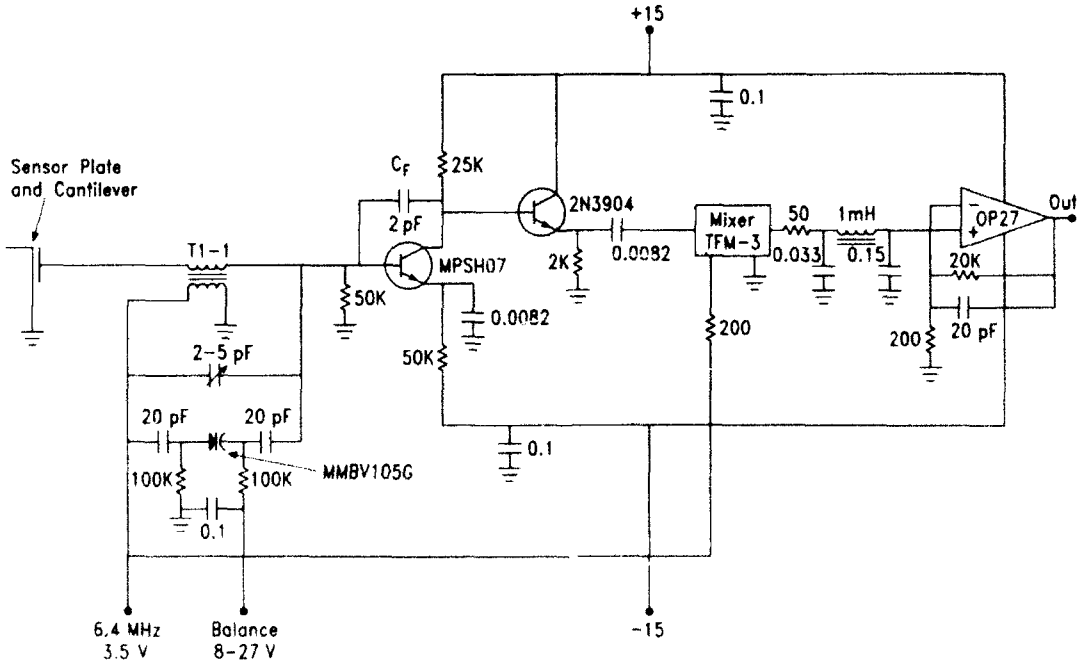

FIG. 2. Schematic diagram of the circuit used to detect capacitance changes between the sensor plate and cantilever. Unless indicated otherwise, capacitance is expressed in μF, resistance in Ω.

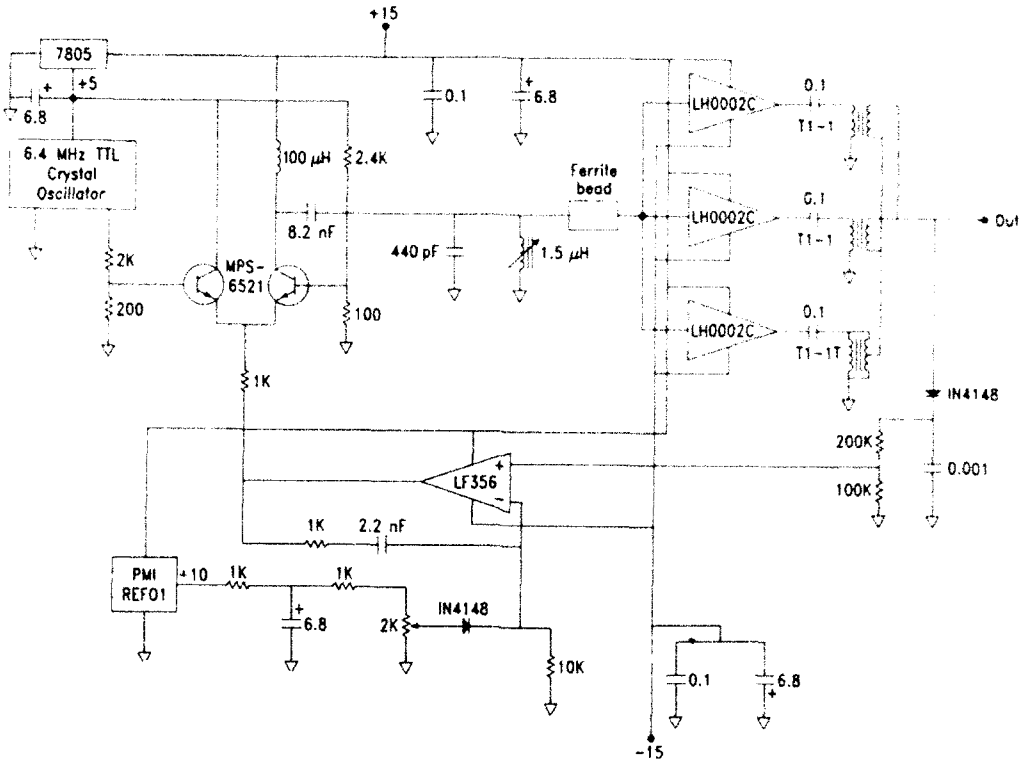

FIG. 3. Schematic diagram of the radio frequency generator used for capacitance measurement. Unless indicated otherwise, capacitance is expressed in μF, resistance in Ω.

From Fig. 4, we see that this is the case above 500 Hz, but that below this frequency the noise rises steadily. This additional noise component is unchanged by offsetting the circuit with the varactor, but it is proportional to V_{rf}. For this reason we believe that the noise arises from fluctuations of the reactance of the portion of the circuit before the MPSH07. The noise could be altered substantially by soldering and unsoldering trimmer capacitors, but never in a reproducible way.

The observed noise spectrum can be fit by the equation

$$N_f = \sqrt{1.70^2 + (13/\sqrt{f})^2} \quad \mu V/\sqrt{Hz}, \tag{19}$$

indicating that the noise consists of a constant component plus a component with a $1/f$ power spectrum. Although this last component is very dominant at low frequencies it only contributes 20 μV of noise per decade of frequency. Integrating the above equation,

$$N_T = \sqrt{\int N_f^2 \, df}, \tag{20}$$

we find the total noise N_T over a 1 to 1000 Hz bandwidth to be 63 μV. If the $1/f$ component were to be removed, this figure would drop only slightly, to 53 μV. Over a range of 0.01–1000 Hz, the total noise is 68 μV, or 5.7×10^{-19} F. At a sensitivity of 2×10^{-7} F/m, this is equivalent to a displacement noise of 0.028-Å RMS.

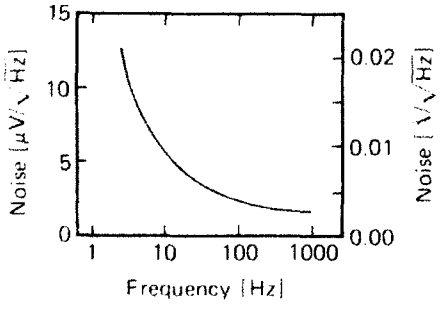

FIG. 4. Measured root mean square noise spectral density vs frequency for the capacitance circuit. The left vertical axis represents circuit output voltage, while the right axis represents the corresponding lever displacement, assuming a sensitivity of 2×10^{-7} F/m.

The actual traces of the output voltage shown in Fig. 5 are consistent with these noise figures. The typical drift rate is less than 0.5 μV/s, corresponding to less than 0.01 Å/min. Since this is better than the positioning drift rate due to thermal variations and piezo creep achieved in most AFMs, the actual drift in the sensor displacement measurement is not limited by the capacitance measurement.

Although the capacitance circuit is mounted in a tube several centimeters from the AFM inside vacuum, the 6.4 MHz rf source is located outside the vacuum; its signal is brought into the vacuum and passes down to the capacitance detector circuit through a coaxial connector. Probably because the circuit works near nulling, the capacitance signal is fairly insensitive to bending or vibration of the rf cable. The $\pm$ 15-V supply is also located outside of vacuum.

The two capacitance signals together with a reference ground were brought to two Tektronix AM 502 differential amplifiers operated at a gain of 100. Because the circuit out-

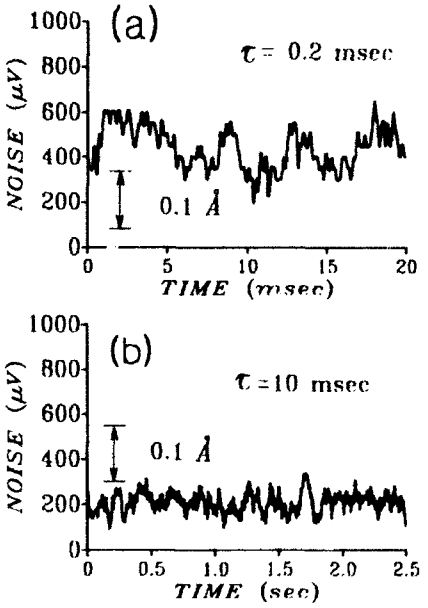

FIG. 5. Noise traces recorded from the capacitance circuit, with two different time constants. The 0.1-Å calibration bar assumes a sensitivity of 2×10^{-7} F/m: (a) Using a 0.2-ms time constant low-pass filter, corresponding to a bandwidth of 1 kHz; (b) 10-ms filter, bandwidth 20 Hz.

put is very sensitive to the line frequency induced and other variations of the varactor voltages, these voltages were provided by three 9-V batteries in series divided by a potentiometer.

Aside from the fundamental limitations of the circuit discussed above in some detail, a chief source of noise is the variation of stray capacitance of the circuit or sensor plates. Because of the extreme sensitivity of the circuit, changes of the capacitance to ground of even the output or supply wires of the circuit due to swinging of the instrument in its suspension can generate noise. To circumvent this problem, all wires running through vacuum to the instrument run through shielded cables (shield grounded) over most of their length. The vibration problem is most severe for wires going directly to the sensor. For this reason, these wires are kept as short and as rigid as possible.

A particularly persistent interfering noise was at 120 Hz and synchronized with the power line. This signal was largest only when the piezo supplies were turned on, but because it was proportional to the rf voltage, it seemed to represent a true capacitance signal on the order of 10^{-17} F *p-p*. It was concluded that the signal resulted largely from the $\simeq$0.1-pF stray capacitance of the sensor plates to the piezoelectric tubes. The 120-Hz signal could result if the impedance at 6.4 MHz of the piezo driving circuits to ground was modulated at 120 Hz. This could result from the switching on and off of the rectifier diodes in the piezo power supply. A similar effect seemed to arise from the $\pm$ 15-V supply of the capacitance circuit itself. In agreement with this theory, we found that the 120-Hz interference disappeared when 1.2-mH inductors were inserted (outside of vacuum) in nearly all wires going to the AFM, including the piezo and capacitance circuit wires, but excluding the rf supply.

When we first implemented our capacitance detection scheme, an anomalous signal was noticed with conducting samples. When the tip came into hard contact with the sample, both the load and friction signals showed an abrupt 1–1.15×10^{-16} F increase in capacitance. This effect is due to the stray capacitance of the sample to the sensor plate, which acts in series with the admittance (impedance $^{-1}$) of the sample to ground to generate a stray sensor-ground capacitance. Although the *derivative* of this capacitance with respect to the sample position is much smaller than the derivative of the cantilever-sensor capacitance with respect to the cantilever position, the *total* sample-sensor capacitance is of the same order as the total cantilever-sensor capacitance. The anomalous signal arises because touching the grounded cantilever to the sample increases the capacitance of the sensor plate to ground.

Obviously this problem could be eliminated by permanently grounding the sample, so that tip contact would have no effect, but this solution would not allow tunneling microscopy, which requires that the sample be electrically biased with respect to the tip. The solution is to use a resonant circuit to permanently ground the sample only at the 6.4-MHz operating frequency of the capacitance circuit. A 200-pF capacitor in series with a custom-wound 3-μH inductor were housed in 18-mm-diam stainless steel can sealed by a welded two-conductor feedthrough. Before sealing, the inductor winding was adjusted to tune the circuit resonance to the 6.4 MHz, so that a low 2-Ω impedance was achieved at this frequency. After the filter was mounted on the AFM base plate, and attached between the sample holder and the AFM body (ground), the anomalous signal was eliminated.

IV. EXPERIMENT

A primary design goal was good vibration isolation, which was attained by mounting the AFM on a suspension of very low resonance frequency and by raising the lowest resonance frequency of the AFM through the use of small, stiff, lightweight parts. Further matters of concern were reduction of stray capacitance and accessibility to all of the devices mounted on the UHV chamber (airlock, LEED, Auger, heater, evaporation source).

Figures 6 and 7 diagram the AFM and the UHV chamber, respectively. The AFM sits on a base plate, which is suspended by two stages of spring support (450 mm total length when fully extended) to the top flange of a 150-mm-diam tube extending upwards from the chamber center. The spring system, with an intermediate mass of about 1 kg between the first and second stages, has a lowest vertical resonance frequency of 1–2 Hz. The sample and sensor are mounted opposite one another on piezoelectric tripods. The tripod consists of three piezoelectric tubes (PZT5A, 25 mm long, 3 mm diameter) each having a scanning range of $\sim$4 μm. For coarse *xyz* translation, each tripod unit is adjusted by three mechanical screws that are accessed by a rotatable wobblestick. A translation of 1 μm results from a 1° screw rotation in the *x* and *y* directions, and spur gears provide a further factor of 7 reduction in the *z* directions. In normal operation, the cantilever remains fixed and the sensor plates and sample are moved toward it first with coarse mechani-

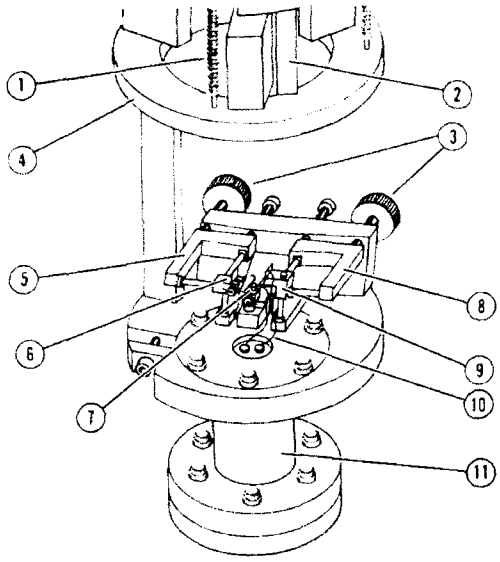

FIG. 6. Schematic of AFM, showing (1) spring suspension, (4) mounting ring, (2) eddy current damping, (3) mechanical adjust screws for sample and sensor, (5) piezo tripods for sample and (8) sensor, (6) sample mount, (7) tip mount on piezo tube scanner, (9) macor mounting block for sensor plates, (10) leads to capacitance circuit, and (11) sealed tube containing capacitance circuitry. For clarity, sample and sensor are shown mechanically retracted from the wire.

cal, and then fine piezoelectric adjustments. The cantilever, however, is mounted on a piezoelectric single tube scanner,[33] which may be used to oscillate it in any direction. Both cantilever and sample are attached to small mounts with wire hooks so that a wobblestick can carry them to all devices—airlock with linear translation stage, LEED, Auger, heater, evaporation source—without breaking the vacuum. The bottom of the mount is a post that slides into a socket and is locked into place by a set screw.

Most of the experiments were done using iridium as the cantilever/tip material because of its hardness and inertness with respect to adsorption of residual gases. The end of the Ir wire is bent by 90° towards the sample, and the tip is fabricated by electrochemically etching this end in molten NaCl. The NaCl is contained in a graphite crucible, which is held at a potential of -2.5 V with regard to the specimen for $\simeq 2$ s.[34] Tip radii of $\lesssim 1000$ Å are obtained, as estimated from SEM pictures. A typical example is shown in Fig. 8. Before being transferred to the AFM, the tip is heated to 1300 K by an electron gun.

The sensor plates are spring mounted on a Macor block, which is screwed into the vertex of the piezo tripod. The plates are cut using a diamond pen from doped Si ⟨111⟩ (Pensilco). They are coated with an evaporated gold film over a chromium underlayer in the region of the spring mounting to eliminate problems of contact resistance.

The two plates are chosen close enough to be coupled by a capacitance C_c of 0.1 pF, which mixes the signals for the cantilever deflections in the y and z directions. For example the effective capacitance C_y' of the y sensor plate includes the capacitance C_y of the gap between the y sensor and the cantilever and the capacitance of C_c acting in series with the capacitance C_z of the gap between z sensor and the cantilever:

$$C_y' = C_y + \left(\frac{1}{C_c} + \frac{1}{C_z}\right)^{-1}. \tag{21}$$

Since C_y and C_z are about 1 pF, $dC_y'/dC_z \simeq 0.01$, and the interaction between y and z is only about 1%, much smaller than interactions due to inexact relative positioning of the sample, wire and sensor plates. In any case, the interaction can be measured by moving the sensor with the piezos in well-defined directions, and later this effect can be removed

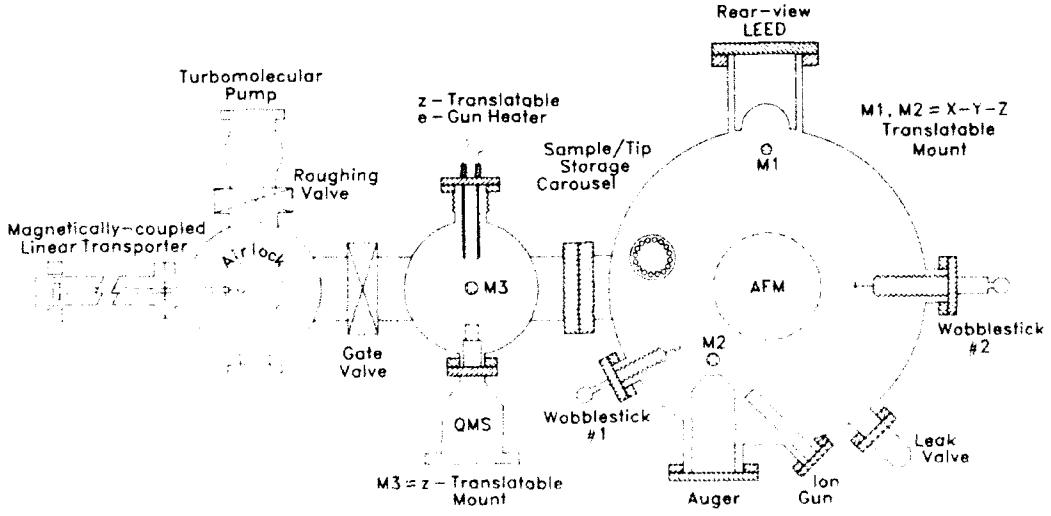

FIG. 7. Schematic top view of the UHV chamber, showing the surface analysis instrumentation, and different sample mounts that allow their use. Wobblestick no. 1 is used to move samples/tips between the carousel, LEED mount, Auger/ion gun mount, and the AFM. The linear transporter transfers between the airlock, heater, QMS mount, and the carousel. Wobblestick no. 2 is used for mechanical (gross adjustments) of the AFM sample and sensor positions. A 150 l/s ion pump provides pumping for the main chamber. Both the airlock region and main chamber are roughed by a 50 l/s turbomolecular pump.

by applying a linear transformation to the y and z data.

The electronics circuitry is mounted in a 38-mm-diam tube, which is sealed with an atmosphere of argon to aid leak detection and clamped directly into the base plate of the AFM. The wire (teflon-clad copper wire with 0.15 mm outer diameter from the California Fine Wire Co.) leading from the sensor plates to the circuit is about 80 mm long. All electrical connections to the AFM are made through feedthroughs in the top flange. To reduce stray capacitance, all signal lines are shielded from each other and especially from the wires carrying the piezo voltages. To avoid vibrational coupling of the AFM to the outside through these relatively stiff wires, a connector board on top of the AFM connects them to the weaker wires described above, which finally lead to the AFM. Other wires, such as those inside the tube between the circuit board and UHV feedthroughs, are stiffer. It was found that vibration of circuit parts and connecting wires could contribute to the noise.

All the piezo scan voltages, capacitance sensitivities, tunneling current, and y and z cantilever motions are recorded on video tape using an A. F. Vetter Co model 4000 16 channel analog-digital processor and Panasonic model AG1230 VCR. For analysis, this data is transferred to an IBM PC-AT.

A. Experimental procedure

To achieve optimum sensitivity, the two sensor plates are first brought into contact with the cantilever (for unidirectional force detection only one plate is used). Depending on whether the cantilever-sensor contact is insulating (due to contaminations) or conducting, contact is detected by an insensitivity of the capacitance signal to sensor position or by a sudden off-scale signal. The plates are then taken back to a position as close as possible to the wire without achieving snapping of the wire into the sensor plates or touching of an asperity on wire or plates. To calibrate the relation of detector output to cantilever displacement, the sensor plates are oscillated by the piezoelectric tubes over a known distance, and the amplitude of the signal modulation is recorded. Even before snapping occurs, the attractive force of the sensor plates on the cantilever reduces the effective cantilever force constant by adding a downward curving potential to the upward curving parabolic potential of the cantilever. The extent to which the force constant is modified can be determined by vibrating the cantilever and measuring the resonant frequency shift. Two nearly equal, low resonance frequencies are found, because the doubly degenerate resonance frequency of a straight wire is split when it is bent.

For conducting samples, the coarse approach of the sample toward the tip can be monitored electrostatically by applying a 30-V p-p triangle wave to the sample. Then, while bringing the sample toward the tip using alternately mechanical and piezoelectric motion, the normal electrostatic force[10,16] is monitored through phase-sensitive detection of the cantilever deflection at twice the frequency of the triangle wave. By comparison of the cantilever deflection with that calculated from the tip radius, the sample is brought to within 500–2000 Å of the tip. For a friction measurement (with both plates close to the wire), the sample is then advanced slowly (several Å/s) up to and beyond the point where hard contact occurs, and then backed out to separation. Simultaneously, the sample is oscillated in the friction-sensitive y direction at 1–10 Hz. Because the change in z is slight for each y oscillation, each such loop gives an average frictional force for a particular average load.

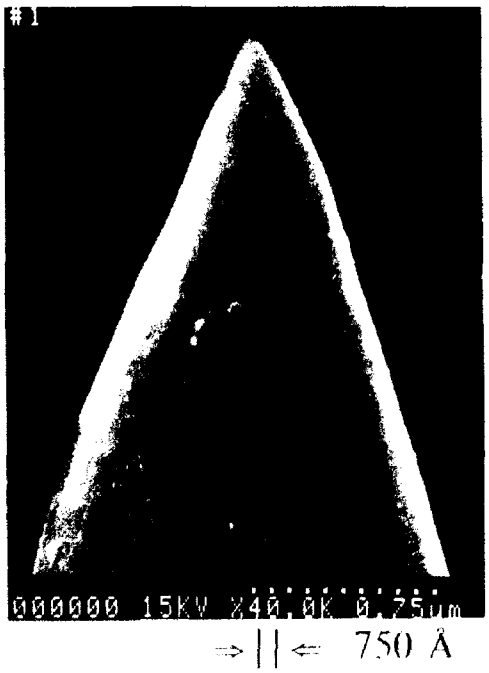

FIG. 8. Electron micrograph of Ir tip etched electrochemically in molten NaCl with tip radius of ~700 Å.

V. RESULTS

Our AFM has been used to study several different systems: Iridium tips on highly oriented pyrolytic graphite (HOPG) and Au(111) films, tungsten on SiO_2, and diamond tips on diamond films. Detailed analysis of these results is published elsewhere.[2,3,35] Here, the bidirectionality of the instrument in the dc mode will be shown with the HOPG data, and the imaging capabilities demonstrated through pictures of diamond films.

A. Friction of an iridium tip on highly oriented pyrolytic graphite

The graphite sample used in our experiment was cleaved in air by peeling a thin layer of graphite from the sample with adhesive tape immediately before loading it into vacuum. Figures 9 and 10 represent a friction experiment performed as described above. The z advance is 8 Å/s and the y oscillation is 20-Å p-p at 2 Hz. A typical loop obtained during one such y oscillation of the sample is shown in Fig. 9, displaying the deflection of the cantilever in the lateral (a) and normal direction (b) versus the sample y displacement. In (a) numbers indicate different regions of the loop: Just after the sample changes direction the loop shows a sticking region

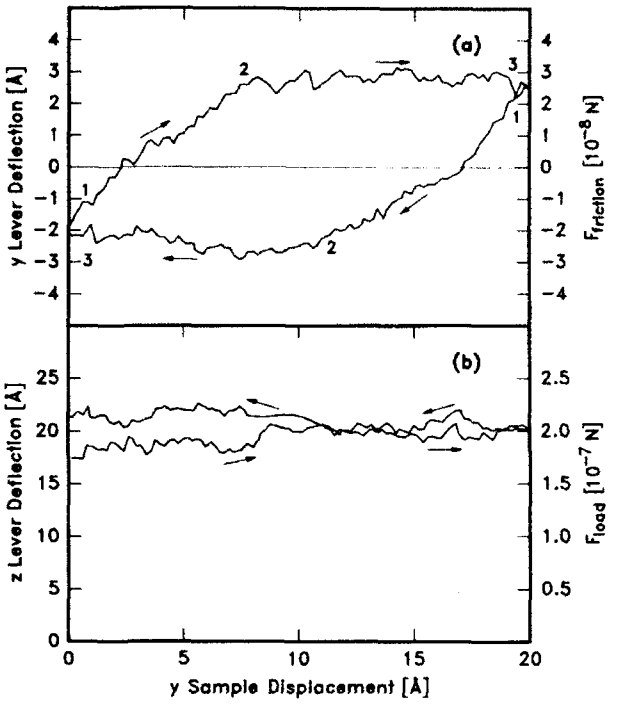

FIG. 9. (a) Lateral and (b) normal deflection of the cantilever ($k = 100$ N/m), as the sample undergoes one complete oscillation in the lateral direction. Numbers in (a) indicate different regions of the friction loop: 1–2, sticking region; 2–3, sliding region.

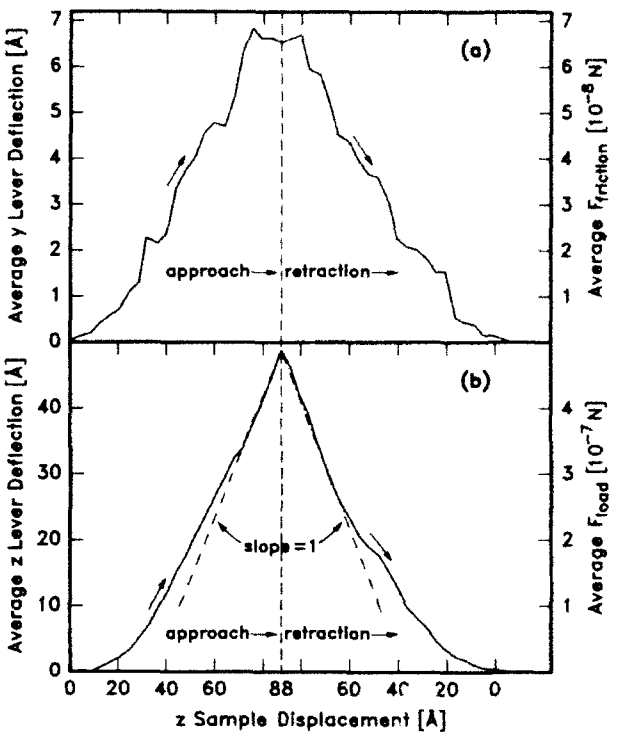

FIG. 10. (a) Average lateral and (b) normal deflections of the cantilever vs the sample z displacement. Arrows indicate approach and retraction.

(1–2), with a slope (i.e., cantilever y deflection per sample y displacement) of one. When the restoring force of the bending wire overcomes the static friction (point 2), the tip slides across the surface (2–3) until the turnaround at point 3.

Figure 10 shows a friction experiment in which a freshly cleaved HOPG surface is contacted with a new Ir tip with a radius of 1500 Å and spring constant of 100 N/m. Here, the utility of bidirectional sensing is demonstrated. The load and friction values for this figure have been measured simultaneously, obviating the need to make assumptions about sample compliance or elasticity. Average lateral (a) and normal (b) deflections of the cantilever, deduced from each loop, are plotted versus the z displacement of the sample, as it is advanced towards the tip and then retracted again at the same rate. The average frictional force is obtained from half of the average loop height multiplied by the wire spring constant. The average load is computed from the average normal cantilever deflection which, in these experiments (Fig. 9), does not change by more than 4 Å during one y oscillation. In Figs. 9 and 10, the dc deflection of the cantilever in the two orthogonal directions is computed directly from the measured capacitance change, without the employment of feedback electronics to adjust the sensor position. As can be seen from the loop in Fig. 9(a), the cantilever deflection noise is approximately 0.3-Å p-p. The effective bandwidth, determined by the sampling rate, is dc to 200 Hz. The structure in the sliding part of the loop in Fig. 9(a) could be an indication for a modulation of the frictional force with the underlying sample lattice, as it was found for graphite in air.[9] the noise in this experiment is too high to clearly distinguish a periodicity.

The most striking feature in Fig. 10 is the slow onset of the normal cantilever deflection as the sample is advanced towards the tip. Only at higher loads is the cantilever eventually bent backwards at the same rate as the sample, resulting in a slope of 1 in curve b at higher sample z displacements. The reversibility of this behavior, as indicated by the subsequent retraction, indications that the deformation is elastic. As discussed elsewhere,[2] the elastic response to a given load is much greater than predicted from a model based on the bulk elastic constants of graphite, an effect that may be due to delamination and bending of a graphite flake normal to the surface. From Fig. 10 we derive a friction coefficient of 0.25, much higher than the values previously reported for metal tips on graphite. Since this value was obtained on the first approach of the sample to the tip, it is likely that much lower friction coefficients for single tips on graphite are attained only after a flake has broken off the surface and attached to the tip.

B. Diamond tip/diamond film interactions

The imaging capabilities of the AFM in the ac mode were tested in both the contacting (repulsive) and noncontacting (attractive) profiling mode. In the attractive mode the cantilever was vibrated at 1 Hz above its resonance frequency at an amplitude of 20-Å p-p. Since the compliance of the cantilever is changed due to the attractive force derivative between tip and sample, the vibration amplitude of the

cantilever is reduced as a consequence of a lowering of the resonance frequency.[11,16] Profiling of the surface was accomplished by a feedback circuit that kept the tip-sample spacing constant by maintaining the vibration amplitude of the cantilever at 50% of its resonant value. In the repulsive mode the tip was vibrated with an amplitude of 5–20 Å *p-p* at a frequency of several hundred Hz, depending on cantilever spring constant and resonance frequency. When the sample is brought to within the range of the tip vibration, the amplitude is reduced due to the hard contact of tip and sample. In this application profiling was accomplished by a feedback circuit that kept the tip-sample spacing constant by preserving a reduction of $\simeq 20\%$ in the tip modulation amplitude.

The diamond tip was obtained by gluing a small diamond fragment, $\simeq 200\,\mu$m across, to the end of a cantilever made from tungsten wire. A spring constant of 20 N/m was calculated from the geometry of the wire and confirmed from the resonance frequency. The diamond films used in our experiments were prepared in two different ways: Film I was deposited in another vacuum chamber onto a silicon substrate, at 1100–1300 K by hot filament chemical vapor deposition. The film was characterized by Raman spectroscopy and SEM photographs, which showed diamond crystals typically $\simeq 2\,\mu$m across.[36] Film II was prepared on a silicon substrate, in a microwave plasma deposition chamber.[37] To learn about the film topography at the film-/substrate interface, the silicon substrate was etched away, and the resultant coherent film glued upside down onto a second silicon substrate. Both films were kept in laboratory air for a couple of weeks before being loaded into the AFM without further treatment.

Figure 11 shows an example of an attractive mode image of film I over an area of 500 Å $\times$ 400 Å. The image reveals a small scale roughness not visible in the SEM pictures, as features of only a couple of Å high can clearly be resolved. We assume that over a such small scanning area the tip is actually profiling a single-crystal plane of a diamond crystallite. A detailed account of our investigation of frictional forces of this film will be deferred to a later publication.[35] Figure 12 shows an example for a repulsive mode image of film II over an area of $\simeq 5000$ Å $\times$ 7000 Å. Relatively small features are again resolved, with heights ranging from 10 to 100 Å.

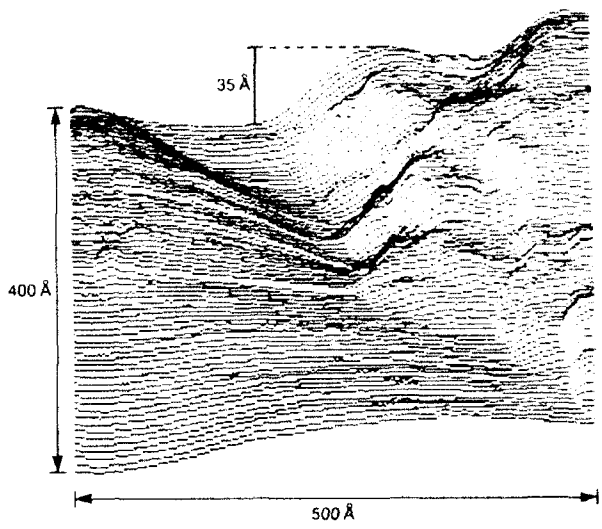

FIG. 11. Attractive mode line-scan image of diamond film I. Scanned area was 500 Å $\times$ 400 Å (x,y). The offset between lines is 5 Å in y. The bar shows the vertical (z) dimension corresponding to 35 Å. The lateral resolution, demonstrated by the narrowest stepwidth seen, is 30 Å.

VI. DISCUSSION

The theoretical performance of this capacitance AFM is comparable to, or better than, that of other AFMs in current operation, although due to roughness our observed noise level is nearly one order of magnitude worse than best reported results using optical fibers. From the measured signal, 1×10^{-3} V/Å, taking the calibration factor of the circuit of 1.2×10^{14} V/F into account, we find an actual sensitivity during the experiment of only $\simeq 1\times10^{-7}$ F/m, several times lower than the expected sensitivity (see Sec. III). A close examination of wire and capacitor plates showed that, in practice, our minimum working distance and consequently our maximum sensitivity is not determined by the theoretical operating distance d_{op} ($\alpha = 0.5$), but rather is limited by the roughness of the wire and/or dust particles attached to wire or plates. Particulates in the size range 0.1–10 μm represent a significant fraction of laboratory particles.[38] While the polished silicon wafers are smooth to better than 100 Å, the wire is manufactured by an extrusion process, and SEM pictures of uncleaned wires show both grooves along the length of the wire, and particles $\lesssim 10\,\mu$m seemingly stuck to the surface. To alleviate the smoothness problem to some extent, a rather high voltage of 3.5-V RMS

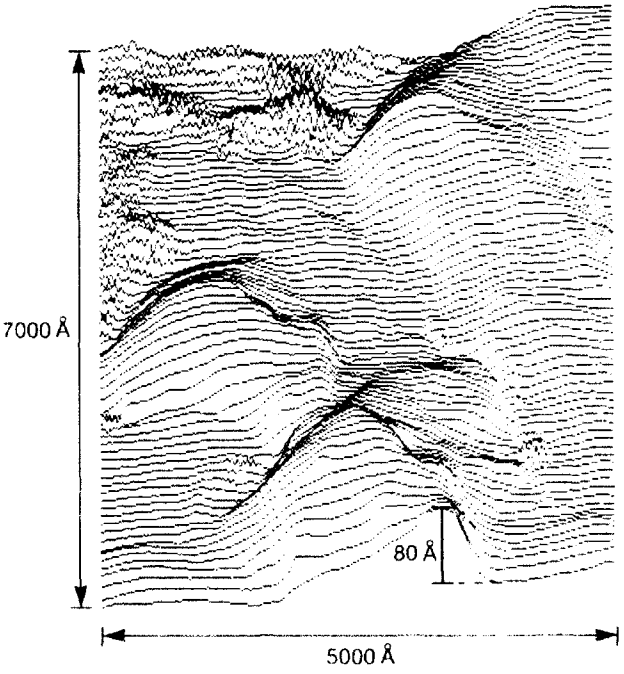

FIG. 12. Repulsive mode line-scan image of diamond film II. Scanned area was 5000 Å $\times$ 7000 Å. Offset between lines is 100 Å. The bar shows the vertical dimension, corresponding to 80 Å. The lateral resolution is 60 Å.

was applied to the sensor plates which sets the snapping distance d_{op} ($\alpha = 0.5$) to 490 Å and the sensitivity to 4.0×10^{-7} F/m (Sec. III). Still, we usually have to work at an actual distance of up to 5 times bigger than d_{op} so that theoretically a sensitivity of $\simeq 1 \times 10^{-7}$ F/m is to be expected. This is found experimentally. Polishing methods for obtaining smoother wires to work closer to the snapping distance are currently under study in our laboratory. Ideally, dust-free conditions should also be maintained both while preparing cantilevers and sensor for operation, and within the UHV chamber.

Whereas optical techniques for sensing AFM cantilever deflection are fundamentally constrained by photon shot noise, no such limit applies to the capacitance technique. The essential limitations of our detection scheme arise from the properties of the input transistor. One way to overcome these limitations is to use a resonant input stage, so that the sensor current changes more rapidly than linearly with respect to the capacitance. Such a circuit would best operate with a FET input which, due to its high impedance, would damp the resonant circuit minimally. The higher voltage noise of the FET input would be outweighed by the resonant signal enhancement. Such a resonant circuit would probably decrease the noise of our circuit by an order of magnitude, so that even with the crude wire plate geometry, the noise level would match that of the best optical techniques. Using a microfabricated flat geometry, much better sensitivity could be attained.

As discussed above in detail, increasing the rf voltage used for capacitance sensing increases the displacement sensitivity of the sensor, but the voltage must be limited to avoid letting the electrostatic force snap the lever into the sensor plate. In a microfabricated cantilever-sensor system, this problem can be avoided by balancing out the electrostatic force with two sensor plates, one on the sample side of the cantilever, and one on the opposite side. Then the sensor-cantilever distance and voltage can be adjusted to give a much better S/N than would be possible for one plate alone.

One disadvantage of all AFMs used to date is that to detect the force on the tip, the force must be allowed to displace the tip. The relative position of the tip with respect to the sample is the difference between the measured lever position and the controlled sample position. This complication can be avoided by using a zero displacement force sensor. In this scheme, the force on the tip would be balanced by an opposing force, which would be adjusted by a feedback loop to keep the lever displacement zero. This method could in principle be applied with any method of deflection detection, but it is particularly well suited to the capacitance technique, in which the sensor electrode is already available for applying the opposing force. The opposing force could be applied to the sensor plate by a variable dc bias superimposed on the rf sine wave. The effective force constant of the lever could be varied by adjusting the gain of the feedback loop controlling the opposing force. Using this method, the dynamic range of measurable forces is not limited by the range of measurable lever displacements.

This zero displacement technique could be implemented by using two opposing sensor plates, one for attractive and one for repulsive forces. Alternatively, a single sensor plate could be used by applying a nonzero dc bias at zero tip force, so that the lever is pulled by the electrostatic force against its own mechanical restoring force.

In conclusion, we have presented a new detection method, based on capacitance measurement, for sensing the cantilever deflection in an atomic force microscope, and employed it for the investigation of tribological properties (i.e., friction, lubrication, and wear) of various samples. The new AFM offers a low noise level at frequencies near dc, is UHV compatible, and bidirectional: Frictional force and load are determined simultaneously by measuring the capacitance change between the cantilever and two orthogonal plates. Theoretically, the instrument should achieve 0.03-Å RMS noise in the 0.01 to 1000 Hz bandwidth. In actuality, we observed 0.1-Å RMS. It is hoped that by reducing the sensor roughness we will be able to approach the theoretical sensitivity. The bidirectional operation of our instrument in the dc mode has been demonstrated by the frictional data obtained using an iridium tip on HOPG. Imaging capabilities of our instrument have been shown in both the contacting and noncontacting profiling mode through images obtained with a diamond tip on diamond films.

ACKNOWLEDGMENTS

We are pleased to acknowledge S. Chiang, R. J. Wilson, and C. T. Rettner for helpful discussions, J. E. Schlaegel and B. A. Hoenig for technical assistance, and A. Badzian and T. Badzian for providing diamond film II. This work was partially supported by the Office of Naval Research under Contract No. N00014-88-C-0419, and by the AFOSR under Contract No. F49620-89-C-0068. S. R. C. thanks the Myron A. Bantrell trust for support through a Chaim Weizmann postdoctoral fellowship.

[1] G. Binnig, C. F. Quate, and Ch. Gerber, Phys. Rev. Lett. **56**, 930 (1986).
[2] G. Neubauer, S. R. Cohen, and G. M. McClelland, Mater. Res. Soc. Symp. Proc. **153**, 307 (1989).
[3] S. R. Cohen, G. Neubauer, and G. M. McClelland, J. Vac. Sci. Technol. A (to be published).
[4] T. Göddenhenrich, H. Lemke, U. Hartmann, and C. Heiden, J. Vac. Sci. Technol. A **8**, 383 (1990).
[5] Y. Kuk and J. Silverman, Rev. Sci. Instrum. **60**, 165 (1989).
[6] P. K. Hansma, V. B. Elings, O. Marti, and C. E. Bracker, Science **242**, 209 (1988).
[7] G. Neubauer and G. M. McClelland (unpublished work).
[8] S. Gould, O. Marti, B. Drake, L. Hellemans, C. E. Bracker, P. K. Hansma, N. L. Keder, M. M. Eddy, and G. D. Stucky, Nature **332**, 332 (1988).
[9] C. M. Mate, G. M. McClelland, R. Erlandsson, and S. Chiang, Phys. Rev. Lett. **59**, 1942 (1987).
[10] R. Erlandsson, G. Hadziioannou, C. M. Mate, G. M. McClelland, and S. Chiang, J. Chem. Phys. **89**, 5190 (1988).
[11] R. Erlandsson, G. M. McClelland, C. M. Mate, and S. Chiang, J. Vac. Sci. Technol. A **6**, 266 (1988).
[12] H. J. Mamin, D. Rugar, J. E. Stern, B. D. Terris, and S. E. Lambert, Appl. Phys. Lett. **53**, 1563 (1988).
[13] D. Rugar, H. J. Mamin, R. Erlandsson, J. E. Stern, and B. D. Terris, Rev. Sci. Instrum. **59**, 2337 (1988).

[14] D. Rugar, H. J. Mamin, and P. Günther, Appl. Phys. Lett. **55**, 2588 (1989).
[15] S. Breen, B. E. Paton, B. L. Blackford, and M. H. Jericho (to be published).
[16] Y. Martin, C. C. Williams, and H. K. Wickramasinghe, J. Appl. Phys. **61**, 4723 (1987).
[17] C. Schönenberger and S. F. Alvarado, Rev. Sci. Instrum. **60**, 3131 (1989).
[18] D. Sarid, D. Iams, and V. Weissenberger, Opt. Lett. **13**, 1057 (1988).
[19] D. Sarid, D. A. Iams, J. T. Ingle, V. Weissenberger, and J. Ploetz, J. Vac. Sci. Technol. A **8**, 378 (1990).
[20] G. Meyer and N. M. Amer, Appl. Phys. Lett. **53**, 1045 (1988).
[21] S. Alexander, L. Hellemans, O. Marti, J. Schneir, V. Elings, P. K. Hansma, M. Longmire, and J. Gurley, J. Appl. Phys. **65**, 164 (1989).
[22] R. V. Jones and J. C. S. Richards, J. Phys. E **6**, 589 (1973).
[23] J. L. Garbini, L. J. Albrecht, J. E. Jorgensen, and G. F. Mauer, J. Dynamic Systems, Measurement, and Control, Trans. ASME Ser. G **107**, 192 (1985).
[24] J. R. Matey and J. Blanc, J. Appl. Phys. **57**, 1437 (1985).
[25] C. D. Bugg and P. J. King, J. Phys. E **21**, 147 (1988).
[26] C. C. Williams, W. P. Hough, and S. A. Rishton, Appl. Phys. Lett. **55**, 203 (1989).
[27] R. C. Palmer, E. J. Denlinger, and H. Kawamoto, RCA Rev. **43**, 194 (1982).
[28] Y. Martin, D. W. Abraham, and H. K. Wickramasinghe, Appl. Phys. Lett. **52**, 1103 (1988).
[29] J. E. Stern, B. D. Terris, H. J. Mamin, and D. Rugar, Appl. Phys. Lett. **53**, 2717 (1988).
[30] K. E. Peterson, Proc. IEEE **70**, 420 (1982).
[31] W. Y. Lee, R. Sequeda, J. Salem, and D. Chapman, Appl. Phys. Lett. **50**, 522 (1987).
[32] J. P. Den Hartog, *Mechanical Vibrations* (McGraw-Hill, New York, 1956), pp. 148 ff.
[33] G. Binnig and D. P. E. Smith, Rev. Sci. Instrum. **57**, 1688 (1986).
[34] C. J. Smithells, *Metals Reference Book*, 3rd ed. (Butterworths, Washington, DC, 1962), Vol. 1, p. 256.
[35] G. Neubauer, S. R. Cohen, G. M. McClelland, and H. Seki, MRS Symp. Proc. (in press).
[36] M. Buck, T. J. Chuang, J. H. Kaufman, and H. Seki, MRS Fall Meeting Symp. Proc. (to be published).
[37] Sample was prepared at Penn State and provided by A. Badzian and T. Badzian.
[38] P. R Austin, *Design and Operation of Clean Rooms* (Business News, Troy, MI, 1970).

4. T. Miyamoto, I. Sato, and Y. Ando, Tribology and Mechanics of Magnetic Storage Systems, Vol. V, STLE SP-25, 55 (1988).

5. E Rabinowicz, Friction and Wear of Materials, J. Wiley and Sons, 1965.

6. M.F. Doerner and W.D. Nix, J. Mater. Res. 1 (4), 601 (1986).

7. R. S. Timsit and G. Stratford, Tribology and Mechanics of Magnetic Storage Systems, Vol V., STLE SP-25, 17 (1988).

8. M. Ronay, Phils. Mag, 42, 161 (1979).

9. S. Suzuki and F.E. Kennedy, Jr., IEEE Trans Mag, 25 (5), 3728 (1989).

10. G.M. Hamilton and L.E. Goodman, ASME J. App. Mech., 33, 372 (1966).

NANOTRIBOLOGY OF DIAMOND FILMS STUDIED BY ATOMIC FORCE MICROSCOPY

GABI NEUBAUER[1], SIDNEY R. COHEN, GARY M. MCCLELLAND, AND HAJIME SEKI
IBM Research Division, Almaden Research Center, San Jose, CA, 95120-6099.

ABSTRACT

An atomic force microscope, operated in ultra-high vacuum has been employed to study the tribological properties of diamond films under small loads ($< 10^{-6}$ N) on a nanometer scale. The incidence of intermittent motion, "stick-slip", while sliding a diamond tip across the diamond film, is detected under certain experimental conditions and is discussed with respect to the difference between static and kinetic friction, sample topography and a varying sample condition.

INTRODUCTION

Diamond and thin films of diamond combine such properties as high hardness, high rigidity and abrasion resistance, chemical inertness, high electrical resistivity and high thermal conduction[1, 2]. An understanding of the mechanical and tribological behavior (friction, lubrication and wear) of diamond films becomes more and more important, as the range of their expected applications, such as heat-sinks in electronic circuitry, cutting tools in tool manufacture, or wear-resistant coatings in general, increases. Recently, tribological research on diamond films, involving larger scales than studied here, have been reported [3, 4, 5]. Studies on diamond single crystals sliding on each other reported friction coefficients varying between $\approx$ 0.05-0.9, depending on the cleanliness of the surface [6, 7] as well as the crystallographic direction of sliding [8-14]. Similar findings have to be expected in experiments on diamond films over small enough sliding regions. We report here nanometer scale experiments on single crystals composing diamond films.

Tribological events occurring at the interface of two sliding macroscopic surfaces are governed by the small areas of contact between asperities of the two solids. To gain insight into the fundamentals of tribological processes we are concentrating on the study of single asperity contacts and employ an atomic force microscope (AFM) for ultra-high vacuum experiments in tribology on the nanometer and subnanometer scale. In the AFM [15], forces between a tip (i.e., the single asperity) and a surface are detected by measuring the deflection of a flexible cantilever upon which the tip is mounted. Upon rastering the sample while keeping the tip under a constant force, i.e., constant spacing to the sample, topographical images of the sample can be obtained. Our AFM combines imaging capabilities with the simultaneous measurement of cantilever deflection both perpendicular and lateral to the surface, thus determining load and frictional force, respectively. It has been used in a recent UHV study of the tribology of a Ir tip on a Au surface [16]. In this paper, we describe the observation of a small scale intermittent motion of a diamond tip sliding across a diamond film.

EXPERIMENTAL

The experimental apparatus has been described in full elsewhere [17]. In brief: The AFM is supported in a UHV chamber equipped with surface analysis instrumentation, such as LEED, Auger, ion sputtering gun, electron gun heater, and airlock for sample and tip transfer. Chamber pressure is in the 10^{-10} Torr ($\approx 10^{-8}$ Pa) range. The diamond tip was obtained by gluing a small diamond fragment, $\simeq$ 200μm across, obtained by shattering a diamond in air between two stainless steel plates, to the end of a cantilever made from tungsten wire. A spring constant of 8 N/m was calculated from the geometry of the wire and confirmed from the resonance frequency, 1960 Hz. To measure the lateral (frictional) and normal force (load) on the tip while it is sliding

Mat. Res. Soc. Symp. Proc. Vol. 188. ©1990 Materials Research Society

across the sample, the bending of the wire is sensed by measuring the capacitance between the wire and each of two orthogonal sensor plates, cut from a Si-wafer. Although better performance of this instrument is achievable the noise in these experiments was about 5 Å peak-to-peak (p-p) because the surface roughness of the wire made it impossible to position the sensor plates closer than $\simeq$ 5000 Å from the wire. Forces are obtained by multiplying the measured deflections of the wire by its spring constant. Both sample and sensor plates are mounted on piezo-tripods, allowing their movement in all three orthogonal directions. The diamond film used in our experiments was prepared in another vacuum chamber by hot filament chemical vapor deposition onto a silicon substrate, at 1100-1300 K with a 1% mixture of methane in hydrogen at 5.3-6 kPa [18, 19]. The film was characterized by Raman spectroscopy and SEM images, which showed diamond crystals typically $\simeq 2\mu$m across. The film was kept in laboratory air before being loaded into the AFM without further treatment. Due to the method of preparation the diamond film is hydrogen terminated and, once the film is exposed to air, adsorbed organic contaminants are undoubtedly present on the film. Not only such contaminants, but also the hydrogen termination itself influences the frictional behavior of diamond: In studies of copper sliding on diamond an increase of the interfacial shear of the metal-diamond interface was found when the hydrogen was gradually removed by increasing the annealing temperature [20].

For a friction measurement the sample is slowly advanced in the normal (z) direction (several Å/s) up to and beyond the point where hard contact occurs, and then backed out to separation. Simultaneously, the sample is oscillated in the friction-sensitive y-direction with an amplitude of 100-200 Å p-p at 1-10 Hz. Because the change in z (the load) is slight for each y oscillation, each such loop gives an average frictional force for a particular average load.

RESULTS

AFM images were made in both the contacting (repulsive) and the non-contacting (attractive) profiling mode [21, 22]. The topography could be divided into relatively flat regions extending several hundred Å with a roughness of several Å and rough regions where height variations of several hundred Å were seen in a scan of several thousand Å. Friction experiments were always carried out in the flat regions where the tip is most likely profiling a single crystal plane of a diamond crystallite.

Figure 1 represents a friction experiment performed as described above with a z-advance of the sample of 8Å/s and a y-oscillation of 200 Å p-p at 2Hz: Friction loops, each obtained during one such y-oscillation of the sample are shown, displaying the deflection of the cantilever in the lateral direction vs. the y sample displacement. Labels show the average load for each loop, as derived from the average normal (z) lever deflection. In the first loop numbers indicate different regions of the loop: Just after the sample changes direction the loop shows a sticking region (1-2), with a slope of one. When the restoring force of the bending wire overcomes the static friction (point 2), the tip slides across the surface (2-3) until the turnaround at point 3.

A striking feature in the loops is the occurrence of an intermittent "stick-slip" motion, in the assumed-to-be sliding region of the tip (2-3), which becomes more pronounced at higher loads. Looking at the slips with a higher time resolution than in figure 1 reveals that they occur instantaneously within the time constant of our electronics, 200 μs. The size of the slips reaches from $\leq$ 10 to $\geq$ 30 Å which is well beyond the noise level of 5 Å p-p. This behavior has not been observed in all friction experiments conducted on this film, but seemed to be dependent on both the spot of the surface and the applied load, possibly being below the noise limit for low loads. In experiments not displaying stick-slips, an average (static) frictional force for each loop could be computed and friction coefficients derived: Again depending on the spot of the surface, values were around either $\simeq$ 0.2 or $\simeq$ 0.8. In either case, i.e., high or low friction, the friction coefficient decreased with increasing load, the values above being the ones for the lowest loads.

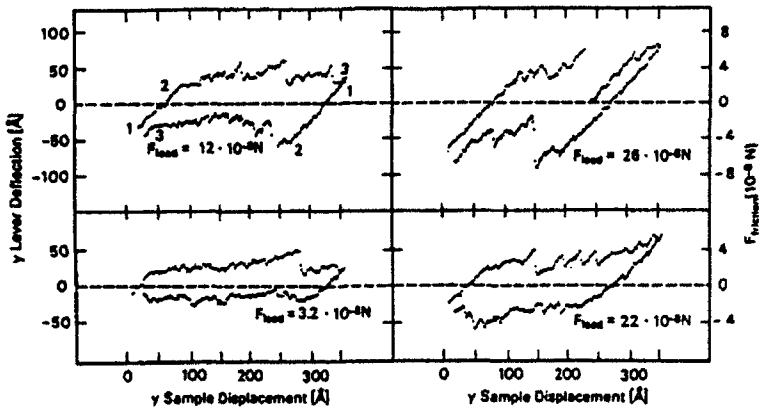

Figure 1: Lateral (y) deflection of the cantilever (k=8N/m) and the derived frictional force, as the sample undergoes complete y-oscillations, each for a different average load. Numbers in the first loop indicate different regions of the friction loop: 1-2, sticking region, 2-3, sliding region.

DISCUSSION

The contact area in our experiments is slightly larger than a single atom, which is very much smaller than that employed in previous studies of diamond tribology. The fracture process used to form the tip probably creates a nearly atomically sharp tip, which is somewhat blunted after initial contact with the surface. Even for a relatively large tip radius of 100 Å, the contact diameter calculated from the elastic constants of diamond is 11 Å for a 10^{-7} N load. Under these conditions the contact pressure is a factor of two above the elastic limit for larger contacts given by the Knoop hardness of 7000 kg/mm^2. However, because of the reduced effect of imperfections, very small contacts are expected to show a much larger plastic threshold than larger contacts. Because of the very small contact area, we expect the frictional force to reflect minute variations in the topography and condition of the surface.

The incidence of intermittent motion during sliding, the "stick-slip", is an often observed phenomenon in friction experiments on a wide range of material combinations, including diamond on diamond [6]. Previous studies on friction of diamond were carried out on much larger scales, usually involving sliding speeds of several hundred μm/s and loads $> 10^{-2}$ N. The friction-speed characteristic, i.e., the difference between static and dynamic friction, the scanning speed, the elasticity of the sliding surfaces, as well as the sequence of events during the slip itself regulate the extent to which stick-slip type motion takes place [23]. On the other hand, in friction experiments on the atomic scale, frictional forces have been reported showing stick-slips reproducing the periodicity of the underlying sample lattices of highly oriented pyrolytic graphite and mica [24, 25]: The tip motion could be described by the sum of a conservative, periodic tip-surface force and the nonconservative restoring force of the wire opposing the direction of motion. However, with the instrument's performance in these experiments we could not resolve such periodicity.

Other factors have to be considered responsible for the stick-slip behavior. The most obvious one, besides the friction-speed characteristic, is the surface topography: Large asperities or steps

on the surface or spots of higher adhesion than the surroundings might cause the tip to stick to the surface and prevent it from moving continuously. Therefore, in a detailed analysis, to obtain the tip motion relative to the actual position of the tip on the surface, each originally obtained friction loop has to be transferred to a graph of y lever deflection vs. the difference of y sample displacement and y lever deflection. This is demonstrated in figure 2 for several consecutive loops at increasing loads. In this figure sticking regions of the tip are now the vertical parts of the loops, sliding is horizontal, whereas the slips appear as lines with a slope of -1.

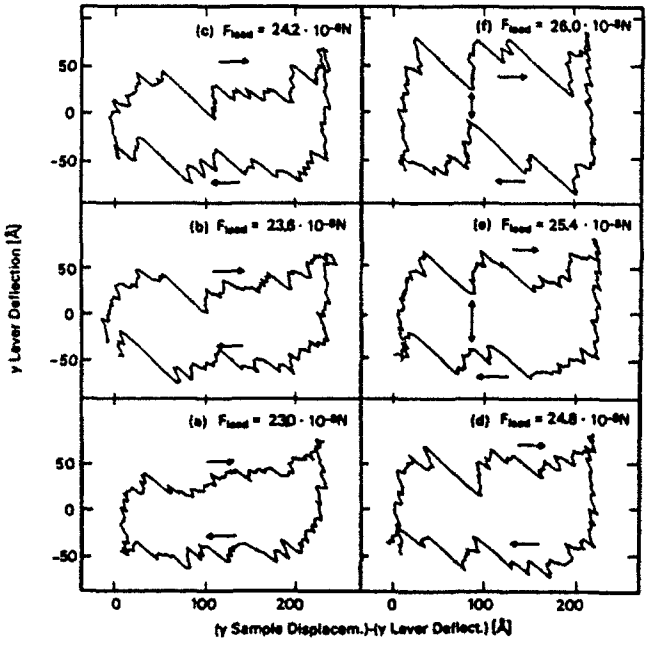

Figure 2: Lateral (y) deflection of the cantilever vs. the difference of y sample displacement and y lever deflection. For details see text.

Comparison of the loops should give some insight into the origin of the intermittent motion: If the stick-slips were caused by the sample topography, all slips should occur at the same spots of the sample and the loops should display the same principal features. Whereas the slips indeed seem to coincide at the start (i.e., upper left corner) of the loops, others clearly do not match. Since in our experimental setup the measurement of the z lever deflections not only determines the load, but also probes the topography of the sample itself, any large asperities or steps should be indicated by a corresponding signal in the z deflection when the slip occurs. No such correlation was found. In some loops (fig. (e) and (f), see vertical arrows) the tip seems to stick at the same spot on the surface independent of the direction of motion. This observation cannot easily be explained by a surface asperity or step because the finite width of such a feature would require the sticking in the different directions to be displaced from one-another. A more plausible explanation would be a higher frictional force due to the surface structure of the diamond or possible adsorbates.

An indication for such contamination is found in the attractive tip-surface force, which displays a hysteresis, being higher during unloading (1.4×10^{-8} N) than loading (4×10^{-9} N).

A velocity effect cannot be considered the only cause of intermittent motion either, because such an effect would be independent of the scanning direction, the y lever deflection should look alike after each turnaround of the sample, leading to a point symmetry of the loops. However, this symmetry could be somewhat distorted by an asymmetry in the tip shape.

To gain some insight into the difference between static and dynamic friction and their dependence on load, we applied a very simple analysis of the data, using only a contribution of static friction, F_s, and velocity-independent dynamic friction, F_d, thus excluding contributions by damping [23]. Under the assumption that the scanning speed of the sample is negligible compared to the actual velocity of the slip itself, the time duration of the slip is given by:

$$t_{slip} = \frac{1}{2f_{res}}, \tag{1}$$

where f_{res} is the resonant frequency of the lever. For the lever used in these experiments (f_{res} = 1960 Hz) we obtain $t_{slip} = 250\mu s$, which is consistent with our observation. The size of the slip is obtained by:

$$y_{slip} = \frac{2(F_s - F_d)}{k}. \tag{2}$$

Thus, with the static frictional force obtained from the lever deflection at the end of the stick, the dynamic frictional force is derived from the y lever deflection at the midpoint of the slip.

Analyzing the data in this manner, we find, in analogy to our static friction results from experiments with no stick-slip, a sublinear dependence of friction on load. In a linear region of the plot, at higher loads between 1×10^{-7} N and 3×10^{-7} N, we derive friction coefficients for the dynamic friction of $\mu_d = 0.16$ and for the static friction of $\mu_s = 0.26$. Such sublinear dependence of friction on load has been found ealier [6] and was attributed to an elastic response of the diamond surface. In a recent work [11, 12], elastic deformation was not necessarily reflected in the dependence of the friction coefficient on load: depending on contact pressure and sliding direction μ was found to be independent, decreasing, or even increasing with contact pressure. An increase of the friction coefficient with load under certain conditions was also found by others [14]. Anisotropy in diamond friction has been reported in many studies with friction coefficients varying by a factor of 2-3 [8-14]. Contact pressure was found to be an important factor [12]. Others reported almost no anisotropy for low loads and attributed the increasing anisotropy to the onset of surface and sub-surface damage [14]. Depending on the point of contact, we find friction coefficients differing by a factor of 4, i.e., $\mu \simeq 0.2$ or 0.8. Although this difference could be related to the anisotropy effect, we cannot rule out the possibility that different degrees of surface cleanliness cause this change in friction behavior [6].

CONCLUSION

In experiments on the nanotribology of diamond films, we have reported the incidence of intermittent motion on a nanometer scale, when sliding a diamond tip across a diamond film. The slips, $\approx$ 10-30 Å in size, occur instantaneously within the time constant of our electronics, 200 μs. Various factors, such as the friction-speed characteristic, the surface topography and a variation in frictional force due to varying sample conditions might cause the stick-slip motion. Depending on the point of sample contact, we observed friction coefficients of $\simeq$ 0.2 or $\simeq$ 0.8. This difference is due either to the anisotropy of diamond friction or to a variation of the surface condition. At a point of low friction, we derived friction coefficients of 0.26 and 0.16 for the static and dynamic friction, respectively. The decrease in friction coefficient with load can be attributed to a largely elastic response of the diamond surface.

Acknowledgements

This work was partially supported by the AFOSR under contract F49620-89-C-0068. S.R.C. thanks the Myron A. Bantrell trust for support through a Chaim Weizmann postdoctoral fellowship.

References

[1] current address: Lawrence Berkeley Laboratory, Center for Advanced Materials, Berkeley, CA, 94720.

[1] J.E. Field, (Editor), Properties of Diamond, Academic Press, London, 1979.
[2] R. Berman, (Editor), Physical Properties of Diamond, Clarendon Press, Oxford, 1965.
[3] M.S. Wong, R. Meilunas, T.P. Ong, R.P.H. Chang, Mat. Res. Soc. Symp. Proc. 140, 483 (1989).
[4] M.S. Wong, R. Meilunas, T.P. Ong, R.P.H. Chang, Appl. Phys. Lett. 54, 2006 (1989).
[5] S. Johanmir, D.E. Deckman, L.K. Ives, A. Feldman, E. Farabaugh, Wear 133, 73 (1989).
[6] F.P. Bowden, F.R.S., J.E. Young, Proc. Roy. Soc. A 208, 444 (1951).
[7] F.P. Bowden, F.R.S., A.E. Hanwell, Proc. Roy. Soc. A 295, 233 (1966).
[8] F.P. Bowden, F.R.S., C.A. Brookes, Proc. Roy. Soc. A 295, 244 (1966).
[9] M. Seal, Proc. Roy. Soc. A 248, 379 (1958).
[10] M. Seal, Phil. Mag. A 43, 587 (1981).
[11] M. Casey, J. Wilks, J. Phys. D Appl. Phys. 6, 1772 (1973).
[12] B. Samuels, J. Wilks, J. Mat. Sci. 23, 2846 (1988).
[13] D. Tabor, in "The Properties of Diamond", edited by J.E. Field, Academic Press, London, 1979.
[14] Y. Enomoto, D. Tabor, Proc. Roy. Soc. A 373, 405 (1981).
[15] G.Binnig, C.F. Quate, Ch. Gerber, Phys. Rev. Lett. 56, 930 (1986).
[16] S. R. Cohen, G. Neubauer, G. M. McClelland, to appear in J. Vac. Sci. Tech. (July/August 1990).
[17] G. Neubauer, S.R. Cohen, G.M. McClelland, D. Horne, C.M. Mate, to appear in Rev. Sci. Instr. (1990).
[18] J.C. Angus, C.C. Hayman, Science 241, 915 (1988).
[19] M. Buck, T.J. Chuang, J.H. Kaufman, H. Seki, to be published in MRS Fall Meeting Symposium Proceedings 162, (1990).
[20] S.V. Pepper, J. Vac. Sci. Tech. 20, 643 (1982).
[21] R. Erlandsson, G.M. McClelland, C.M. Mate, S. Chiang, J. Vac. Sci Tech. A 6, 266 (1988).
[22] Y. Martin, C.C. Williams, H.K. Wickramasinghe, J. Appl. Phys. 6., 4723 (1987).
[23] F.P. Bowden, D. Tabor, The Friction and Lubrication of Solids, Oxford University Press, New York, (1986).
[24] C.M. Mate, G.M. McClelland, R. Erlandsson, S. Chiang, Phys. Rev. Lett. 59, 1942 (1987).
[25] R. Erlandsson, G. Hadziioannou, C.M. Mate, G.M. McClelland, S. Chiang, J. Chem. Phys. 89, 5190 (1988).

ION BEAM ANNEALING OF VAPOR-DEPOSITED CARBON FILM

KAZUO HIGUCHI, SHOJI NODA, SUMIKO IRITANI, TOMOJI ISHIGURO AND OSAMI KAMIGAITO
TOYOTA Central R & D Labs., Inc., Nagakute-cho, Aichi-ken 480-11 JAPAN

ABSTRACT

The effects of ion implantation on microtexture of vapor-deposited carbon film were studied by Raman, XRD, TEM and sheet resistivity measurements. Growth of graphite-microcrystals in the film was found when the film was implanted at the temperature above about 500 K, while graphite-sheet in the as-deposited film was distorted when it was implanted at the temperature below 300 K. The critical temperature for the ion beam annealing was estimated to be about 350 K. Ion implantation also caused the increase of the adhesion strength of the carbon film to a substrate.

INTRODUCTION

Carbon film coating is thought to have potential applications in a variety of fields because of its excellent chemical and physical properties. But the poor adhesion to a substrate limits its application now. A vacuum-deposited carbon film has been reported to be in a large compressive stress[1], and the film tends to wrinkle when it is exposed in an ambient air.

High energy ion irradiation (ion implantation) to a thin film on a substrate induces many atom displacements in both the film and the substrate, and it may cause atom-mixing at the interface. The atom displacements may reduce any residual stress in the film. So, ion implantation to a thin film is expected to improve the adhesive strength of the film via atom-mixing at the interface as well as the relief of residual stress in the film. The atom displacements also result in either ordering or disordering of atom arrangement in implanted materials. For a given material, irradiation temperature is a crucial factor to determine whether the ordering occurs in the material or the disordering does. The ion-induced ordering is called ion beam annealing. Atom ordering, or crystallization usually occurs at lower temperature in ion beam annealing than in conventional thermal annealing[2].

Here, we study the effects of ion implantation on adhesion and microtexture of a vapor-deposited carbon film. Carbon has two crystalline structures of very different nature; diamond and graphite. As ion implantation is a non-equilibrium process, it is expected to result in unique modification of carbon.

Mat. Res. Soc. Symp. Proc. Vol. 188. ©1990 Materials Research Society

Diamond force microscope tips fabricated by chemical vapor deposition

G. J. Germann, G. M. McClelland, Y. Mitsuda,[a] M. Buck,[b] and H. Seki
IBM Research Division, Almaden Research Center, 650 Harry Road, San Jose, California 95120

(Received 6 April 1992; accepted for publication 7 June 1992)

A chemical vapor deposition method is described for fabricating force microscope cantilevers with single-crystal diamond tips. The $\simeq$1-μm-diam diamond tips have corner radii of 30 nm, and have been used to study diamond–diamond friction on well-characterized surfaces in UHV. The tip size and orientation can be determined by electron microscopy without altering the surface atomic structure.

I. INTRODUCTION

Atomic force microscopy (AFM) requires the use of sharp tips for imaging forces on the atomic scale.[1] However, sharp tips are often fragile, especially at higher loads, such as occur in indentation experiments.[2] Several groups have used tips made of diamond, the hardest substance known. Diamond tips have been formed by fracture[3] or by polishing,[4] and ion-impregnated conducting diamond tips have been developed for scanning tunneling microscopy.[5] Although a fractured diamond tip can probably be quite sharp, its geometry and surface chemistry are not well defined. In this paper we present a method for preparing diamond AFM tips by chemical vapor deposition (CVD).[6] These single-crystal tips have a well-defined crystal structure and can have quite sharp corners. Furthermore, their diamond surfaces, which are grown in a hydrogen-rich atmosphere, are hydrogen terminated. They therefore have a low surface energy, and should become contaminated less readily than other tip materials such as Si, SiO_2, or Si_3N_4.

Apart from its utility in AFM applications, CVD diamond film shows great promise for the construction of improved electronic devices.[7] Diamond can be made to be semiconducting and, in addition to its hardness, has very high thermal conductivity and a low coefficient of friction.[8,9] As manufacturing techniques become more advanced, its role in production of devices will become more prevalent. Because of this, an investigation of diamond on the nanometer scale is warranted. We report elsewhere on the use of diamond-tipped cantilevers to investigate diamond–diamond interactions on the atomic scale.[10] To address diamond's important tribological applications, these experiments probe the forces both perpendicular (load and topography) and parallel (friction) to the surface.

II. FABRICATION

Although we have chosen tungsten for the cantilever material for its stiffness and ease of etching, other cantilever materials are suitable for diamond tip deposition, including silicon, which is commonly used for AFM cantilevers, and as a test substrate for diamond CVD.

To begin forming the cantilevers, the end of a 1.0-cm length of 0.005-cm-diam tungsten wire is crimped into a 0.4-cm length of 0.040-cm o.d. stainless-steel tubing, which will become the base post of the cantilever. The wire is bent to an angle of 90° at a distance of 0.2 cm from the base and electrochemically etched with 8-V ac in a 10% aqueous KOH solution, until a $\simeq$200-μm length remains after the bend. The 0.2-cm length gives a force constant of $\simeq$30 N/m and a res nant frequency of $\simeq$5600 Hz. The etched end radii vary from $\simeq$0.1 to 2 μm, with a cone angle between $\simeq$10° and 25°.

A diamond nucleation site is introduced at the tip of the W wire to facilitate diamond growth. While viewing under an optical microscope, a diamond abrasive block (General Electric) mounted on a micropositioning stage is approached to the W tip. The block is pressed to the tip for 1 s at $\simeq 2\times10^{-4}$N, a force monitored by the deflection of a weak wire spring on which the cantilever holder is mounted. Significantly less force than this does not introduce a nucleation site on the tip (no diamond growth), while much greater forces cause multiple nucleation sites, resulting in multiple diamond crystals and poorer tips. Evidently the nuclei deposited from the block are no bigger than $\simeq$10 nm, because they could not be observed by scanning electron microscopy (SEM).

Diamonds are grown at these nucleation sites in the CVD apparatus diagrammed in Fig. 1. The wire cantilever tips are mounted $\simeq$3 mm from a Ta filament consisting of 0.25-mm Ta wire wrapped in a 4-mm-diam coil $\simeq$13-mm long. The apparatus is evacuated and CH_4 and H_2 are flowed over the filament toward the cantilevers at rates of 0.3 and 60 sccm, respectively. The flows are regulated by mass flow controllers, and a vacuum pump keeps the pressure constant at 40 Torr. These conditions provide flow stability and concentration uniformity during CVD. Slower flow rates reduce the probability of forming single crystals on the tip and increase the probability of forming less desirable multiple crystals.

Monitoring the temperature by an optical pyrometer (Wahl DHS-52), the Ta filament is heated to $\simeq$2100 °C to effect dissociation of the CH_4 and H_2 and to heat the cantilever tips to a temperature appropriate for diamond deposition, $\simeq$800 °C. This temperature was not measured directly, but under these conditions the temperature of the assembly which holds the cantilevers, as measured by a thermocouple, is 500 °C. After CVD has continued for 1 h, the filament and the CH_4 flow are stopped and the canti-

[a]Present address: Institute of Industrial Science, The University of Tokyo, 7-22-1 Roppongi, Minato-ku, Tokyo 106, Japan.
[b]Present address: U. of Heidelberg, Institute of Applied Physical Chemistry, D-6900 Heidelberg, Germany.

 0034-6748/92/094053-03$02.00 © 1992 American Institute of Physics

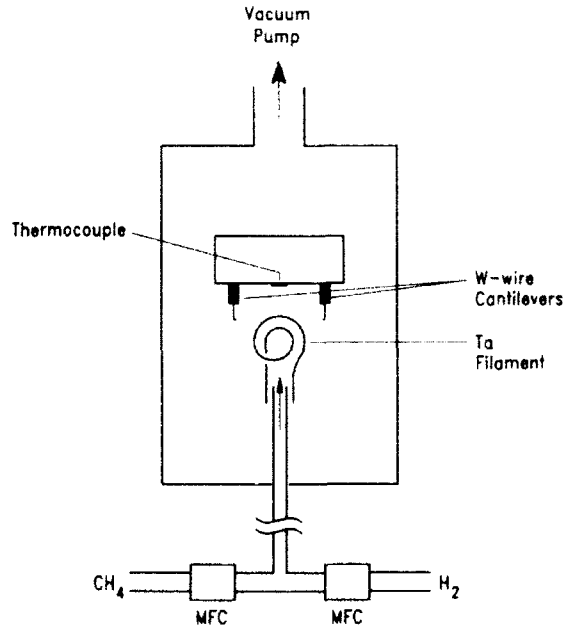

FIG. 1. Schematic of chemical vapor deposition (CVD) apparatus used to deposit diamond on AFM cantilevers. The H_2 and CH_4 flow rates are regulated by mass flow controllers (MFC).

levers are allowed to cool in flowing H_2. This process almost always produces a single $\simeq 1$-μm-diam diamond crystal or aggregate of several such crystals at the very tip of the cantilever. Generally, fewer than 10 diamonds are seen on other regions of the cantilever which have not been intentionally nucleated. Since the diamond surfaces are grown from a gas rich in H atoms, their surfaces are believed to be terminated with hydrogen.[11]

III. CHARACTERIZATION AND USE

While using a SEM to characterize the diamond tip, it is important to avoid damage by the 10-keV electron beam. We minimize damage by using a frame grabber to capture a low magnification, 6000× SEM image of the AFM tip in 5 s with a beam current of 0.02 nA. To estimate the beam damage, we note that for polyethylene, a 10-keV electron will inflict on average one damage site every 300 Å along its path.[12] If the probability of damage to a diamond surface, with its single C—C and C—H bonds, is similar to that for polyethylene, the instance of damage to our diamond tip in the SEM would be 0.3% per $(3.5\ \text{Å})^3$ unit cell. We conclude that the SEM imaging does not significantly alter the surface bonding of the CVD deposited tip.

The orientation of the crystal facets of the diamond tip on the cantilever cannot be controlled. The "ideal" AFM tip crystal possesses a sharp corner pointing along the W tip axis. We have found that a suitable tip, one with a sharp corner oriented outward from the AFM cantilever, can be obtained on W once in about 20 attempts. To facilitate the production process, we deposited diamond tips onto 10 nucleated tungsten wire tips simultaneously. Originally we attempted to grow diamonds on 25 tips simultaneously, by mounting the cantilevers on a square 5×5 array spaced by

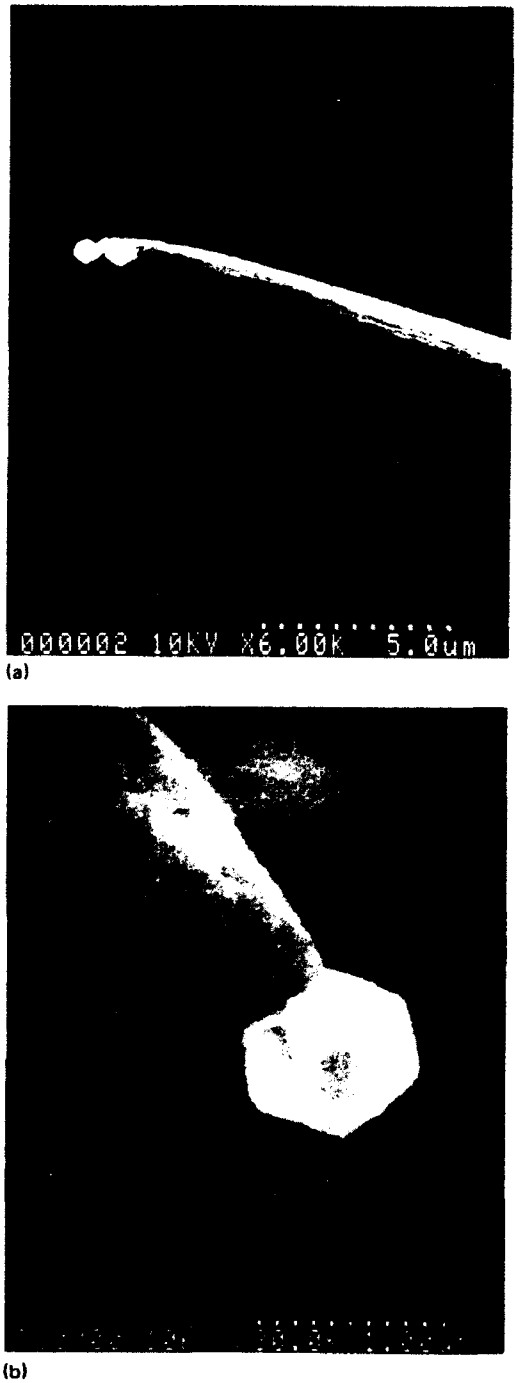

(a)

(b)

FIG. 2. Scanning electron micrographs of diamond AFM tips. (a) Low-resolution image after experiments involving 3×10^{-7} N loads. (b) High-resolution micrograph of another tip. The outward pointing corner, which has an estimated radius of $\simeq 300$ Å, is used for imaging.

0.25 cm. We found that only those 10 cantilevers (the two outermost rows of 5) positioned as shown in Fig. 1 grew acceptable diamonds. This was probably because the center cantilever deposition positions, being closest to the Ta filament, were too hot to support deposition.

Two sample cantilevers are shown in Fig. 2. High magnification, >6000×, photos are taken after rather than before the AFM experiments, in order to avoid damage which may result from the high electron intensity involved.

FIG. 3. AFM friction image (57.9×12.5 Å) of a hydrogen-terminated single-crystal (100) diamond surface taken using a diamond-tipped cantilever. The gray scale ranges from 0 (black) to 1.5×10^{-8} N (white). It represents the deflection of the cantilever parallel to the surface as the tip is scanned from left to right and is a measure of the forces along the scan direction.

From these SEM images we find tip radii of $\simeq$300 Å. The diamond tips form in a variety of shapes and sizes ranging from 0.1 to 2 μm, and exhibit almost exclusively {100} and {111} planes. A typical corner used for AFM imaging is a four-sided pyramid, with two opposite {100} planes at an included angle of 90°, and two {111} planes at an angle of 109.5°. The sharpest corners are cube corners formed by {100} plane junctions.

The diamond-tipped cantilever is introduced into the vacuum AFM chamber through a sample transfer/airlock system, and the cantilever is cleaned by heating in a Ta oven to 500 °C, under vacuum, for 30 min. This heating process is sufficient to clean the hydrogen terminated diamond surface of physisorbed contaminants.[13,14] After cleaning, the cantilever is mounted in the AFM and its motion is detected with a bidirectional fiber optic interferometer. Details of the basic experimental apparatus,[15] and the dual fiber detection scheme[16] are described elsewhere.

The normal force between the diamond tips and (111) or (100) diamond surfaces exhibits van der Waal's attractive forces that are appropriate for the estimated tip radii.[10] Measuring the maximum attractive force from the curve of normal force versus separation, we find 7.5×10^{-9} N. The attractive dispersion force[17] between a sphere of radius R a distance D from a flat is $F = -AR/6D^2$, where A is the Hamaker constant, estimated from the diamond optical constants to be 3.5×10^{-19} J. Using an estimated tip radius of 30 nm, and the observed attractive force, this gives 0.47 nm for the effective tip from the sample at its potential minimum value, considering the effect of surface

The diamond–tungsten adhesion is surprisingly strong, and we have never dislodged the tip from its nucleation site on the tip, even at loads up to 3×10^{-5} N. By SEM we observe no evidence of wear after weeks of AFM experiments and no progressive change in the attractive approach curve for our diamond tip–diamond surface experiments during this period.

To illustrate the use of the diamond tip, we show an image in Fig. 3 of the friction force between a diamond tip and a single crystal diamond (100) surface.[10] The image clearly shows structure in the form of rows along a [210] direction of the bulk diamond lattice, spaced by 2.3 Å. These are consistent with a 2×1 monohydrogen terminated reconstructed surface.[13] We believe that averaging over an asymmetric AFM tip prevents the observation of structure perpendicular to the rows shown in the figure. The gray scale in Fig. 3 represents not a topographic image but rather the force parallel to the surface, reflecting the friction and dynamics along the raster scan direction.

In summary, a straightforward method of fabricating diamond-tipped AFM cantilevers has been developed. This CVD method produces sharp, hard, and inert tips, which are found to be mechanically robust and wear-resistant even at high load. We have used the cantilevers to probe the hydrogen-terminated (100) surface of a single-crystal diamond, obtaining friction images with sub-nm resolution.

Note added in proof: Visser *et al.* have also recently described a CVD technique for fabricating semiconducting diamond AFM and STM tips. [E. P. Visser, J. W. Gerritson, W. J. P. van Enckevort, and H. van Kemp, Appl. Phys. Lett. (in press)].

ACKNOWLEDGMENTS

We are grateful to V. S. Smentkowski and J. T. Yates, Jr. for help with the early experiments, G. D. Kubiak and J. Pacansky for helpful discussions, and J. Vazquez for obtaining the electron micrographs. This work was partially supported by Office of Naval Research Contract N00014-88-C-0419 and Air Force Office of Scientific Research Contract F49620-89-C-0068.

[1] For a review, see D. Rugar and P. Hansma, Phys. Today **43**, 23 (1990).
[2] P. J. Blau and B. R. Lawn, eds., *Microindentation Techniques in Materials Science and Engineering* (ASTM, Philadelphia, 1985).
[3] O. Marti, B. Drake, and P. K. Hansma, Appl. Phys. Lett. **51**, 484 (1987); T. R. Albrecht and C. F. Quate, J. Appl. Phys. **62**, 2599 (1987); E. Meyer, H. Heinzelmann, P. Grütter, Th. Jung, Th. Weisskopf, H.-R. Hidber, R. Lapka, H. Rudin, and H.-J. Güntherodt, J. Microscopy **152**, 269 (1988); G. Neubauer, S. R. Cohen, G. M. McClelland, and H. Seki, in *Thin Films: Stresses and Mechanical Properties II*, edited by M. F. Doerner, W. C. Oliver, G. Pharr, and F. R. Brotzen (Materials Research Society, Pittsburgh, 1990), MRS Symp. Proc. **188**.
[4] T. Miyamoto, R. Kaneko, and S. Miyake, J. Vac. Sci. Technol. B **9**, 1336 (1991).
[5] R. Kaneko and S. Oguchi, Jpn. J. Appl. Phys. **29**, 1854 (1990).
[6] R. C. Devries, Ann. Rev. Mater. Sci. **17**, 161 (1987); B. V. Spitsyn, L. L. Bouilov, and B. V. Derjaguin, Prog. Crystal Growth Charact. **17**, 79 (1988).
[7] A. T. Collins, Semicond. Sci. Technol. **4**, 605 (1989); K. Shenai and B. J. Baliga, Proc. Inter. Symp. on Diamond and Diamond-Like Films (Electrochemical Society, NJ, 1989).
[8] J. E. Field, ed., *The Properties of Diamond* (Academic, London, 1979).
[9] B. Samuels and J. Wilks, J. Mater. Sci. **23**, 2846 (1988), and references therein.
[10] G. J. Germann, G. Neubauer, S. R. Cohen, G. M. McClelland, and H. Seki (to be published).
[11] M. Frenklach and H. Wang, Phys. Rev. B **43**, 1520 (1991); P. Deak, J. Giber, and H. Oechsner, Surf. Sci. **250**, 287 (1991).
[12] T. Okada and L. Mandelkern, J. Polym. Sci. A-2 **5**, 239 (1967); L. Mandelkern, in *The Radiation Chemistry of Macromolecules*, edited by M. Dole (Academic, New York, 1972), Vol. 1, p. 287.
[13] A. V. Hamza, G. D. Kubiak, and R. H. Stulen, Surf. Sci. **237**, 35 (1990).
[14] B. B. Pate, Surf. Sci. **165**, 83 (1986).
[15] G. Neubauer, S. R. Cohen, G. M. McClelland, D. Horne, and C. M. Mate, Rev. Sci. Instrum. **61**, 2296 (1990).
[16] D. Rugar, H. J. Mamin, and P. Guenther, Appl. Phys. Lett. **52**, 2588 (1989).
[17] J. N. Israelachvili, *Intermolecular and Surface Forces* (Academic, London, 1985).

Atomic scale friction of a diamond tip on diamond (100) and (111) surfaces

Geoffrey J. Germann, Sidney R. Cohen,[a] Gabi Neubauer,[b] Gary M. McClelland,[c] and Hajime Seki
IBM Research Division, Almaden Research Center, 650 Harry Road, San Jose, California 95120

D. Coulman
E. I. Dupont, Experimental Station, P. O. Box 80326, Wilmington, Delaware 19880-0356

(Received 1 June 1992; accepted for publication 22 September 1992)

The friction of a clean diamond tip on diamond (111) and (100) surfaces is studied using an ultrahigh vacuum force microscope that simultaneously measures forces parallel and perpendicular to the surface. The 30 nm radius diamond tip is fabricated by chemical vapor deposition. The attractive normal force curve between the tip and surface agrees well with calculated dispersion interactions. The frictional force exhibits periodic features, which on the (100) surface are tentatively associated with a 2×1 reconstructed surface convoluted over an asymmetric tip shape. The (111) surface shows features that cannot be simply related to the surface structure. As the tip is scanned back and forth along a line, the same features are observed in each direction, but offset, suggesting the presence of a conservative force independent of the direction of motion as well as a nonconservative force. The friction is approximately $\simeq 3\times10^{-9}$ N independent of loads up to 1×10^{-7} N.

INTRODUCTION

Interfacial solid-solid sliding friction is customarily associated with wear, but atomic force microscope (AFM)[1] and surface force apparatus[2] experiments show that sliding without wear is feasible, and AFMs have directly measured atomic scale frictional force variations.[3–7] With some exceptions,[8] little attention has been given to the tip morphology or composition, and, as discussed by Cohen,[9] many previous measurements of tip-surface forces have probably been affected by interfacial contamination. Here we present a study of atomic level friction between (100) and (111) diamond surfaces and a diamond tip in ultrahigh vacuum (UHV). This is the first observation of the atomic scale structure of friction in UHV, although several vacuum studies, including our work on films formed by chemical vapor deposition (CVD),[10] have probed a somewhat larger scale.[7,10,11] Because of its unique hardness, diamond is an ideal material on which to observe wearless friction. We observe variations in the lateral force associated with the diamond crystal lattice, and find that the frictional force varies little with load. The lateral tip-surface force shows a strong conservative component, which can be as large or larger than the nonconservative frictional component that dissipates energy.

EXPERIMENT

To probe frictional forces, several bidirectional AFMs have been designed that measure both lateral (frictional) and normal (loading) forces. These designs have used capacitance measurement,[12] laser beam deflection,[5,7] and optical fiber interferometry.[13,14] If fiber interferometer is used to measure the lateral force directly,[14] the fiber must be positioned very close and parallel to the surface. Our design (Fig. 1) avoids this problem by symmetrically positioning two fibers 90° apart in a plane perpendicular to the sample and the cantilever. From the normalized sum and difference of these two signals, the deflection normal (load) and parallel (friction) to the surface is determined. Forming these linear combinations has no effect on the noise of the deflection measurement. Because variations in laser diode power are subtracted out,[15] the 0.15 Å (rms) noise measured over a scan line was caused mainly by wavelength variation.

All experiments used the diamond tip displayed in Fig. 2(a). As described elsewhere,[16] the tip was grown onto the end of the tungsten cantilever (force constant, 30 N/m) by CVD. Before the AFM measurements, it was examined at low magnification by scanning electron microscopy (SEM), using low electron exposure to insure negligible alteration of the surface bonding.[16] By examining high-resolution SEMs obtained from several viewing angles after the AFM measurements, the tip was found to be formed from two {100} and two {111} planes [Fig. 2(b)], and oriented so that the sample surface normal was parallel to the ⟨110⟩ direction of the tip. The flat single-crystal samples were polished with diamond grit in olive oil, rinsed in several solvents, and blown dry. After being placed in the ultrahigh vacuum (UHV) chamber, both surfaces and tip were raised to 500 °C for 30 min and returned to 25 °C, a process known to leave clean ordered hydrogen-terminated surfaces.[17,18] The vacuum was limited by outgassing of the fiber cladding to 5×10^{-9} Torr.

RESULTS

The tip-surface force normal to the surface shows a broader and deeper attractive well upon retraction than during approach (Fig. 3). As demonstrated by molecular

[a] Present address: Department of Chemical Physics, Weizmann Institute of Science, Rehovot 76200, Israel.
[b] Present address: Intel Corp. P. O. Box 58119, Santa Clara, CA 95052.
[c] To whom correspondence should be addressed.

 0021-8979/93/010163-05$06.00 © 1993 American Institute of Physics

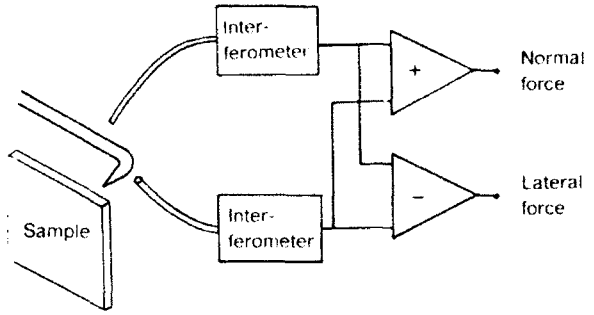

FIG. 1. Dual fiber interferometer for measuring lever deflection normal (load) and perpendicular (friction) to the surface. The two interferometers are optically independent.

dynamics (MD) calculations,[19] no plastic deformation or chemical processes are expected at these loads for hydrogen-terminated diamond surfaces. The hysteresis thus indicates the presence of physisorbed molecules or flexible groups chemically bound to the sample or tip. For a sphere of radius R a distance D from a flat, the attractive dispersion force is approximately $F=-AR/6D^2$, where A is the Hamaker constant, estimated from the diamond optical constants to be 3.5×10^{-19} J. This function is plotted in Fig. 3(a) for the 30 nm tip radius estimated by SEM. The observed maximum attractive force of 7.5×10^{-9} N gives 0.48 nm for the effective distance of closest approach, a reasonable value considering probable roughness of the tip. Comparing Figs. 3(a) and 3(b), the approach curve varied little over the weeks required to do the experiment, suggesting little tip wear.

Hertz showed that the radius a of the elastic contact of a spherical tip of radius R with a flat is $[3PR(1-\nu^2)/2E]^{1/3}$, where P is the load and E and ν are the Young's modulus and Poisson's ratio.[20] Using $R=30$ nm, the contact radius a is 1.6 nm at the largest 10^{-7} N loads used, giving an elastic deformation of each of the two solids of $a^2/2R=0.042$ nm, and MD simulations indicate that the additional deformation at the interface is well below 0.1 nm.[19] Surface roughness probably leads to a smaller contact area and larger deformation.

An image [Fig. 4(b)] of the frictional forces on the (100) surface was obtained at 1.5×10^{-8} N load and a scan rate of 2.3 nm/s while oscillating the sample 0.15 nm peak-to-peak (p-p) at 1 kHz along the scan direction to increase contrast. The image shows rows along the ⟨021⟩ direction spaced by a single lattice constant along the ⟨001⟩ direction, a pattern consistent with a 2×1 reconstruction. The lack of structure along ⟨021⟩ may be due to averaging over the asymmetrical contact area of the tip, whose shape and orientation is shown in Fig. 4(a). Although the 2×1 reconstruction was previously observed only at much higher temperatures than we used, the measured Arrhenius parameters for the associated hydrogen desorption[18] predict that the reconstruction would go 5% toward completion during our 30 min heating. Considering possible errors in measuring the temperature of the diamond surface, and deviation from the strict Arrhenius relation over the large

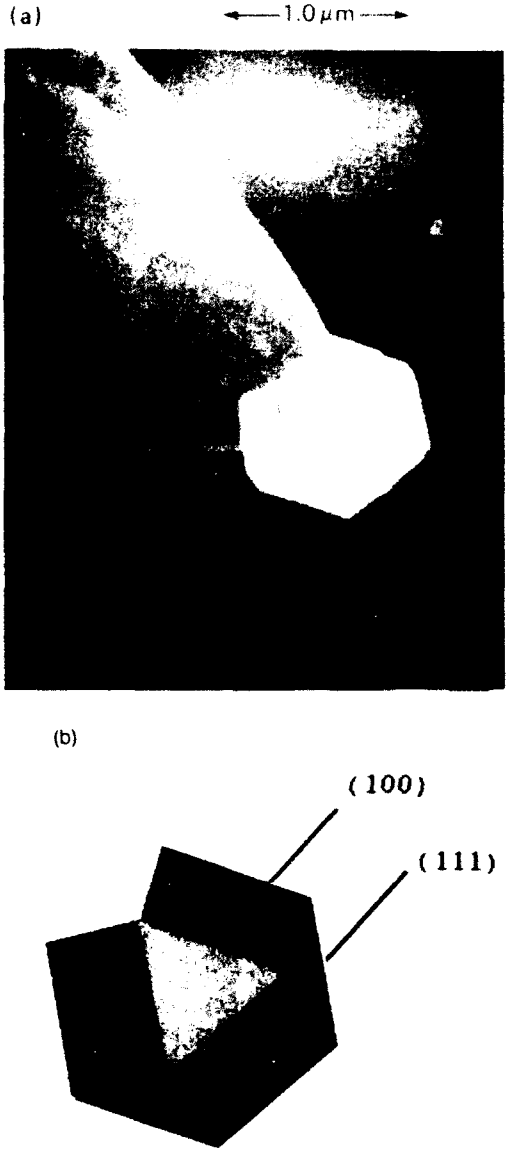

FIG. 2. (a) Scanning electron micrograph of the diamond tip grown on the end of an etched tungsten tip. The corner pointing outward along the wire axis was used for imaging. (b) Geometric model of the tip.

temperature range extrapolated, it is possible that reconstruction could occur under our heating conditions. Friction on the (111) surface at 1.5×10^{-8} N load shows less well-defined rows [Fig. 4(c)], bearing no clear relation to the diamond (111) lattice. The approximate parallelism of the predominant features on the (100) and (111) surfaces suggests that the tip geometry may play a role in emphasizing this direction. Simultaneous measurement of the normal deflection of the lever shows no atomic level structure within the 0.07 nm p-p noise, but on the (100) surface we observed 0.3–1.5 nm high striations approximately 5 nm apart. That no topographic features narrower than 2 nm were observed may reflect the size of the diamond tip. Recently, atomic-level structure of CVD diamond films has been observed by STM[21] and AFM.[22]

The "friction loops"[3] of Fig. 5 (without small amplitude oscillation) on the (100) surface are obtained by

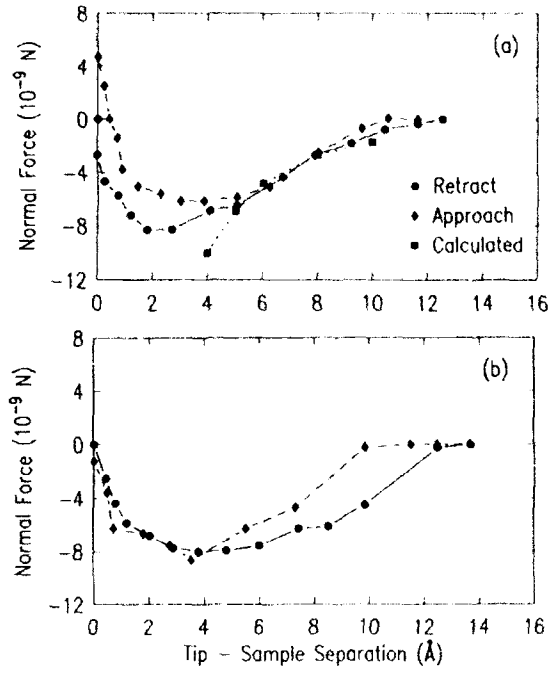

FIG. 3. Normal force between the tip and the surface as the sample is first approached and then withdrawn from the tip. Positive forces are repulsive. Curves (a) and (b) were recorded 40 days apart.

scanning the sample alternately back and forth along the same path in opposite directions. The sample position is subtracted from the measured tip position to generate the abscissae of Fig. 5. Measuring the force parallel to the scan direction [Fig. 5(a)], the loop shows very similar features along opposite scanning directions, but the force offset between the two directions reveals a net dissipation of mechanical energy. The diagonal straight lines in the loop indicate "slipping" of the lever, which occurs when the derivative of the tip-surface force changes from being greater than to being less than the lever force constant.[3] The shape of the loop, which changes little during consecutive scans, suggests that the lateral force is the sum of a position-dependent conservative part, independent of sliding direction, and a position-independent dissipative force, whose sign reverses with sliding direction.

When the surface is scanned at an angle 45° with respect to the layer axis [Fig. 5(b)], approximately parallel to the features of Fig. 4(a), very little hystersis is observed. In fact, during a scan in a particular direction, the lever is deflected laterally to both positive and negative sides of its equilibrium position. The decrease in hysteresis can be partially attributed to the fact that the sliding direction is 45° with respect to the force sensing direction. Also, for sliding

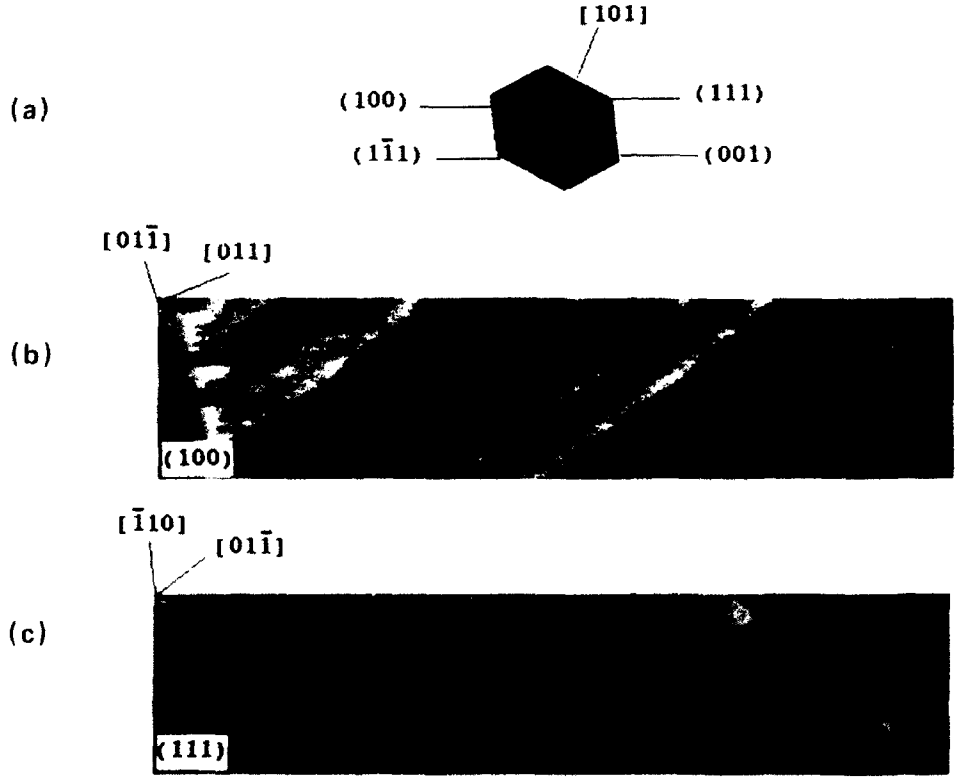

FIG. 4. (a) Schematic of the tip, viewed as if looking through the tip along the surface normal, with the proper experimental orientation relative to the grey scale images. (b) 5.79×1.25 nm image of the frictional force between the diamond tip and a (100) surface. The gray scale, ranging from 0 to 1.1×10^{-8} N, represents the deflection of the cantilever parallel to the scan direction as the tip is scanned from left to right. (c) Friction on the (111) surface, area 5.8×1.25 nm, grey scale range 0–1.1×10^{-8} N. The sample orientation is determined by x-ray diffraction.

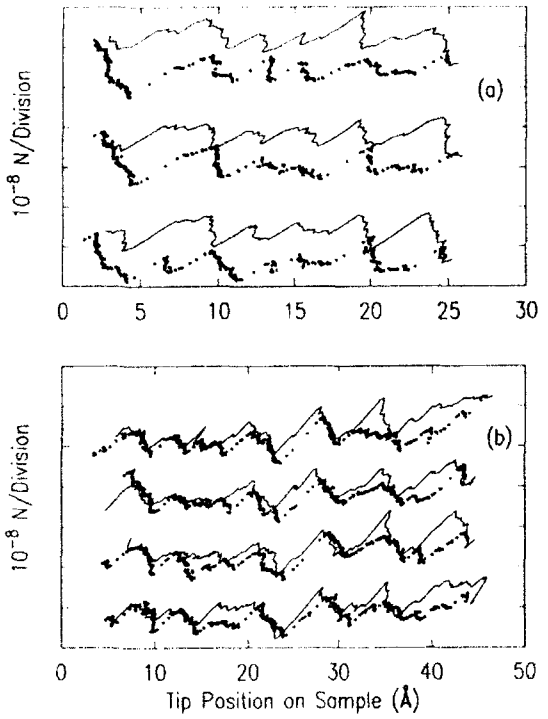

FIG. 5. Lateral tip-surface force on the (100) surface as the sample is moved back and forth along a single line. Several sequential loops are shown, offset vertically. The solid trace represents the right-to-left scan, the data points, left-to-right. Positive (up) forces oppose right-to-left motion. (a) (100) surface with zero net load, scanning in the same direction as in Fig. 4(b), along the force-sensing direction. (b) (100) surface at 1.5×10^{-8} N load, scanning in the direction rotated $\pi/4$ counterclockwise from the scan direction of Fig. 4(b). The force component is measured along the scan direction of Fig. 4(b).

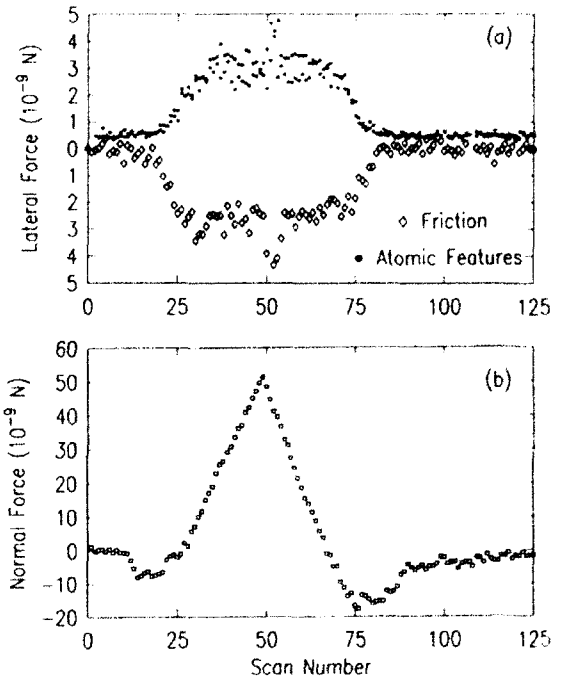

FIG. 6. Forces measured over friction loops as the (111) surface is first advanced toward, then withdrawn from the tip while being scanned back and forth. The horizontal axis is the sequential scan number. (a) Average friction force (note inverted vertical scale) and size of force features. (b) Average force normal to the surface (load).

in this direction, the lever cannot become "stuck" on the surface because there is a component of the sample motion along the axis of the cantilever, a direction in which it is not compliant. These results emphasize the existence of a conservative force parallel to the surface, dependent on position but unrelated to the sliding process itself.

The average friction, defined as half the difference between the average lateral force along the scanning direction in the two directions of the friction loop, is plotted versus load in Fig. 6. As the surface is brought into contact with the tip, friction increases suddenly at the attractive force maximum, but it changes little in the repulsive regime, as the load varies between 0 and 1×10^{-7} N. The magnitude of the rms lateral force deviation from its average along a single scan direction (labelled atomic features in Fig. 6), which we associate with the conservative potential, also depend little on load.

Although the qualitative frictional properties described were observed repeatedly, variations of up to a factor of 2 in frictional forces were observed from day to day on different areas of the surface. Within this range, the average frictional forces observed on the (100) and (111) surfaces were the same. The dependence of lateral force on sliding direction was probed by comparing the sliding in the two directions 45° with respect to the lever axis [as in Fig. 5(b)] at a particular place on the surface. The average frictional hysteresis was the same within 10%.

DISCUSSION

The minimal load dependence of the frictional force observed here is in sharp contrast to macroscopic systems, in which friction increases linearly as the load increases, causing more asperities to contact. Our experiments correspond more to the contact of a single asperity. For a single "Hertzian" elastic contact of a sphere on a plane, the contact area increases as $P^{2/3}$, a stronger variation than we observe. If the lateral force were due to the slope of the local topography, the conservative lateral force would be proportional to load by a proportionality constant equal to the local slope of the surface. Even for atomically flat surfaces, the shear strength of the interface sometimes depends linearly on load.[23] Since none of these models are consistent with our results, it may be that the load is carried by a different region of the tip than that which determines the lateral forces. At the highest loads, the ratio of frictional force to load is 0.05, and the friction is essentially independent of load, so that the "differential friction coefficient" is essentially zero. It has been predicted that friction between strong smooth solids interacting by nonchemically bound forces should disappear unless the solids are commensurate,[24] even at zero temperature. Recent MD calculations of diamond friction show zero friction along a particular sliding direction.[25] Thermally activated processes should act to reduce friction.

The largest loads we used correspond to a contact loading stress of 20 GPa, a value also attained in experiments using a much larger 60 μm radius tip.[26] At this stress, the ratio of friction to load is similar to the value we measure, but in the larger scale experiments, the friction increases strongly with load, in contrast to our observations.

Concerning the friction of diamond, there is an extensive literature, which has been summarized by Samuels and Wilks.[26] They speculate that energy dissipation during friction occurs by two mechanisms. In the "ratchet mechanism," energy is released by the sudden transfer of the loading force from one asperity to another. In the elastic mechanism, the released energy comes from elastic strain in an asperity. The sudden slips we observe could be considered a type of ratchet mechanism, in which the lever itself supplies a lateral loading. Yet the lateral force shows hysteresis even where the tip is not sticking. In the elastic asperity mechanism, for a sudden slip to occur between neighboring minima of the interfacial potential, the total lateral distortion of the asperities would have to be at least 0.1 nm, the minimum (atomic) scale over which the interfacial potential varies. Using the fact that the lateral stiffness[20] of a contact of radius a is to a good approximation aE, for the typical observed lateral force of 10^{-8} N, the contact would then need to be less than 0.1 nm in radius, too small to be considered an asperity. Thus, the deflection of individual bonds is involved in the friction. For example the bending potential of a C—C—C bond is weak enough that a 0.1 nm deflection can be attained with a force of 4×10^{-9} N. From these considerations, pendant groups on the surface, which act to decrease the effective force constant for surface atoms, may enhance friction.[24]

ACKNOWLEDGMENTS

We thank V. Smentkowski and J. T. Yates, Jr. for encouraging our interest in diamond friction and for help with our early experiments. B. A. Hoenig assisted with computer programming. We enjoyed helpful discussions with G. D. Kubiak and J. A. Harrison. S. R. C. thanks the Myron A. Bantrell Trust for a Chaim Weizmann Postdoctoral Fellowship. This work was partially supported by the Office of Naval Research contract N00014-88-C-0419 and the Air Force Office of Scientific Research contract F49620-89-C-0068.

[1] For a review, see D. Rugar and P. Hansma, Phys. Today **43**, 23 (1990).
[2] See, for example, M. L. Gee, P. M. McGuiggan, J. N. Israelachvili, and A. M. Homola, J. Chem. Phys. **93**, 1895 (1990); S. Granick, Science **283**, 1374 (1991).
[3] C. M. Mate, G. M. McClelland, R. Erlandsson, and S. Chiang, Phys. Rev. Lett. **59**, 1942 (1987).
[4] R. Erlandsson, G. Hadziioannou, C. M. Mate, G. M. McClelland, and S. Chiang, J. Chem. Phys. **89**, 5190 (1988); E. Meyer, R. Overney, L. Howald, D. Brodbeck, R. Lüthi, and H.-J. Güntherodt, in *Fundamentals of Friction*, edited by I. Singer and H. Pollock (Kluwer, Dordrecht) (in press).
[5] O. Marti, J. Colchero, and J. Mlynek, Nanotechnol. **1**, 141 (1990).
[6] S. R. Cohen, G. Neubauer, and G. M. McClelland, J. Vac. Sci. Technol. A **8**, 3449 (1990).
[7] G. Meyer and N. M. Amer, Appl. Phys. Lett. **57**, 2089 (1990).
[8] Q. Guo, J. D. J. Ross, and H. M. Pollock, MRS Symp Proc. **140**, 51 (1989); M. D. Pashley, J. B. Pethica, and D. Tabor, Wear **100**, 7 (1984); D. Maugis and H. M. Pollock, Acta Metallurg. **32**, 1323 (1984).
[9] S. R. Cohen, Ultramicroscopy **42**, 66 (1992).
[10] G. Neubauer, S. R. Cohen, G. M. McClelland, and H. Seki, in *Thin Films: Stresses and Mechanical Properties II*, edited by M. F. Doerner, W. C. Oliver, G. Pharr, and F. R. Brotzen (Materials Research Society, Pittsburgh, 1990), pp. 219–224.
[11] G. Neubauer, S. R. Cohen, and G. M. McClelland, in *Interfaces Between Metals, Polymers, and Ceramics*, edited by B. M. DeKoven, A. J. Gellman, and R. Rosenberg (Materials Research Society, Pittsburgh, 1989), p. 307.
[12] G. Neubauer, S. R. Cohen, G. M. McClelland, D. E. Horn, C. M. Mate, and C. M. Mate, Rev. Sci. Instrum. **61**, 2296 (1990).
[13] G. M. McClelland and J. N. Glosli, in *Fundamentals of Friction*, edited by H. M. Pollock and I. L. Singer (Kluwer, Dordrecht) (in press).
[14] C. M. Mate, Phys. Rev. Lett. **68**, 3323 (1992).
[15] D. Rugar, H. J. Mamin, and P. Günther, Appl. Phys. Lett. **52**, 2588 (1989).
[16] G. J. Germann, G. M. McClelland, Y. Mitsuda, M. Buck, and H. Seki, Rev. Sci. Instrum. **63**, 4053 (1992).
[17] B. B. Pate, Surf. Sci. **165**, 83 (1986).
[18] A. V. Hamza, G. D. Kubiak, and R. H. Stulen, Surf. Sci. **237**, 35 (1990).
[19] J. A. Harrison, D. W. Brenner, C. T. White, and R. J. Colton, Thin Solid Films **206**, 213 (1991); J. A. Harrison, C. T. White, R. J. Colton, and D. W. Brenner, Surf. Sci. **271**, 57 (1992).
[20] K. L. Johnson, *Contact Mechanics* (Cambridge University Press, Cambridge, 1985).
[21] T. Tsuno, T. Imai, Y. Nishibayashi, K. Hamada, and N. Fujimori, Jpn. J. Appl. Phys. **30**, 1063 (1991).
[22] L. F. Sutcu, M. S. Thompson, C. J. Chu, R. H. Hauge, J. L. Margrave, and M. P. D'Evelyn, Appl. Phys. Lett. **60**, 1685 (1992).
[23] B. J. Briscoe and D. C. B. Evans, Proc. R. Soc. London A **380**, 389 (1982).
[24] J. B. Sokoloff, Phys. Rev. B **42**, 760 (199); G. M. McClelland, in *Adhesion and Friction*, edited by M. Grunze and H. J. Kreuzer, Springer Series in Surface Science 17 (Springer, Berlin, 1989), p. 1; M. Hirano, K. Shinjo, R. Kaneko, and Y. Murata, Phys. Rev. Lett. **67**, 2642 (1991).
[25] J. A. Harrison, C. T. White, R. J. Colton, and D. W. Brenner, Phys. Rev. B **46** (1992) (in press).
[26] B. Samuels and J. Wilks, J. Mater. Sci. **23**, 2846 (1988).

RJ 9215 (81523) February 9, 1993
Surface Science

Research Report

OBSERVING THE MOTION OF A SINGLE ADSORBED ATOM WITH PICOSECOND AND SUB-NANOMETER RESOLUTION

H. Heinzelmann
F. Watanabe
G. McClelland

IBM Research Division
Almaden Research Center
650 Harry Road
San Jose, California 95120-6099

LIMITED DISTRIBUTION NOTICE

This report has been submitted for publication outside of IBM and will probably be copyrighted if accepted for publication. It has been issued as a Research Report for early dissemination of its contents. In view of the transfer of copyright to the outside publisher, its distribution outside of IBM prior to publication should be limited to peer communications and specific requests. After outside publication, requests should be filled only by reprints or legally obtained copies of the article (e.g., payment of royalties).

Research Division

Yorktown Heights, New York • San Jose, California • Zurich, Switzerland

RJ 9215 (81523) Februry 9, 1993
Surface Science

Observing the Motion of a Single Adsorbed Atom with Picosecond and Sub-nanometer Resolution

Harry Heinzelman†
Fumiya Watanabe
Gary M. McClelland‡

IBM Research Division
Almaden Research Center
650 Harry Road
San Jose, California 95120-6099

ABSTRACT

A new method is described for recording the motion of a single adsorbed atom or molecule in real time, with an ultimate achievable resolution of 10^{-14} s. The time dependence of electron field emission through an atom adsorbed on a metal tip is measured by focussing the electrons into a beam, which is swept across a detector screen. Simultaneous temporal and one-dimensional spatial resolution of the dynamics is possible. The motion of single Cs atoms between sites on atomically characterized W(111) tips is observed at 2 ps resolution.

†Current address;
Institute of Physics
University of Basel
4056 Basel
Switzerland
‡ To whom correspondence should be addressed

The physical and chemical properties of matter are determined by atomic motion, which occurs on the length scale of Ångstroms and on the 10^{-14} - 10^{-12} s time scale of vibration. Until recently, temporal information on this scale has been deduced only indirectly from scattering experiments or from spectral data in the frequency domain. Pump-probe laser techniques[1,2] have now been applied to large ensembles of molecules to achieve temporal resolution good enough to resolve molecular vibrations in stable and reacting molecules,[1] and time-resolved electron diffraction techniques have achieved somewhat poorer resolution.[3] Optical techniques are generally incapable of continuously observing the motion of single atoms and molecules on picosecond and shorter time scales, because they are insufficiently sensitive, and because the optical probes transitions drastically perturb the motion by changing the electronic state. On a much slower microsecond time scale, scanning tunneling microscopy[4] (STM) and field emission microscopy,[5,6,7] which can also be applied to thermal ensembles,[8] have been used. The jumping of single atoms can be traced by field ion microscopy (FIM), but with resolution of only $\approx$ 1 s.[9] STM has been combined with pump-probe laser techniques to monitor electronic relaxation with sub-nanometer resolution,[10] and an STM switch based on the motion of a single atom has been demonstrated.[11]

We have developed a method for continuously observing the motion of single adsorbed atoms or molecules by recording the variation of field emission intensity from a metal tip. The jumping of a Cs atom between adsorption sites on a tungsten tip has been recorded with 2 ps and sub-nanometer resolution. In our femtosecond field emission camera (FFEC),[12] electrons field-emitted from a tip and selected by a lens aperture are focussed into a spot, which is swept electrostatically across a detector screen (Fig. 1a). The spatial variation of the detected intensity along the sweep records the temporal variation of the field emission intensity (1 mm = 10 - 100 ps). Field emission (FE) is a tunneling process, which occurs when the width of the potential barrier at the surface of a metal tip is reduced by applying a negative potential (Fig. 2).[13] Electrons originate from the metal interior, but the tunneling rate depends exponentially on the local barrier

height, which is determined by the identity and location of surface atoms. FE thus provides a method for monitoring the position of surface atoms without strongly perturbing them by electronic transitions.

In our instrument, which has a base pressure of 2×10^{-11} Torr, a lens optimized for field emission[14] is positioned 7 mm from the tip. The beam electrons are multiplied by a dual microchannel plate before striking a phosphor screen, which is imaged by a vidicon and frame grabber. A krytron pulse generator[15] supplies the $\approx$ 2 kV/ns sweep voltage. To image the tip by field ion or field emission microscopy,[13] the lens voltage is turned off or reduced, so that the angular distribution of emitted electrons or ions is projected onto the detector (Fig. 1b).

Fink[16,17] showed that the triatomic end of a tungsten tip can continuously emit currents as large as 10^{-5} A, or 6×10^{13} e^-/s, which gives many electrons during the 10^{-13} to 10^{-12} s vibrational period of adsorbed heavy atoms. To begin our experiments, we sputter-sharpen a chemically etched <111> W tip to a $\approx$ 300 Å radius by field emitting in 5×10^{-4} Torr Ne.[16] Annealing briefly at 1100K forms a corner of three {211} planes.[16] Using field ion microscopy[13] (FIM) to image the tip atoms, we field evaporate to form an apex plane composed of a triangle of three W atoms[16] (Fig. 3).

Individual Cs atoms can be observed in FE, because the partially ionized adatom greatly lowers the local work function[18] (Fig. 2). A Cs atomic beam is directed at very low flux onto a 90 K tip, so that the average time between the arrival of atoms detected in the viewed area ($\approx$ 20 Å diameter) is $\approx$ 60 s. To ensure that no more than one Cs atom resides near the apex, frequent positive voltage pulses evaporate Cs atoms from the tip, while leaving the W atoms unmoved. Deposition is ended when a bright spot (Fig. 1b) appears near the image of the apex, increasing the FE by a factor of 5 to $\approx$ 10^{-11} A, and signaling the arrival of a single Cs within 1 nm of the apex. At 90 K, the atom remains at this site.

A series of alternating sweeping and imaging experiments are now performed, so that the position of the Cs atom is determined after each sweep. To sweep, the tip is pulsed with a negative voltage for several ns, generating a 5 μA e^- beam, which is focussed and swept across the screen to record the emission intensity displayed in Figs. 3 and 4. The high current heats the adsorbed Cs to ≈ 800 K, presumably by inelastic electron tunneling[6,19] or the Nottingham effect,[20] so that during the sweep, it may jump to another site.[21] Following each sweep, FE images the Cs after it has cooled (Fig. 1b). During the brief tip pulse the strongly bound W atoms do not jump.

Because the tip pulse is rounded, if no Cs motion occurs, the FE will be bell-shaped, as in sweep 6 of Fig. 3. Judging from the FE images (Fig. 3) at 90 K, the Cs occupies one of two sites in these sweeps. (Some other sites were observed in other sweeps.) In sweeps 1, 7, and 8, the Cs jumps between sites. During sweep 1, an abrupt increase in FE is observed, with a rise time within 20 ps. The atom has moved from the position giving lower field FE, occupied in sweep 6 and designated "L", to a position designated "H," resulting in higher FE. The images indicate that Cs has moved from the upper left hand portion of the image to the center, increasing in brightness because the field is stronger at the tip apex. Between sweeps 1 and 6, the atom has moved back to position L. In sweep 7 an L→H transition is observed at about the same time as in sweep 1. Although the jumping of the atom is a statistical process, in both sweeps, the jump occurs at the time when the FE is sufficiently strong to heat the Cs vibration high enough to activate the atom. During sweep 8, Cs moves H→L. The FE changes back to the curve of sweep 6 characteristic of the L position, and the FE image correspondingly returns to that after sweep 6. After the experiments, FIM confirmed that the atomic geometry of the W tip was unchanged by either the negative or positive pulses.

When the sweeping e^- beam is not perfectly focussed, the location at which an electron strikes the detector screen will depend on the position of its emission from the tip. This spatial information is lost along the sweeping direction, but the time dependence of the spatial distribution of the emitted electrons perpendicular to the sweep di-

rection can be recorded. Fig. 4 shows such a measurement, at increased sweep speed. Four traces from adjacent detector pixels are presented, each displaying a distinct time dependence from a portion of a 20 Å diameter region of the tip. The two upper traces from the upper portion of the tip show a sudden increase in the FE at about 300 ps, while the two lower traces, representing the bottom, show no increase. The sudden increase, with an apparent instrumental rise time of 2 ps, is consistent with a Cs atom moving suddenly from the edge to the upper portion of the viewed region of the tip.

Compared to photoabsorption, which switches atomic motion to a new potential surface, perturbation of the atomic trajectories by a single field-emitted electron is weak, because the electron mass is so small compared to the Cs mass. Yet the net result of many such interactions over many vibrational periods is substantial heating. The field emission of single electron could strongly perturb atomic motion if it left a localized empty state which is not quickly refilled. The heating of ultrasharp field emission tips by high DC currents has been observed recently.[6]

The FFEC is essentially an electronic streak camera[22] in which the photoemitting electron source has been replaced by a field emitter, which is itself the sample of interest. The time resolution achievable by our instrument is in principle limited by four factors. The most obvious is the ratio a/v involving the velocity v and the size a of the focus spot at the detector. In practice this effect is not limiting, because the tip is a nearly perfect point source for sharp focussing, and high sweep rates of 10 kV/ns are readily achievable. Inhomogeneities in the deflection field are not a problem, because we distinguish only relatively few (256) time points at small deflections.

A fundamental resolution limit is the distribution of the time of flight (TOF) between the tip and deflecting field caused by the ≈ 0.5 eV[23] kinetic energy spread. of the emitted electrons. Two electrons emitted simultaneously but arriving at the deflecting field at different times will be deflected to different positions on the detector. In a spatially uniform accelerating field, most of the TOF spread occurs just after the electrons are emitted, when the electrons are moving slowly and the transit time is

strongly affected by the energy. But in field emission from a point, most of the potential drop between tip and lens occurs within 0.5 mm of the tip, and the accelerating field at the tip is so strong (≈ 1 V/Å) that the TOF spread contribution due to initial acceleration is only 1×10^{-14} s. In our instrument, most of the effect of the energy spread on the TOF occurs after the region of strong initial acceleration, but before the lens, where the electron kinetic energy is ≈ 1000 eV. This region is traversed in 370 ps, so a ≈ 0.5 eV energy spread causes a TOF spread of (½)×370×.5/1000 = 0.090 ps. Over the much longer path between the lens and the deflecting field, the TOF spreads only 0.050 ps, a smaller value because the electron energy is a much higher 8 kV. A TOF spread estimated at 0.3 ps arises from the dependence of the flight time of electrons of a given energy on the off-axis angle with which they leave the tip.

The net results of these effects is that, at the highest sweep rates, the time resolution of our instrument in 0.4 ps, a number which can be reduced by a factor of 10 by scaling down the size of conventionally manufactured electron optics. Microfabricated optics[24] could enable achievement of the 10^{-14} s resolution limit imposed by the initial acceleration.

Our measurements exceed by a factor of 10^6 the speed of the fastest previous continuous measurements of single atom motion.[4,7] In addition, one-dimensional spatial resolution has been demonstrated, and with more complex electron optics, full temporal and two-dimensional spatial resolution can be achieved. In future experiments, our instrument will be used to time resolve the trajectories, including the vibrational motion, of individual atoms and molecules undergoing diffusion, adsorption, desorption, and reaction.

This work was partially supported by the Office of Naval Research and the Air Force Office of Scientific Research. H. H thanks the Swiss National Science Foundation and the Treubelfonds, Basel, Switzerland, for fellowships.

References

1. M. Dantus, H. H. M. Janssen, and A. H. Zewail, *Chem. Phys. Lett.* **181**, 281 (1991); L. Khundkar and A. H. Zewail, *Ann. Rev. Phys. Chem.* **41**, 15 (1990).
2. F. Budde, T. F. Heinz, M. M. T. Loy, J. A. Misewich, F. de Rougemont, and H. Zacharias, *Phys. Rev. Lett.* **66**, 3024 (1991); J. D. Beckerle, R. R. Cavanagh, M. P. Casassa, and E. J. Heilweil, *J. Chem. Phys.* **95**, 5403 (1991).
3. H. E. Elsayed-Ali and G. A. Mourou, *Appl. Phys. Lett.* **52**, 103 (1988); J. W. Herman and H. E. Elsayed-Ali, *Phys. Rev. Lett.* **68**, 2952 (1992); J. C. Williamson, M. Dantus, S. B. Kim, and A. H. Zewail, *Chem. Phys. Lett.* **196**, 529 (1992).
4. G. Binnig, H. Fuchs, and E. Stoll, *Surface Sci.*, **169**, L295 (1986).
5. Ch. Kleint, and K. Möckel, *Surface Sci.* **40**, 343 (1973).
6. V. T. Binh, S. T. Purcell, G. Gardet, and N. García, *Surface Sci.* **279**, L197 (1992).
7. I. Brodie, *Surface Sci.* **70**, 186 (1978).
8. Ch. Kleint, *Surface Sci.* **25**, 394 (1971); J.-R. Chen and R. Gomer, *Surface Sci.* **79**, 413 (1979).
9. G. Ehrlich and F. G. Hudda, *J. Chem. Phys.* **44**, 1039 (1966); T. T. Tsong, *Rep. Prog. Phys.* **51**, 759 (1988).
10. R. J. Hamers and D. G. Cahill, *J. Vac. Sci. Technol. B* **9**, 514 (1991).
11. D. M. Eigler, C. P. Lutz, and W. E. Rudge, *Nature* **352**, 600 (1991).
12. G. M. McClelland, USA patent 5151594; H. Heinzelmann, G.M. McClelland, and F. Watanabe, *proceedings of the NATO ARW on Manipulation of Atoms under High Fields and Temperatures*, NATO ASI Proceedings Series E ed. V. T. Binh, N. Garcia and K. Dransfeld. (Kluwer, Dordrecht, 1993), to be published.
13. D. P. Woodruff, and T. A. Delchar, *Modern Techniques in Surface Science* (Cambridge U. Press, Cambridge, 1986).
14. M. M. El Gomati, M. Prutton, and R. Browning, *J. Phys. E* **18**, 32 (1985).

15. Lasermetrics Co., Model 8612.

16. H.-W. Fink, *IBM J. Res. Develop.* **30**, 460 (1986); H.-W. Fink, *Physica Scripta* **38**, 260 (1988).

17. see also V. T. Binh, S. T. Purcell, N. Garcia, and J. Doglioni, *Phys. Rev. Lett.* **69**, 2527 (1992), and references therein.

18. C. J. Todd and T. N. Rhodin, *Surface Sci.* **42**, 109 (1974).

19. E. L. Wolf, *Principles of Electron Tunneling Spectroscopy* (Oxford, New York, 1985).

20. H. Bergeret, A. Septier, and M. Drechsler, *Phys. Rev. B* **31**, 149 (1985).

21. R. Morin, *Surface Sci.* **162**, 109 (1985).

22. for a collection of recent articles, see *Proc. SPIE - Int. Soc. Opt. Eng.* **1358** (1991).

23. E. W. Plummer and R. D. Young, *Phys. Rev. B* **1**, 2088 (1970).

24. T. H. P. Chang, *J. Vac. Sci. Technol. B* **6**, 1698 (1990); L. S. Hordon and R. F. W. Pease, *ibid.*, p. 1686.

Figures

Fig. 1. Femtosecond field emission camera. Not to scale; total length, 60 cm. a) Time resolving mode, in which the electrons are focussed and swept across the detector screen. b) Imaging mode, in which the emitted electrons are projected onto the detector to spatially resolve their emission point on the tip (field emission microscopy). For FIM imaging, the tip voltage is made positive.

Fig. 2. Potential energy diagram for electron field emission from a sharp tip, showing the effect of electric field and the adsorption of a Cs atom.

Fig. 3 Series of sweeping and imaging experiments documenting the jumping of a single Cs atom between two adsorption sites on a tungsten tip. The numbered plots present the time-resolved field emission intensity for four of eight consecutive sweeps. The time axis is referenced to the tip voltage pulse, and a smoothed sweep 6 is superimposed on all plots. The field emission images to the right are recorded after each sweep. The lower right diagram presents the FIM-determined position of the three W atoms, spaced by 4.5 Å, of the apex layer of the tip.

Fig. 4 Simultaneous temporal and one dimensional spatial resolution of field emission, showing the jumping of a single Cs atom. The four plots, recorded simultaneously, present field emission from four adjacent regions of the tip. Consecutive data points, separated by 2 ps, are connected by a straight line. The schematic indicates a possible motion of the adsorbed Cs atom consistent with the field emission.

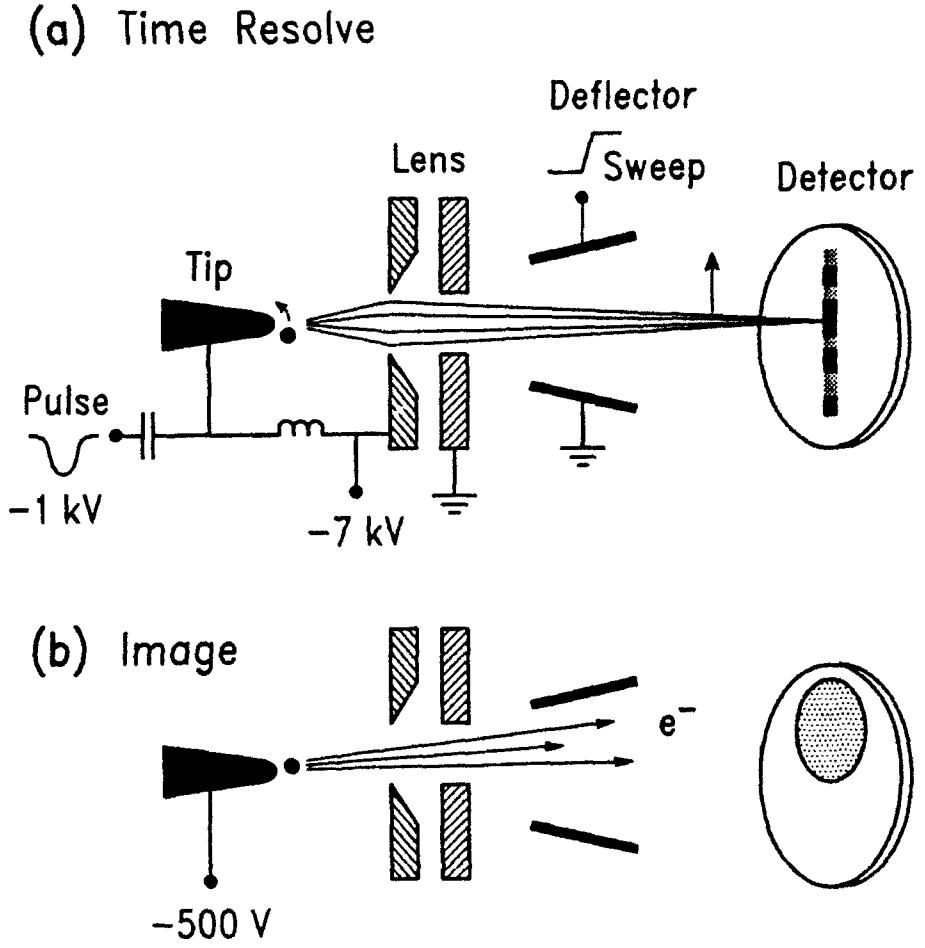

Fig. 1. Femtosecond field emission camera. Not to scale; total length, 60 cm. a) Time resolving mode, in which the electrons are focussed and swept across the detector screen. b) Imaging mode, in which the emitted electrons are projected onto the detector to spatially resolve their emission point on the tip (field emission microscopy). For FIM imaging, the tip voltage is made positive.

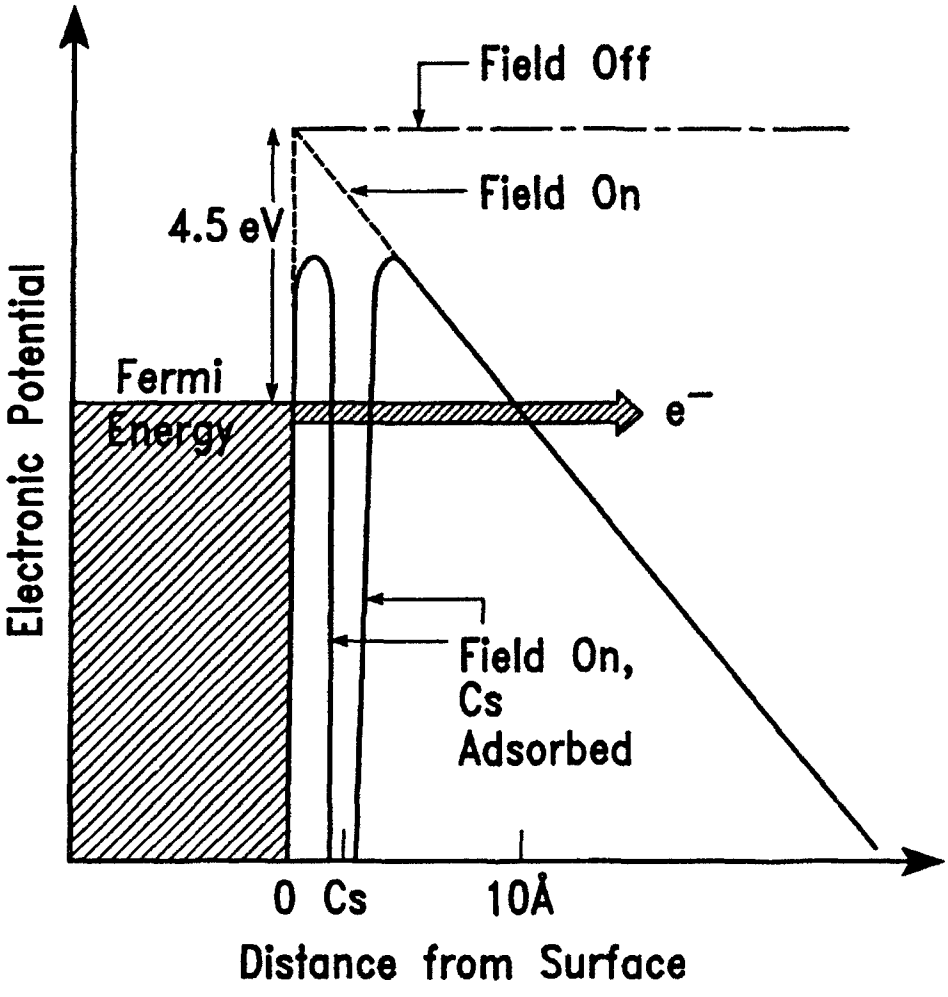

Fig. 2. Potential energy diagram for field emission from a sharp tip, showing the effect of electric field and the adsorption of a Cs atom.

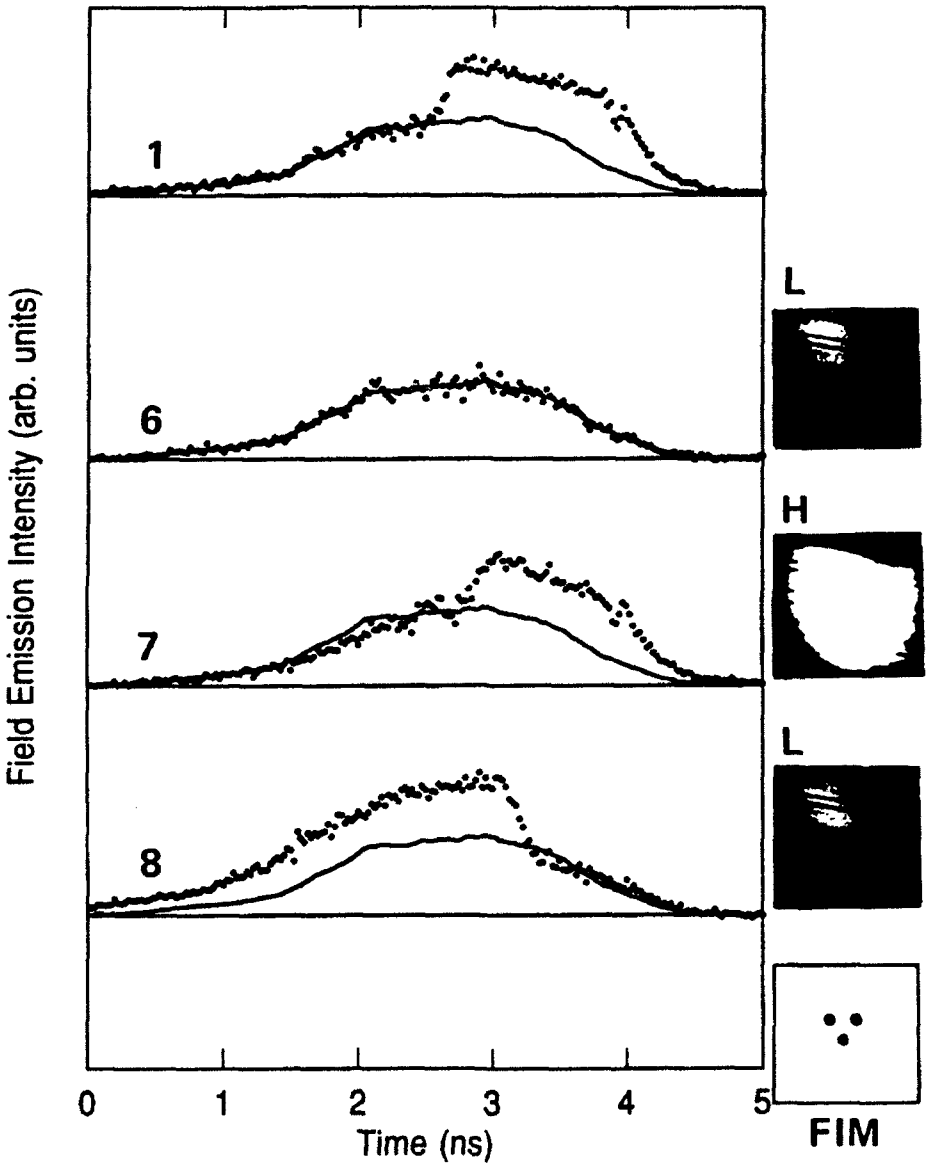

Fig. 3 Series of sweeping and imaging experiments documenting the jumping of a single Cs atom between two adsorption sites on a tungsten tip. The numbered plots present the time-resolved field emission intensity for four of eight consecutive sweeps. The time axis is referenced to the tip voltage pulse, and a smoothed sweep 6 is superimposed on all plots. The field emission images to the right are recorded after each sweep. The lower right diagram presents the FIM-determined position of the three W atoms, spaced by 4.5 Å, of the apex layer of the tip.

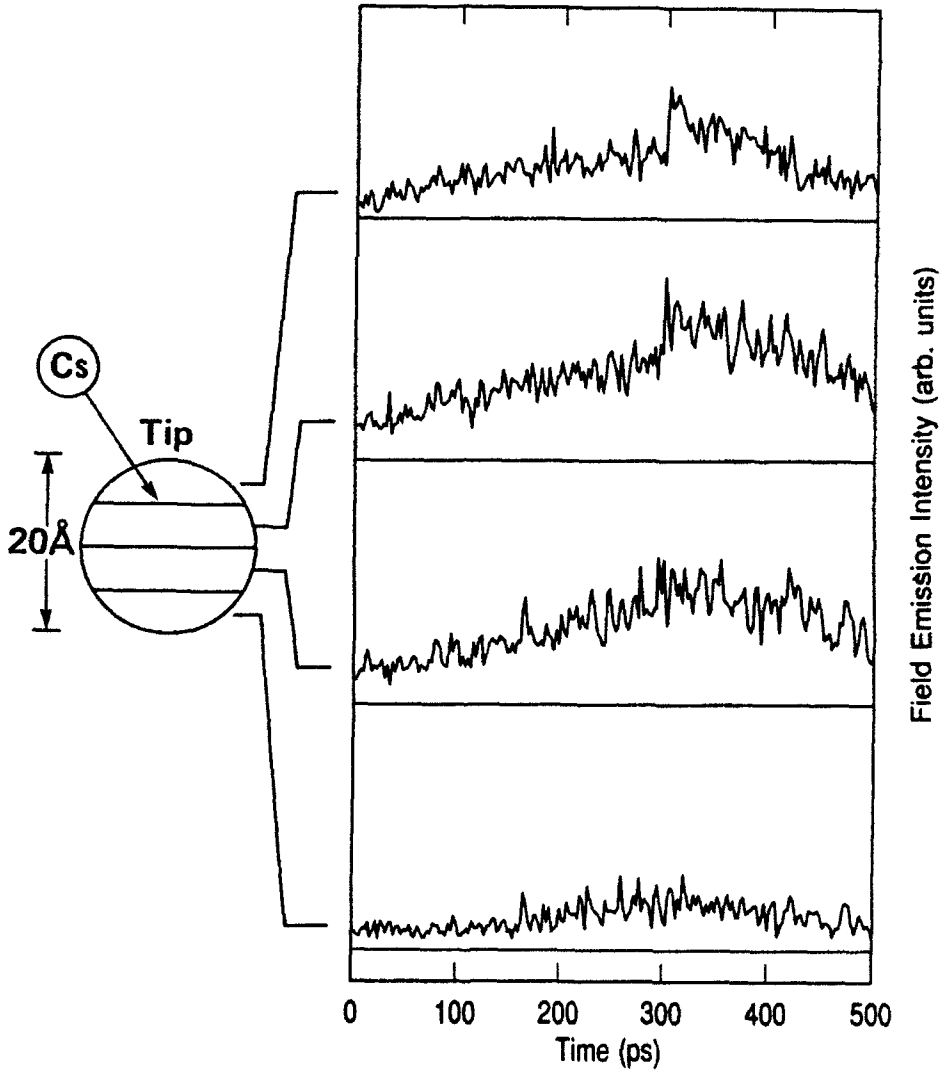

Fig. 4 Simultaneous temporal and one dimensional spatial resolution of field emission, showing the jumping of a single Cs atom. The four plots, recorded simultaneously, present field emission from four adjacent regions of the tip. Consecutive data points, separated by 2 ps, are connected by a straight line. The schematic indicates a possible motion of the adsorbed Cs atom consistent with the field emission.